AUTOMATED ANALYSIS OF NEURONAL MORPHOLOGY: DETECTION, MODELING AND RECONSTRUCTION

SREETAMA BASU
(B.Tech, West Bengal University of Technology, 2010)

A THESIS SUBMITTED
FOR THE DEGREE OF DOCTOR OF PHILOSOPHY
DEPARTMENT OF COMPUTER SCIENCE,
SCHOOL OF COMPUTING
NATIONAL UNIVERSITY OF SINGAPORE

SINGAPORE, 2014

© 2014, Sreetama BASU

Declaration

I hereby declare that this thesis is my original work and it has been written by me in its entirety. I have duly acknowledged all the sources of information which have been used in the thesis.

This thesis has also not been submitted for any degree in any university previously.

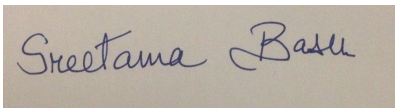

Sreetama Basu
02-05-2015

Acknowledgement

It is my great pleasure to acknowledge the support and assistance of a number of people, which contributed towards the completion of this thesis.

Firstly, I am extremely grateful to my thesis advisors Professors Daniel Racoceanu and Wei Tsang Ooi. The combination of their support, guidance and the collaborations they facilitated, has been crucial for the completion of my doctoral thesis. Dr. Racoceanu's contagious enthusiasm, constant encouragement, and considerations have been invaluable source of inspiration and motivation. The writing and organizing of my thesis was made easy due to his insightful comments and suggestions. Dr. Ooi made himself available for discussions and mentoring at any time of need. His meticulous analysis and dissection of arguments, focus on precision and clarity of presentation — encouraged and challenged me throughout my doctoral studies to be a better researcher.

I thank my thesis advisory committee, Professors Wynne Hsu and Michael Brown, for providing me valuable feedback and suggestions for improving my work on numerous occasions, inspite of their busy schedules.

My sincere thanks and gratitude to Dr. Elena Zhizhina and Dr. Maria Kulikova for the enriching discussions on marked point processes. Dr. Zhizhina, during her visit to Singapore and over numerous emails, and helped me achieve a deeper understanding of the point process methodology. Dr. Kulikova, during the early part of my PhD, provided me with essential mentoring in technical report writing and presentations.

I greatly appreciate the efforts of the staff at Graduate Office, SOC and also at IPAL, who helped me immensely with all the paper work during conference trips and for their support and tolerance in navigating administrative matters during the course of my PhD.

I thank my friends and lab-mates for their technical help, de-stressing tea-times, and precautionary advices that helped me avoid many a pitfall. I am very thankful for the friends I have made here in Singapore, who made it a home

away from home. In particular, Pooja, Damtei and Skanda - I cherish the loving company, cheerful encouragement and the many laughs.

Finally, I am forever indebted to my parents Siddhartha Basu and Sunanda Basu, and brother Soumyak Basu for their support throughout my doctoral studies. Their patient understanding, constant encouragement and endless love have been my pillars of strength.

Abstract

Automated Analysis of Neuronal Morphology: Detection, Modeling and Reconstruction

This thesis addresses the problem of automatic analysis of neuronal tree morphology: from detection, modeling to digital reconstruction of tubular branches of neurites from 3D Light Microscopy image stacks. Comprehending the complex structure and connections of the neurons is key to the study of brain development and functioning. Advances in neuro-imaging has enabled us to capture such neuronal morphology in previously unimaginable details. The huge volume of rich and heterogeneous data generated, however, makes expert manual analysis of such images tedious, subjective and prohibitively expensive. Thus, robust, scalable and highly automated algorithms are desired to analyze such data. In this thesis, we propose a framework for automated quantification of neuronal morphometrics. We target three important methodological areas of biomedical image analysis.

First, we present an automated, unsupervised object *detection* framework using stochastic marked point processes. We propose special configurations of marked objects and an energy function well adapted for vessel-like tubular structure networks. It incorporates both radiometric properties and high level structural constraints into a probabilistic formulation and global optimization scheme. This enables extraction of connected neuronal networks by fitting an optimal configuration of spheres to the centreline of the branches giving us the position, local width and orientation information.

Second, we explore the problem of *modeling* of single neuron morphology. We propose new priors for accurate identification of critical nodes like bifurca-

tions and terminals and sophisticated semantic interpretation of complex neuronal morphology. Such explicit modeling of neurites derive various characteristic morphological and geometrical parameters such as total length, internodal lengths, branching index, branching angles, average branch curvature etc., to describe the neurons. We tackle parameter estimation for the marked point process model by relating the model parameters to the application data. A critical analysis of the sensitivity and robustness of the model identifies the parameter dependencies and rules for initialization of the critical parameters.

Third, we focus on *reconstruction* of neuronal branches using robust and efficient numerical fast marching methods into connected minimum spanning tree representations. We exploit image potential in evaluating the connectedness of nodes that are Euclidean neighbors to remove the false positives. Thus, we generate a mathematical description abstracting out the important position and connectivity information about neuronal branches from the microscopy data. Such digital reconstruction can be represented in the standard SWC format, prevalent for storage, sharing, and further analysis in the neuroimaging community. Our proposed pipeline outperforms existing neurite tracing algorithms and minimizes the subjective variability in reconstruction, inherent to semi-automatic and semi-manual methods.

Keywords: Neuron morphology description; Marked point processes; Fast marching; Neurite tracing; Digital reconstruction.

Thesis Advisors:
Professor Daniel Racoceanu
Associate Professor Wei Tsang Ooi

List of Publications

1. A Stochastic Model for Automatic Extraction of 3D Neuronal Morphology. **Sreetama Basu**, Maria S. Kulikova, Elena Zhizhina, Wei Tsang Ooi, Daniel Racoceanu. Medical Image Computing and Computer Assisted Intervention **(MICCAI 2013)**, Nagoya, Japan, September 22-26 2013.

2. Improved Marked Point Process Priors for Single Neurite Reconstruction. **Sreetama Basu**, Wei Tsang Ooi, Daniel Racoceanu. 4TH International Workshop on Pattern Recognition in Neuroimaging **(PRNI 2014)**, Tuebingen, Germany, June 4-6 2014.

3. Reconstructing Neuronal Morphology from Microscopy Stacks using Fast Marching. **Sreetama Basu**, Daniel Racoceanu. IEEE International Conference on Image Processing **(ICIP 2014)**, Paris, France, October 27-30 2014.

Contents

List of Figures

List of Tables

Chapter 1

Introduction

Contents

1.1 Motivation: automatic analysis of high content, high resolution data

Various biomedical techniques rely largely on image data as their primary source of information. The emergence of fluorescence labeling technologies and the development of sophisticated imaging microscopes, such as confocal and multi-photon, has enabled acquisition of high-resolution digital images of neuronal networks both in vitro and in vivo. This allows the cellular bio-chemists and neuro-anatomists to monitor their structural dynamics in response to various stimuli. Neuroscience has unearthed a strong structure-function relations in the nervous system. The intricate connections and patterns of the neuronal fibres throughout neuron networks, retain what we have learned, and how we respond to external stimuli. This structure-function relation of the nervous system eventually influences our higher order cognitive functions such as speech, motor functions and intellectual capacities. Hence, the ability to accurately capture the morphological information of neuronal trees and their connections and track their dynamic changes is crucial to a better understanding of the brain and its functions.

While the technological advances and development of new imaging modalities like *Super Resolution Imaging, Serial Section Electron Microscopy* have opened up exciting avenues of investigation in neuroscience; it also gives rise to unimaginably vast quantities of image data. Consequently, it created a number of computational, algorithmic, and mathematical challenges involving the analysis and modeling of high-resolution data. In [95], the authors talk about the new

era in biomedical informatics where focus is on brain atlas building for model organisms, understanding the dynamic processes in cells of living organisms, reconstruction of 3D neuronal structures and generating the wiring diagram of a brain. Such tasks place higher demands on traditional segmentation, registration, annotation, mining, indexing and visualization methods. There is a clear requirement for algorithms to analyze biomedical images in a more expressive way than traditional methods.

Recently, there have been successful attempts at construction of brain atlases for model organisms like mouse, drosophila, zebra fish etc., to promote simulation based research [66]. The Allen Atlas Project [1] developed a Google Earth-like tool that allows interactive navigation through the nervous system model of certain organisms with anatomical and ontological information integrated with corresponding morphological structures. Simulation based research will enable us to gradually move away from experiments on live animal once there is enough knowledge, data, computing power and intelligence to support their biological objectives.

Progress in the above described direction would require detailed *Brain Atlases* with descriptive parameters for common neuron types such as average total length, branch length, branching order and angles. This enables to statistically compare different populations of neurons or to quantify changes in morphology for the same class of neuron over time in 4D time series data, which is the future goal in neuroscience [47]. It is known that morphology/structure is intricately related to neuronal functions. The characterization of normal and degenerated morphology allows early detection and analysis of pathological conditions.

Till date, understanding the brain physiology remains an elusive task. To enable scientists to ask and answer questions about the brain of evolved organisms would require reverse engineering the complex anatomical and functional wiring of the neuronal networks that make up the brain. An interesting example is the Blue Brain Project [2], which attempts to synthesize and simulate the neocortical columns of human brain to create the first virtual brain capable of emulating the intelligence of a regular human. A detailed computer model of a virtual brain that is truly equivalent to the biological counterpart, could in principle allow scientists to carry out experiments that could not be performed on real nervous systems because of physical constraints.

One of the scientific challenge of foremost interest in the current times is *Brain Mapping* [9, 46]. Scientists are attempting to develop a synaptic connection level circuit map of the brain at nano scale resolutions called "connectomes". The complete description of morphology of single neurons is called the "neurome"; while the study of connectivity and topological changes due to degenerative diseases changing this model "connectome" is called "connectopathology". It is expected to eventually translate the so generated expertise into a behavior-structure mapping of the brain.

A critical step for all these efforts is quantitative analysis of neuronal anatomy.

Automated computational methods allow generating highly detailed neuronal morphological structures in minutes compared to manual tracing which would take months and years. The automated analysis of large image has emerged as the major bottleneck in neuroscience research, digital histopathology and other biomedical domains. In neuroscience, it is estimated that while tissue

preparation, labeling and imaging takes days; expert manual analysis of the acquired image volumes takes years in terms of man hours. Depending on experience of the human tracer, there is significant subjectivity and variability in analysis. Though manual tracing is considered superior in-spite of subjective variability, it is prohibitively expensive in terms of human labor.

At Light Microscopy resolution, it takes approximately 1 hour per millimeter of neurite path, totaling 30 hours to completely trace a single spiny stellate neuron of rat barrel cortex [49]. In order to reconstruct connections at synaptic levels, scientists need to resort to superior microscopy techniques like Serial Section Transmission Electron Microscopy (SSTEM). Manual tracing of SSTEM data is even slower at 1-2 hours per micrometer, i.e., 200-400 hours per millimeter of neurite length. Complete analysis of connectomic structures from SSTEM data is a daunting task estimated to take 24K-80K human work years for cortical column neurons of evolved species like humans [49]. The DIADEM Challenge (*DI*gital Reconstruction of *A*xonal and *DE*ndritic *M*orphology) [42] was organized so that resulting algorithms will push the boundaries of automated reconstruction on the most challenging data available. The competition brought together all necessary resources and existing knowledge in this multidisciplinary domain to facilitate continuous development of automated neuronal reconstruction algorithms.

Comprehending the complex neuronal wiring diagram of the brain is key to understanding its functions. The aim is to create a connectome, i.e., a circuit map of the brain with details of the wiring of each individual neuron. To appreciate the enormity of the task one can consider the fact that till today scientists

have managed to create the connectomic mapping of a single, very primitive organism, the roundworm (*C. Elegans*) [125]. It is known to have 302 neurons and approximately 5000 synaptic connections amongst them. It is estimated the generation of the connectome of the *C. Elegans* took 15 years of man hours. The complexity of the task increases exponentially for more evolved organisms. The common fruit-fly (*Drosophila Megalonaster*) having 100,000 neurons is estimated to have 10^7 synapses. In comparison, the average adult human has $85,000,000,000$ neurons and a staggering 10^{15} synapses to map in order to generate a human connectome. To achieve the aforementioned objective, automated 3D neurite tracing is a crucial step.

1.2 Objective: detection and reconstruction in biomedical images

Advent of various high content,high resolution imaging technologies have necessitated the development of high throughput analysis. Automation of analysis of such data will not only speed up the process but can also weed out operator variability. Grand challenges in mapping the Brain [46], digital histopathology [52, 102, 51], and remote sensing [59] — all examples of various domains where very large images are required to be analyzed. For most of these images the relevant information needs to be abstracted out from the image data and quantified in mathematical models for subsequent analysis. This is a new challenge in the field of bio-imaging due to the high-content nature and large size of these images. High-level spatial relation and configuration modeling issues and even

semantic approaches are gaining momentum in the image analysis and computational bioinformatics fields. In particular, it is important to mine high-content, large scale images in more expressive ways than a purely statistical description [70]. Hence, efforts in developing frameworks that allow incorporating high level geometric and shape priors for modeling the data need to be addressed. The demands of the new era of image analysis requires highly automated algorithms that are also robustly scalable.

The objective of this thesis is two-fold — automatic bio-image analysis and quantitative image informatics. Firstly, we develop efficient, automatic stochastic marked point process framework for unsupervised extraction and description of neuronal morphology from 3D microscopy image stacks. We use this extracted information to adapt fast, robust and accurate numerical methods for digital reconstruction of neuronal fibres as minimum spanning trees into standard *SWC* format. Secondly, we identify critical nodes in neuronal arborization such as bifurcation and terminals, which generate further information about branching index, branch length, branching angles, tapering rate and so on. These parameters are used to quantify neuronal cell types for classification or morphological comparison. Before the era of high-resolution imaging, these parameters of neuron populations were estimated with classical statistical methods. The digital reconstructions capturing positional and connectivity information in standard format help in storage, archiving and subsequent analysis of neuronal structure.

ID	T	X	Y	Z	R	C
1	1	−1.5	−8.2	1.3	3.8	−1
2	3	0.8	4.2	1.4	2.3	1
3	3	21.1	41.1	1.4	1.3	2
4	3	89.2	115.1	−5.3	1.1	3
5	3	153.6	163.5	3.0	0.6	4
6	3	184.9	218.1	−2.3	0.5	5
7	3	220.9	238.7	−13.7	0.3	6
8	3	159.9	183.9	−23.6	1.1	4
9	3	211.9	270.9	−35.2	0.7	8
10	3	0.6	58.1	−2.6	1.1	2
11	3	−0.5	75.9	−18.6	1.1	10
12	3	−40.5	180.0	−55.3	1.0	11
13	3	−156.4	281.8	−65.9	0.8	12
14	3	0.3	186.8	−7.0	0.8	12
15	3	−51.5	235.7	−27.0	0.8	14
16	3	−85.2	297.6	−41.5	0.5	15
17	3	75.3	198.3	−54.6	0.8	10
18	3	130.6	228.6	−81.3	0.5	17

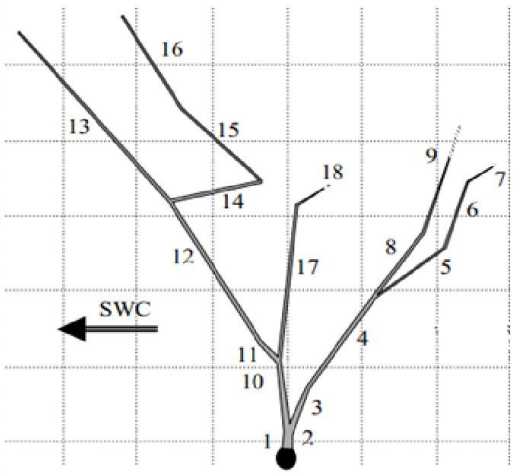

Figure 1-1: *Digitized representation of neuronal morphology in SWC format.*

1.3 Problem definition

There are two principal ways of studying neuronal structures. The classical neuro-anatomical analysis is based on estimation of certain geometrical descriptive parameter values that typically result in some statistical distribution. In this case, for generation of virtual neurons, parametric values from such distributions are sampled stochastically. The second method of representation of neuronal morphology is the digital format that deterministically generates values for complete description of the neurons. For more details the interested reader can refer to [8]. This second category of representation has only been made possible due to recent advances in biomarker and imaging technology that captures neuronal morphology with unprecedented resolution and magnification. This enables high-fidelity modeling of neuronal morphology. Our focus is, thus, the second category of methods. Recent advances in imaging technologies gener-

ate tera-bytes of data. For example, the nervous system of a nominally evolved organism like the fruit-fly imaged by Electron microscopy technique for connectomic studies generated 800 tera-bytes of image data. But mostly, this data is sparse. Digital representation of neuronal morphology results in compact mathematical descriptions that offers ease of archiving, exchanging, comparing and analyzing. Neuronal data are generated through diverse image acquisition techniques such as Fluorescent microscopy or Confocal microscopy, and different staining techniques like genetic methods or fluorescent proteins. Hence algorithms for general applicability have a very difficult task. Moreover, neuronal processes can have very complicated orientation and branching pattern. Even manual reconstructions of the same neuron show significant inter-operator and intra-operator variability besides being extremely labor intensive.

Given a 3D neuron image obtained by any of the common microscopy techniques, reconstruction refers to a digital record of the morphology of the neuronal process, (Figure 1-1). It involves firstly segmentation of the objects of interest and then quantification of segmented objects according to their arbor types. This abstracting out of the neuronal tree from the image data into a mathematical model facilitates further querying and analysis. Figure 1-1, taken from [8], illustrates digitized representation of neuronal morphology in *SWC* format. Every critical point (bifurcation node, terminal node and inflection node) is represented as a 7 tuple with an unique identity (ID). Tag (T) represents arbor type (Soma 1, Axon 2, Dendrite 3) of concerned point. X, Y, and Z are the coordinates representing the physical position of critical points in 3D image stacks. 'R' column records radial width of process and last column (C) holds the ID

of parent node. In this way the SWC representation abstracts out all relevant information about neuronal morphology from 3D image volumes of several Gigabytes and captures it in a analytical model in a text file.

1.4 Technical challenges

Automatic digitized representation of neuronal networks is being attempted since Ramon and Cajal proposed the first model of neurons in the 19th century. The field gathered new impetus in the last 10 years when recent development in microscopy techniques finally made the necessary data available. The bottleneck to digitized reconstruction are processing speed, data access (with large data-sets 96 GB of RAM has proved insufficient to hold the entire data at once) and processing intelligence for expert automated tracing. While solutions to processing speed and data access can be achieved through clever parallelization on multicore systems or GPU based simulation, processing intelligence remains a much tougher challenge [90]. Much of the difficulties in neurite tracing arise due to the artifacts introduced during image acquisition. Such artifacts are unavoidable given neurons are inherently 3D, but any image acquisition technique records their 2D projections. Even for imaging a 3D volume the slicing thickness of the sample limits the resolution in "Z" direction (perpendicular direction to imaging plane) to be much coarser compared to "XY" (in- plane resolution). Images (Figure 1-2) adapted from [21], illustrate the challenges faced by automatic neurite tracing algorithms. Examples of automated reconstruction demands are explained as follows:

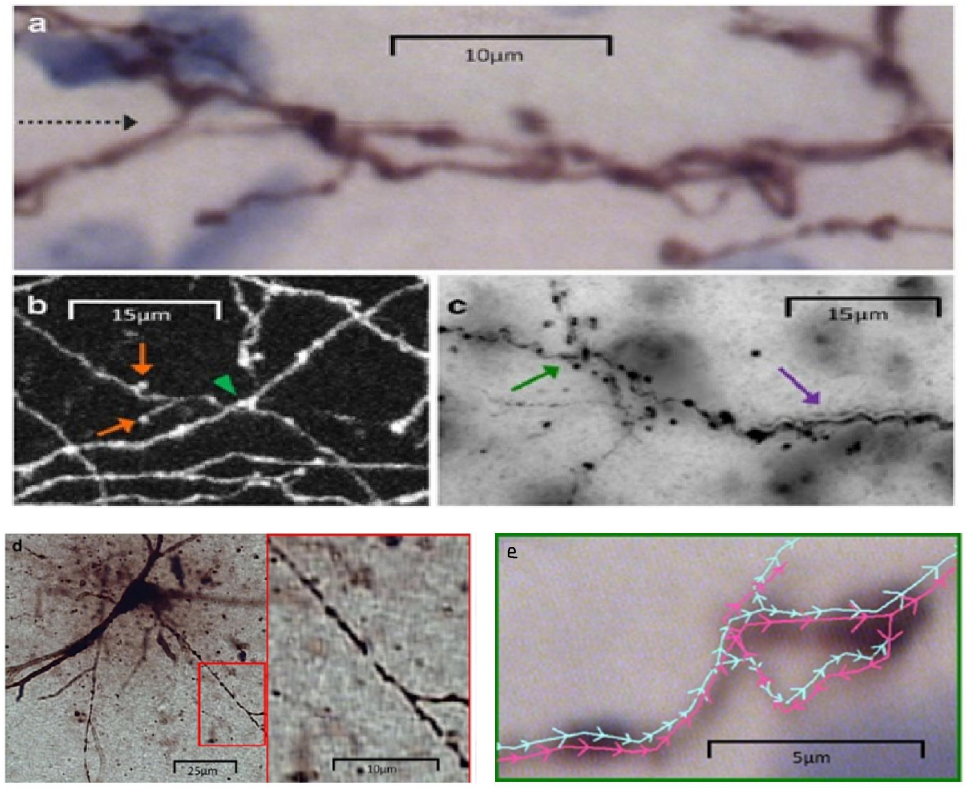

Figure 1-2: *Challenges faced by automatic neurite tracing algorithms.*

Figure 1-2a shows fibers reaching the limit of light resolution resulting in fuzzy structures with unclear boundaries when zoomed-in. Black dashed arrow shows slight image tile offset due to stitching together neighboring overlapped sections. This kind of artifact arises when the region to be imaged is too large to be captured all at once.

Figure 1-2b shows how 2-D projections of neurons which are typically 3-D objects result in obscuring branch connectivity at critical points like bifurcations and overlaps (green arrow). Neurite boutons show up as detached blobs (orange arrows in Figure 1-2b and green arrow in Figure 1-2c). Out-of-focus branches

exhibit 'halos' that can be mistaken for additional parallel branches (purple arrow) are highlighted in Figure 1.2c. Close lying parallel processes can in turn be mistaken for "halo" effect.

Neurite branching can be quite complex and manual tracing is tedious, time consuming and subjective. As seen in Figure 1-2e, there is often inter and intra operator variability (marked in different colors). The pink traces form a closed loop which is impossible in a neuronal tree. This is a major point of contention in the field as newer algorithms performing better than interactive or semi-automated manual traces are penalized on comparing against gold standard manual reconstructions. Branch gaps (red square zoomed-in on the right) resulting from inhomogeneous staining of the neuronal processes or noise injected during image acquisition are shown in Figure 1-2d. For an elaborate description of such artifacts one can refer to [21].

Manual tracing can resolve such ambiguities in neurite tracing by following Gestalt principles of human perception [80]. But with 10,000 fold increase in speed desired, manual tracing is time-wise an infeasible option. Automatic tracing needs to be enabled with the intelligence to emulate human operators in resolving such ambiguities and also to root out the subjectivity of manual reconstruction.

1.5 Overview and contribution

In the context of automating all stages of the neuron morphology analysis, the objective of this thesis is to automate detection, modeling and reconstruction

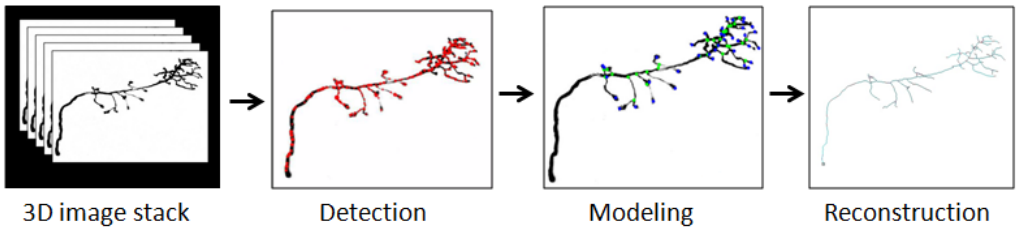

Figure 1-3: *The 3D stack of microscopy data containing the neuronal branches is the input to our algorithm. The detection, modeling and reconstruction of neuronal branches from the image volume by our proposed method.*

of neuronal morphology from 3D light microscopy image stacks. Refer Figure 1-3, for illustration. The input for our proposed pipeline is the 3D stack of microscopy images containing the neuronal data. We proposed special marked point process model for detection and modeling of neuronal branches and finally an automated pipeline using fast marching method for the reconstruction. The final output of our proposed pipeline is a SWC file containing all the positional, connectivity and branch hierarchic information about the neuronal tree. The proposed methodology is applied to the delineation and reconstruction of neuronal networks and trees from 3D confocal microscopy stacks of images.

This thesis targets three important methodological areas of biomedical image analysis and computer vision:

Firstly, we propose an automatic, unsupervised object *detection* framework using stochastic marked point processes incorporating both radiometric information and high level structural constraints for extraction of the neuronal fibre networks. The second part is devoted to the *modeling* of single neuron morphology by proposing new priors for accurate identification of terminal and branching nodes. Thirdly, we focus on robust and efficient numerical techniques like fast marching methods for *reconstruction* of merging of neuronal branches into

connected minimum spanning tree representations. Such digital reconstruction abstract out the important position and connectivity information about neuronal trees from the microscopy data and represent it in the standard SWC format, prevalent for archiving, exchanging, and further analysis in the neuroimaging community. The contributions for each task is outlined below.

Detection of particular pattern or feature is a frequently encountered task in image processing and computer vision. In case of biomedical images or remote sensing images, the data tends to be very large images, but have sparse repartition of the objects of interest. In such cases *detection* algorithms are desired to have the ability to incorporate high-level spatial relation and geometric constraints. In the first part of the thesis, we propose a stochastic marked point process model for unsupervised, automatic object detection. This marked point process framework allows to simultaneously exploit low level radiometric properties of the image data as high level geometric and prior shape constraints by means of an Gibbs energy formulation. We propose a special configuration of marked objects and an energy function well adapted to tubular structure networks. These energies enforce connectedness of the neuronal tree components, in spite of imperfect labeling, causing intensity inhomogeneity and discontinuities in branches. Our model extracts networks of neuronal fibres preserving their continuity from various 3D confocal microscopy data sets. This work has been published in the 16th International Conference on Medical Image Computing and Computer Assisted Intervention (MICCAI 2013) [17].

The second section of the thesis focuses on *modeling* single neuron morphology. In this work, we classify the various parameters of the model and

relate their initialization to the application data to automate parameter initialization. A study of sensitivity and robustness of model parameters identifies the critical parameters and their data dependencies. We propose priors modeling arborization patterns encountered in single neurons. These specialized priors enables efficient identification of bifurcation junctions, terminal nodes and intermediate points on neurite branches. The explicit modeling of critical nodes derives various characteristic parameters such as branching index, branching angles, internodal lengths, branch curvature besides aiding in reconstruction. We demonstrate how our model presents accurate and sophisticated semantic modeling of complex neuronal morphology. We complete the presentation of our model with an analysis of the errors and their sources in the neurite tracing pipeline in the hope of better integration of neuroimaging and automated tracing. This work has been published in the Pattern Recognition in Neuro-Imaging Workshop (PRNI 2014) [18].

In the final part of the thesis, we propose an automatic pipeline for *reconstruction* of 3D image data. We present a Fast Marching based geodesic curve tracing algorithm for automatic and reliable reconstruction of neuronal morphology into minimum spanning trees. The fast marching extracts the neuron branches as geodesic minimal paths which iteratively reconstructs the entire neuron tree. It is robust to ambiguous branch discontinuities, variability of intensity and curvature of fibres, arbitrary cross-sections, noise and irregular background illumination. We demonstrate the effectiveness of our method on synthetic data modeling challenging scenarios and confocal microscopy data of Olfactory Projection fibres from DIADEM data set. The preliminary results

have been published in IEEE International Conference on Image Processing (ICIP 2014) [19].

Our proposed pipeline outperforms existing neurite tracing algorithms in accuracy and minimizes the subjective variability in reconstruction, inherent to semi-automatic methods.

1.6 Thesis organization

The remainder of the report is organized as follows:

In Chapter 2, we begin by reviewing the background definitions and analyzing the existing literature for the various approaches applicable for reconstruction of tubular structures from biomedical image data. We give special focus on methods that have been employed for neuronal morphology analysis.

In Chapter 3, we briefly introduce the marked point processes methodology for object detection in high content, high resolution images. Next, we present the stochastic marked point process framework for automatic prior-shape based detection of tubular structure networks, requiring no user-interaction.

In Chapter 4, we present a study of the sensitivity and robustness of the parameters of the model and how to relate the parameter estimation to the application domain. This enables us to propose new priors that help in accurate modeling of critical nodes such as bifurcations and terminals.

In Chapter 5, we propose a methodology for efficient automatic reconstruction of neuronal morphology from 3D microscopy data stacks using fast marching methods to represent neuronal branches as connected minimal spanning

trees.

Chapter 6 concludes the report with discussion of contributions and summary of the work in the thesis. We also present a perspective on related future research directions.

Chapter 2

Background

Contents

Segmentation of 3D tubular structures such as neurons are abundantly encountered in biomedical image analysis. Some common examples of such struc-

tures are vascular network segmentation in angiograms, microvasculature in retinal images, blood vessel segmentation in liver images, bronchial pathways in chest x-rays or CT scans. Segmentation methods vary according to imaging modality, particular biomedical requirement, application domain. For an extensive review of segmentation techniques of general vessel extraction literature, the interested reader is referred to [53]. The focus of the background review in the rest of the chapter will be the various seminal and recent methods applied to neuronal data.

Neurons are the structural and functional building blocks of the mammalian nervous system. The neuronal processes, axons and dendrites arise from the soma (cell body) and repeatedly branch to form a complex arborization pattern that spans a 3D space and forms unique connection patterns. It has been well established that variation of the neuronal morphology has significant effect on the connectivity and consequently, the activity of the nervous system. This structure-function relation is, in turn, also related to higher order cognitive functions of the organism. Hence, neuronal analysis is an important part of drug treatment and therapy for psychiatric and neurological disorders (e.g., Autism), age-related neuro-degenerative diseases such as Dementia, Parkinson's, Alzheimer's. Structural changes in neurons act as precursors of onset of pathological conditions.

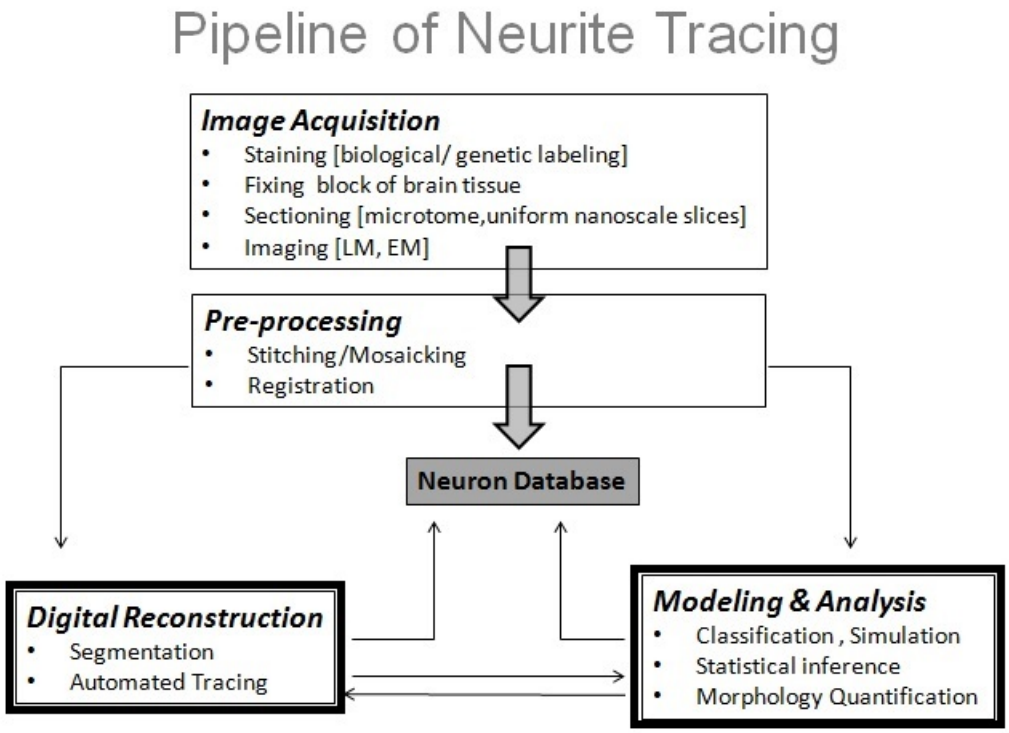

Figure 2-1: *The neuronal reconstruction pipeline. Our proposed methods and contributions are aimed at the areas represented in bold boxes.*

2.1 Data acquisition pipeline

The traditional microscope has come a long way since its conception and can provide a deluge of detail on neuronal morphology. Currently, sophisticated Light Microscopy (LM) technique can reach magnifications of up to X1500 and has a theoretical resolution limit of 200 nanometers. Electron Microscopy (EM) provides finer details with X50,000 magnification and reaches resolutions of 0.2 nanometers. The integration of Charged Couple Device (CCD) camera to microscope allows recording digital images that can directly be displayed on computer screen for analysis. The development of digital microscopy brought

many additional benefits in terms of archiving images for reuse, superior data visualization, automated image analysis and has opened up many new avenues of research. For example, automatic high throughput semantic analysis of high content, large scale digital histopathology slides. Since research in neuroscience is increasingly dependant on image analysis of massive amounts of heterogeneous and complex data collected by diverse imaging modalities, it is worthwhile to take a look at the data acquisition mechanism. Figure 2-1 illustrates the neuronal reconstruction pipeline.

Data acquisition refers to a multi-step process starting from tissue staining to extraction of fluorescent images containing structural information. The experimental procedure of obtaining single neuron image is an arduous task. Figure 2-1 explains the sequence of events in the data acquisition procedure by common microscopy technology. Fixation involves embedding the tissue in a block which preserves the tissue for long-term observation and processing. Sectioning or cutting the 3D volume into slices parallel to imaging plane is necessary due to diminishing depth-of-field of the high magnification objective lens needed to resolve details at cellular levels. Next, the neurons are labeled with fluorescent dyes so that they acquire differently colored stains to enable accurate evaluation of the generally intricately intermingled arbors. Tissue preparation, sectioning and staining are tedious procedures that require a very high level of precision and accuracy on part of the technician. It is a delicate procedure which even the most experienced neurobiologists find challenging. One point of contention with the serial section LM or EM techniques is that the Z direction resolution is coarser (limited by sectioning thickness) than the in plane resolution and varies

at different slices resulting in anisotropic voxels which compromises reliability of neurite tracing. Recent research efforts focus at improving discrimination in depth by imaging with polarized light (principle of confocal microscopy) and using computer controlled fine focus techniques, which significantly minimizes the number of cutting artifacts generated by physical sectioning [8]. Similarly, labeling methodologies contend with the question of whether neurons are stained completely and whether structural changes were imposed by the method of tissue processing for image acquisition. Modifications of optical microscopy methods like the confocal scanning microscope or the phase contrast methods use polarized light source that negates the need of staining the tissue.

In conclusion, high branch contrast with background and other cellular components is desired to increase fidelity of subsequent digital reconstruction. Homogeneity in the staining of the processes is desired. Any error in sample preparation and image acquisition will get propagated to the subsequent tasks and its impact will get magnified. [21] provides a good review of the image acquisition techniques for neuronal morphology. Automation is desired in every step to weed out human error and prevent artifacts from appearing on digital slides. The focus and scope of the work in this thesis is on automating the analysis of the acquired image volumes highlighted in the schema of neuronal morphology analysis in Figure 2-1.

2.2 Data pre-processing

Microscopy imaging of neuronal morphology is typically affected by blurring and Poisson noise. Image pre-processing becomes an absolute necessity to remove noise injected during the process of image acquisition, filtering, compression and reconstruction. The common sources of imaging artifacts are non-uniform staining resulting in inhomogeneous contrast, background gradation due to non-uniform illumination, tile stitching or image mosaicking to make montages. Poor staining gives rise to noisy images; neuronal fibres having low contrast with the background which causes weak edge response, and also varying contrast along the length and width of the fibres. Mosaicking is the method of stitching together and registration of multiple overlapped image sections when the region of interest is too large to be captured at the required resolution all at once. Errors arising due to creating such montages are called tilling errors. Pre-processing is necessary to avoid amplifying these irregularities and mistakenly interpreting artefactual noise as structural components of the neurons [4]. Hence, image restoration is necessary using smoothing, de-noising and enhancement techniques.

Anisotropic diffusion methods suppress noise while preserving image features. Morphological filtering operations like erosion are used [134] to segregate objects in apparent contact, for example close lying processes like parallel running axon fibres. Dilation is used to fill in and make solid weakly contrasted inhomogeneously stained processes. Often in multi-scale extraction, spines appear as detached blobs and dilation is needed to make connection with parent processes and maintain continuity.

Mathematical de-convolution sharpens neuronal processes in image and kills noise [103]. It also gives a final increase in overall resolution. While confocal microscopy images exhibit small lateral and axial resolution difference, this poses as a major difficulty for wide-field microscopy images. Traditional blind de-convolution which attempts to generate results without a-priori knowledge of the point spread function of the microscopic setting (which is generally not available) proves to be an impossible task estimated to take weeks on contemporary microscopy images. [91] provides a review of pre-processing techniques. They propose a novel multi-scale wavelet based Curvelet Transform for de-noising. A Scalar and Tensor voting with steerable filter is used for continuity enhancement that is particularly good at preserving tracing context at critical points like bifurcation nodes and inflection points.

Current high resolution microscopy technology enables generation of high throughput, high content data. Pre-processing is also used to reduce computation cost of such data in a *multi-scale framework*. A rough segmentation is initialized in low resolution images and only those regions of the image are considered in the high resolution version for further refinement, particularly for sparse images. In [26], the authors propose an efficient multi-scale graph tracking algorithm.

Recent trends in related biomedical histology analysis methods indicate that rigorous pre-processing greatly improves and helps the subsequent automatic segmentation. At the same time, pre-processing the data should not compromise the ability to follow the morphology by distorting branching feature or artifactually modifying network pattern by affecting process diameter, inducing

varicosities and creating or merging discontinuous. Many algorithms have been proposed in the literature for enhancement of filament-like structures — early methods like multi-scale Eigen analyis of Hessian matrix [36], shape preserving morphological filtering [126]; and more recent phase congruent Eigen decomposition [31], Gabor wavelets [81] methods.

2.3 Computational analysis of neuron morphology

After data acquisition and pre-processing we arrive at the final and most important step in this pipeline- extraction of the neuronal network. This task involves segmentation of the neuronal branches followed by quantification of the branch topology hierarchy. In [113], the authors present a method for volume partitioning of 3D microscopy image stacks for estimating somata, axon and dendrites from neuron morphology. Generally, the soma takes up the biological dyes more strongly and uniformly than the branches and presents a stronger contrast with the background. Hence, it is comparatively easier to segment and gives some indication about the starting points of the dendritic and axonal processes. Traditional segmentation methods like intensity thresholding and repeated morphological filtering (dilation and erosion) is generally adopted for the purpose. Next, the segmentation of the neuronal processes, i.e., dendrites and axon, collectively called neurites is considered. They present a much tougher challenge as they are sinuous processes with variable contrast with the background.

There are multiples ways of doing structural analysis of neuronal morphology [34]. One way is to represent digital reconstruction as a series of points

Algorithm	Local/Global Gradients	Features Detected	Extent of Automation	Imaging modalities	Reference
Watershed, dynamic programming	G	C,CP	F		[116]
Robust Edge Detection	L,G		F	F	[55]
Region growing across sections	G	C	S	LS	[72]
Adaptive smoothing, watershed	L	C	S	LS	[109]
Skeleton thresholding, edge detection	G	C,CP	S	F	[92]
Thresholding and thinning	L	C,CP	S	BF	[93]
Skeletonization, thresholding	G	C, CP	F	F	[99]
Skeletonization, snakes	L	C, CP, R	S	LS	[106]
Tracing with directional kernels	L	C, CP, R	F	M	[5, 4, 6, 7]
Approximation of Gaussian kernel	L	C,CP	F	F	[134]
Local Hessian matrix, Gaussian kernel	L	C, CP	F	F	[129]
Active contour, snakes	L	C, CP, R	S, F	LS	[35]
Modified Active Contours	L	C, CP, R	F	M	[119, 27, 91]
Marked Point Process	L,G	C, CP, R	F	M	[17, 18, 19]

Table 2.1: Automated neuronal reconstruction algorithms

along the neurites with their positions, radius, connectivity and process type [132]. This vector style of representation (refer Figure. 1-1-SWC format) is very concise. Neuronal processes can also be captured by volume or surface encoding [133]. The following sections summarizes the existing algorithms for neuronal network extraction (see Table 2.1 for summary[1]).

[1]Local/Global Gradients: L, local; G, global. Features Detected: C, centreline; CP, critical points; R, radius. Extent of Automation: F, fully; S, semi-automatic Imaging modalities: M, multi-modal; LS, laser scanning; F, Flourescence; BF, bright-field; C, confocal; MF, multi-photon; 2P, two-photon

2.3.1 Thresholding and region-growing

Thresholding and region-growing are some of the traditional segmentation methods adopted for neurite tracing in Light Microscopy images. Intensity based thresholding [65] and adaptive thresholding [124] are among the simplest strategies to segment neuronal structures. Region growing along the neuronal structures from given seed points combined with edge-detection based stopping criteria has been proposed by Lu *et al.* in [72]. However, these methods are error prone and in case of inhomogeneity in neuronal structures, and insufficient contrast with the background, fails, making user intervention inevitable.

2.3.2 Mathematical morphology and skeletonisation

The neurite centreline provides the necessary data to obtain a compact description of the branching topology. Hence algorithms aimed at extraction of neurite center-line are abundant in the literature. Skeletonization methods [48, 124, 101]; medial axis extraction [4, 84]; distance transform field [131] watershed segmentation are used to extract neurite center-lines. Generally, these methods require an initial good segmentation which is difficult to achieve. These method apply 3-D deconvolution to correct the images followed by adaptive 3-D skeletonization method, and graph-theoretic representation of nodes as branch, terminal points and paths interconnecting these points. However, with increasing size of data sets deconvolution is infeasible w.r.t 3D data sets to sharpen images that suffer from fast motion or jiggles during capturing or restore image from PSF distortion. These methods often result in isolated branch segments and dis-

connected trees. As a result, they require complex constraints for keeping check on number of connected regions. Post processing steps involving pruning and filling strategies are needed to correct the results [72, 127, 96]. Mathematical morphology operators like "erosion" to remove spurious branches and "dilation" to join disconnected branches are applied.

2.3.3 Sequential tracing

One common property of all neuronal structures is that they all exhibit roughly tubular shapes. This property is exploited to find location of tubular structures in the data to limit the processing area using methods like Frangi vessel-ness measure [36], and Hessian or Jacobian based ridge filter analysis of critical points. The Eigen values of the local hessian is used to approximate the normal and the tangent direction. The shifted normal plane bounds the region for the search of next neurite point. For Frangi vessel-ness measure the second order local structure of an image (Hessian) is examined with the purpose of developing a vessel enhancement filter. The vessel-ness measure is obtained on the basis of all eigenvalues of the Hessian. Given the centerline, there exists various algorithms to estimate the local radius, such as the Rayburst algorithm [123].

In sequential tracing local models of the neurite are sequentially fit to image data starting from a detected set of seed points. Commonly, multi-scale Eigen analysis [36], in combination with gradient information [56] or intensity ridge traversal [11] are used to detect seeds on tubule centerlines. These filters find voxels maximizing a vesselness measure by collecting responses over a range of filter scales. However, a major drawback of this method is the detection fails

at the junctions and branching points where the structures deviate significantly from the tubular shape. Moreover, the performance is sensitive to the scale of the edge detectors and fails for branches that are significantly thicker. These methods are susceptible to discontinuities (gaps and holes) of the foreground and produce fragmented traces that require additional post-processing procedures for curve completion.

2.3.4 Min cost path

This class of algorithms use a variety of energy minimizing functions to fit local image data and curve regularity. The optimal neuronal trees are determined by a Djikstra-like minimal cumulative cost strategy. Some of the popular choices are parametric deformable active contours or snakes, level-sets [88], deformable cylinders, mathematical neurite kernels; fitted between critical points based on the intensity values in the data and some prior information (regularization term). Automatic neurite tracing algorithms emulate the strategies adopted by a human operator. Manual tracing generally starts from given critical points like terminal points or the cell body and traces out the neurite. Kernels or templates corresponding to neurite segments are iteratively tested at different orientations at the end of the already detected neurite process along the lengths of the neurons until end points are detected. The major advantage of this approach is that computation is directed only in the immediate vicinity of the extending neurite, thus greatly reducing the overall computational load in CPU and memory [5, 6, 7, 134]. This makes them more attractive choices for scaling to larger data sets.

The seed points, for example end points, branch points and inflection or ridge points, can be user supplied or automatically detected using machine learning techniques like used in [100]. Some of the recent efforts have focused on detection of terminal nodes in volumetric neuronal data to initialize automatic tracing methods [68]. The extent of automation can be determined by how the seed points are generated. While traditional methods used expert supplied seed points, full automation of seed point selection is also possible [27]. The quality of the seed points is, however, of utmost importance. Experience shows that full automation cannot match the quality of user supplied seed points. Seed point selection can be tricky and depends on the experience level of the user. Hence, it is important to strike a balance between automation and the quality of seed points. This choice affects the robustness of the solution verses scalability to full automation.

Of the above enumerated categories, the first two classes of algorithms were mainly successful with early, low-resolution, 2D microscopy data. In view of the growing size of data sets, it is predicted that stochastic data exploration strategies rather than deterministic ones, combining both local and global image evidence, will gain popularity and relevance [79]. Methods on recent complex and large neuronal data sets focus on various statistical machine learning approaches such as multi-layer neural networks with receptive fields [29]. Lately, the neuron segmentation problem is increasingly being viewed as a graph theoretic representation problem ensuring global connectivity [85]. In [115], too the authors present a stochastic Ant colony Optimization strategy to sample connections between a set of detected nodes and generate the optimal Minimum

Spanning Tree. Another novel and revolutionary effort at large scale neuron reconstruction is the Eyewire project using crowd sourcing [3]. A team at MIT labs developed a game Eye-wire which challenges the players to map 3D neuronal circuits in the retina.

Recent efforts at neuron reconstruction is focused not only on segmentation of neuronal branches but also extracting analytical parameters for neuron shape quantification. The neuronal structure is the primary tool for enumerating neuron types. The most obvious criterion of choice for classification of neurons is their functionality. But very little is known about the nervous system in general. The structure of neurons have been found to have an intimate relation with its functions, and further other characteristics like electrophysiological responses and genetic expressions have also been known to be influenced by neuron structure [112]. [14, 104, 87, 86, 16, 82] have proposed methods to quantify neuron morphology in order to differentiate neurons in the shape space.

2.4 Global versus local algorithms

The various neurite tracing methods can broadly be classified as local tracing and global segmentation methods. The first category refers to algorithms that explore an image in the vicinity of relevant structures instead of processing the entire image. The basic idea of this approach is to determine whether the next point is part of the neuronal process. Region growing [72], active contour based propagation [74, 27]; cost based path fitting between start and end points [13] are examples of "local explorative" algorithms. Local methods are computationally

Global algorithms	Local algorithms
• Neuronal Reconstruction	• Neurite Tracing
• Computationally intensive; high memory requirements	• Less intensive computation; dependence on seeds
• Results in less cases of disconnected components	• Can interpolate only through small intensity gaps
• Exploits more image evidence using optimization like MCMC, ACO etc.	• Localized search; tracing errors result in large topological perturbations

Table 2.2: *Contrasting global and local neuronal reconstruction methods.*

inexpensive in both CPU and memory. The other advantages are that these local methods are faster and are more attractive for parallelization. Local algorithms can successfully interpolate through small intensity gaps along branch lengths but larger discontinuities result in disconnected components. The disadvantage with local tracing are small errors get propagated and magnified, resulting in large topological perturbations of the neuron tree morphology.

Global algorithms are typically computationally expensive as they consider the evidence from the whole image but only a small fraction of the data has the relevant neuronal structures. Skeletonization, filling and pruning [92, 99] are examples of global segmentation schemes. Global methods are, however, better at avoiding disconnected components by sampling evidence from the entire data. Processing the entire data allows to intelligently join the close lying disconnected components. But this makes them slower and more computationally intensive than the local methods. In order to handle this computational

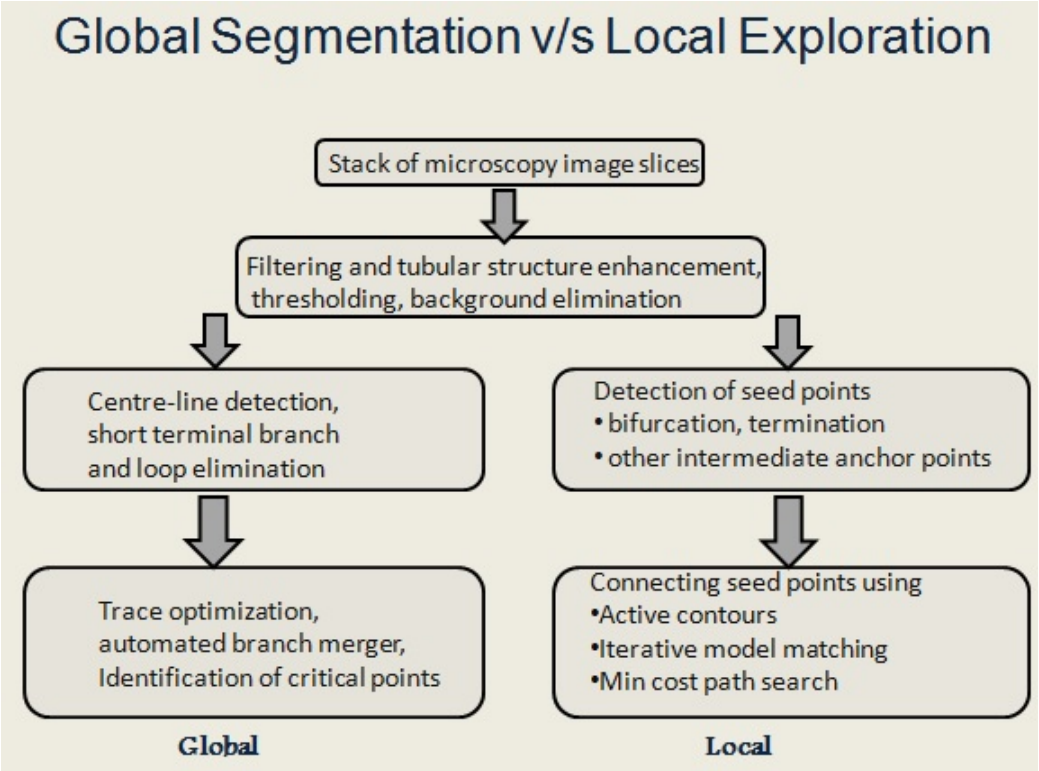

Figure 2-2: *Flow of neurite tracing algorithms.*

challenge, in global methods, segmentations are initialized roughly at low magnification data and then further optimized in a multi-scale framework.

There is a trend of transition from manual to semi-automatic approaches [72, 65] over the past decade. A comprehensive survey of all issues related to automatic neuronal reconstruction can be found in the following papers [79, 34, 107]. The papers present a survey of the existing algorithms and tools and lists their merits and demerits.

2.5 Validation tools and metric

Validation methods and metrics for automated reconstruction present a point of contention in the field. The most common method for validation of automated reconstruction is to compare with Gold Standard reconstructions. Mostly, manual reconstruction by the experts are accepted as the Gold Standard. Sometimes, neuronal morphology databases comes with synthetic data. In such cases the the reference reconstruction used to generate the synthetic data is taken as the Gold Standard. However with real data, the Gold Standard manual reconstruction is treated as the ground truth. Hence, if the manual reconstruction contains errors, even when the automated algorithm performs better, it is not reflected in a comparison against the Gold Standard. Once the Gold Standard is fixed, there are multiple ways to compare the automated reconstructions.

Traditionally, scoring the reconstruction is done by checking whether it lies within the scope of inter and intra operator variability [80, 37]. Some studies score the automatic reconstructions according to percentage of deviation from manual reconstruction called the constrained *Tree Edit Distance* (TED) [43, 50]. The standard morphometrics for axonic and dendritic tree quantification are total length, branch number, branching pattern, mean diameter, centre-line deviation. For example, the DIADEM (short for Digital Reconstruction of Axonal and Dendritic Morphology) Challenge [42] that brought together the most challenging neuronal morphology reconstruction data from Confocal, Brightfield and Fluorescence microscopy also established its own metric. The metric scored generated reconstructions against gold standard manual reconstruction on the basis of location of critical points like inflection nodes, terminal nodes

and branch nodes; branching hierarchy and the inter-nodal distance [41]. It calculated the precision and recall of both centreline position and connectivity. Other tools focus, such as *NetMets* focus on comparing distances between generic network graphs [77, 78]. It compares the spatial geometry and connectivity of two interconnected graphs, like those produced using neuron and vascular/microvascular segmentation. Additionally, NetMets provides tools for visualizing differences between graphs, including color maps highlighting differences between geometric features and edge mapping to indicate differences in connectivity. *Path2path* [15] is another hierarchical path analysis tool for neuron matching for classification based on shape quantification.

2.6 Discussion

The study of neuronal structure and neural circuits is still at a nascent state. It is expected to open up many new research directions in the future [69]. 4D images, i.e., 3D time lapse images of the neuronal morphology are relevant for studying development, plasticity degeneration and regeneration of the nervous system. Development of super-resolution optical microscopy will enable tracing sub-cellular structures of various proteins and organelles at synaptic sites. While deterministic structural analysis methods are currently focused at studying axonic projections in relatively small area, the ultimate goal is to study the entire neural circuity. That would require reconstruction at sub-cellular scales Electron Microscopy data of synapses and eventually exploring at extra-cellular level the connectomic pattern of the nervous system.

Chapter 3

Detection of 3D Tubular Structure Networks

Contents

Tubular structures are frequently encountered in biomedical images. The centerlines of these tubules provide an accurate representation of the topology of the structures. We introduce a stochastic Marked Point Process framework for fully automatic extraction of tubular structures requiring no user interaction or seed points for initialization. Our Marked Point Process model enables unsupervised network extraction by fitting a configuration of objects with globally optimal associated energy to the centreline of the arbors. For this purpose, we propose a special configuration of marked objects and an energy function well adapted for detection of 3D tubular branches. The optimization of the energy function is achieved by a stochastic, discrete-time multiple birth and death dynamics. Our method finds the centerline, local width and orientation of neuronal arbors. The proposed model is tested on 3D light microscopy images from the DIADEM data set with promising results.

3.1 Overview

The rapidly evolving field of imaging generate huge volume of rich and heterogeneous data. Manual analysis of such data is prohibitively expensive in terms

of expert man-hours required besides presenting considerable inter-operator variability. Tubular structures abound in biomedical images. Vasculature networks in retina and tumors, coronary arterial angiograms, bronchial trees are some commonly encountered examples. In our work, we focus our attention on neuronal morphology imaged by various 3D microscopy techniques. At present, high resolution, high content 3D image data is becoming more and more prevalent. Hence, we focus on developing a fully automatic, stochastic rather than deterministic data exploration strategy, combining both local and global image evidence.

3.1.1 Tubular structure detection

Neurite tracing methods connect paths of maximum neuriteness voxels locally between sets of seed points to extract the global neurite structure. A common drawback of existing methods is their dependence on seed points [114]. Often, manual intervention is required to select the optimal seed points. Unavailability of seed points can even lead to entire branches going undetected. Not only for neurons, seed points are a relevant concern for all kinds of tubular structure extraction scenarios [53]. This topic has been extensively researched for over two decades. In the literature it is given various names such as tube detection filters, vessel detection filters, medialness filters etc. Over the years the application data has grown in volume and dimension (2D to 3D) and complexity. Most of these methods perform a shape analysis for each image voxel for a medialness or tube-likeliness measure. Ideally, this is maximum when computed at the correct local scale at the centreline of the tubule.

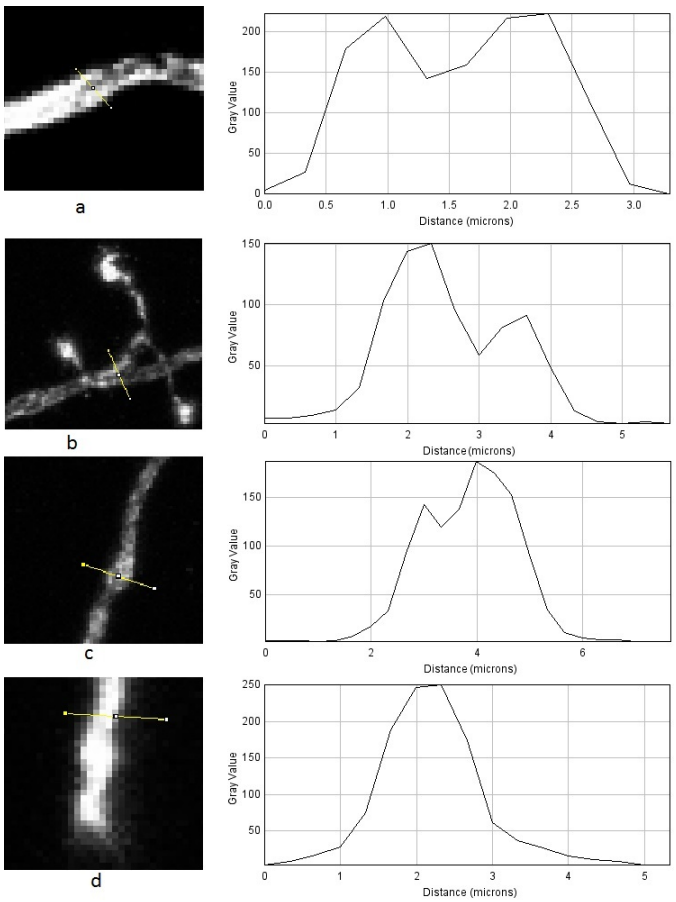

Figure 3-1: *Variation of intensity profiles across the cross-sectional scan lines.*

Commonly, multi-scale Eigen analysis [36], in combination with gradient information [56] or intensity ridge traversal [11] are used to detect seeds on tubule centerlines. There are mainly two categories of approaches the central medialness filters and offset medialness filters. The former focuses on image information at central voxel while the latter takes into account information away from the center voxel at the tube radial edges too. The former rely on Eigen analysis of Hessian matrix for identifying typical structural properties such as large variance in two directions along tube cross-sections and low variance in

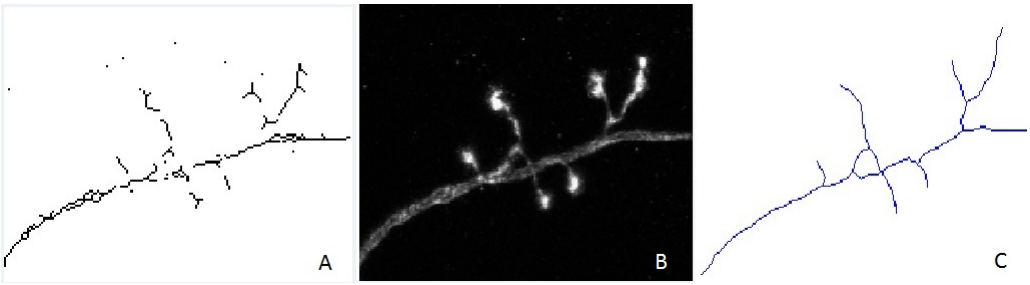

Figure 3-2: *Non-maxima suppression of vesselness measure versus result by our proposed method.*

the tube tangent direction. In Gaussian scale space tubular structures present height ridges when scales are adapted to tube dimensions. The offset medialness filter in addition to second order derivatives (Hessian) use first order derivatives (gradient vectors) at tube radii for more robust detection of tubular structures.

These filters find voxels maximizing a vesselness measure by collecting responses over a range of filter scales. They are computationally intensive as multiple scales and orientations of the filters are convolved with the image data at every voxel. With increasing volume of data and considering 3D orientations of neurites, deterministic filter response maximization is an infeasible option, considering the huge solution space that is required to be explored. A common drawback of Hessian-based filters, such as the Frangi vesselness filters, is that they fail at critical junctions and bifurcations where the neuronal morphology deviates significantly from expected tubular cross-sections. They are also sensitive to presence of adjacent structures. Scale-orientation space non-maxima suppression fails to generate a connected topological centreline of the neurite branches. It is very difficult to explicitly model the variety of artifacts generated due to inhomogeneity in branch labeling and noise injection during imaging.

Figure 3-1 demonstrates the variation of intensity profiles encountered in branch cross-sections. The left images show scan lines in yellow across branch cross-sections. The right images show the corresponding intensity profiles across the scan lines. We see that the intensity ridges often do not correspond to geometric centre lines in case of irregularly stained neurons as is expected in the ideal situation.

Recently various supervised machine learning techniques modeling the centreline detection problem as a classification task have been proposed in the literature [44]. These methods learn binary classifiers for centreline and non-centreline pixels. Although these methods perform better than classification based methods for direct segmentation of tubular objects, they are not strongly discriminative about pixels close to centerlines. Hence, automatic seed selection by these techniques generate sub-optimal seeds. Moreover, their dependence on availability and quality of learning data, make them an unattractive choice. Figure 3-2 demonstrates the superiority of our proposed method. The middle section is a maximum intensity projection of the Olfactory Projection Fibre (OP7), the left image is the result of non-maxima suppression of vesselness measure, and the right image is the result by our proposed method. We solve this problem by reformulating neuronal morphology as a special configuration of an object process. It offers the advantage of modeling a random set of points describing a spatial distribution of data by means of geometric shape and object interaction priors. Thus the neuronal structure is described by a optimal configuration of the marked point process objects fitted to the tubular branches. The centreline and the corresponding local scale and orientation information can be easily

Figure 3-3: *The detected network with our proposed MPP configurations on OPF.*

obtained in an automatic, unsupervised manner requiring no user interaction. Refer Figure 3-3 for overview of our method. It shows the minimum intensity projection of intensity inverted (for ease of visualisation) Olfactory Projection Fibers (OPF) data obtained by confocal microscopy. The extracted network with the proposed model visualised on a projection of the OPF data. We restrict overlap of object to have a sparse density on the branches and yet get a sense of the continuity of the neurites.

3.1.2 Bayesian learning and MCMC

Markov Chain Monte Carlo (MCMC) simulations are widely used for approximate counting problems, Bayesian inference and as a means for estimating very high-dimensional integrals. As such MCMC has found a wide variety of applications in computational biology and biomedical analysis. For high resolution, high content microscopy data such as neuronal morphology data, MCMC is a computationally expensive nondeterministic iterative technique for sampling from a probability distribution that cannot easily be sampled from directly. In-

stead, a Markov Chain is constructed that has a stationary distribution equal to the desired distribution. We then sample from the Markov Chain, and treat the results as samples from our desired distribution. At each iteration a transition is proposed to move the Markov Chain from state $\mathscr{S}_i$ to some state $\mathscr{S}_{i+1}$, normally by making small alterations to $\mathscr{S}_i$. The probability of applying this proposed move is calculated by a transition kernel constructed in such a way that the stationary distribution of the Markov Chain is the desired distribution. These methods typically allow the user to define priors modeling expected structural and shape properties besides using radiometric properties from image data. The probability for advancing the chain to state is based on how well the new state fits with the prior knowledge — what properties the target configuration is expected to have—and the likelihood of the new state considering the actual data available.

3.1.3 3D marked point process model

We develop an efficient Marked Point Process (MPP) framework for extraction of neuronal structures from 3D data without greatly increasing the computational complexity of sampling and estimation. Firstly, spheres are chosen as MPP objects, in particular because it gives one dimensional object space but allows to simultaneously extract center line, size and local orientation of branches. Secondly, to find the Maximum A Posteriori (MAP) estimate of the optimal configuration, we sample from the object configuration space using a Multiple Birth and Death (MBAD) dynamics embedded in a Simulated Annealing scheme [32]. The MBAD dynamics reduces computational cost over traditional Reversible

Jump Monte Carlo Markov Chain samplers by avoiding proposal kernel computations and leads to faster convergence.

In the Marked Point Process (MPP) literature, previous works on network extraction, such as coronary network extraction from angiograms [59],[111] and road network extraction from satellite data [60] in remote sensing, used line segments as objects. More complex polyline objects were employed in [60] with improved accuracy. Line segments are defined by the position of their midpoints, length and orientation parameters. On 3D data, however, considering line segments or cylinders to approximate the tubular structure would lead to four or five parameters (marks) respectively to define each object, thus increasing the object space dimension. Hence, a Point Process model was proposed for efficient road network extraction from 2D aerial and satellite images [23]. Neurite dimensions, however, are found to vary significantly from root to the terminals necessitating a variable object model, making a fixed dimension object space impossible.

Hence, we adopt a stochastic framework that enables a flexible object model along with incorporation of prior shape and object interaction information which is partly introduced in [17]. We introduce special configurations of MPP objects corresponding to neuronal morphology and adapt an energy function designed for extraction of 3D tubular structure patterns. then we perform a search in a high dimensional solution space. We develop an efficient Marked Point Process (MPP) framework for extraction of neuronal structures from 3D data without greatly increasing the computational complexity of sampling and estimation. Firstly, spheres are chosen as MPP objects, in particular because it gives one

dimensional object space but allows to simultaneously extract center line, size and local orientation of branches. Secondly, to find the Maximum A Posteriori (MAP) estimate of the optimal configuration, we sample from the object configuration space using a Multiple Birth and Death (MBAD) dynamics embedded in a Simulated Annealing scheme [32]. The conventional Reversible Jump Markov Chain Monte Carlo (RJMCMC) sampler allows perturbation of only a few objects in the current configuration and hence is slow to converge. In contrast, in MBAD multiple random objects are proposed and removed independently and simultaneously in each iteration, which greatly reduces computational cost and speeds up convergence. Recently, Graph Cut optimization schemes Multiple Birth and Cut (MBC) were proposed for MPPs [39] as an alternative for MBAD optimization with fewer parameters and more stable convergence. Although MBC has several advantages over MBAD, it is very difficult to set up our energy function for a graph cut optimization. The class of energy functions MBC can deal with are ones satisfying the sub modularity constraint of pairwise interaction terms [54]. However, in our proposed energy function for neurite tracing, the multi-element interaction term is very important for accurate detection of critical nodes.

3.2 Marked point process: notations, definitions

The *Point Process* models were first introduced in [12] to exploit random fields whose realizations are configurations of random points describing a spatial distribution of data. Under this view, images are considered as configurations of a

Gibbs field. The implicit assumption behind the probabilistic approach in image analysis is that, for a given problem, there exists a Gibbs field such that its ground states represent regularized solutions of the problem. [117] and [30], are good resources for complete details of Marked Point Processes and their applications. These methods are particularly useful for addressing spatial relation and configuration modeling purposes for high dimensional, high resolution image data. These methods have been used for various applications such as counting in flamingo colony [38], tree identification [58] from aerial and satellite images, crowd counting [40], vasculature tree extraction [61],[111] etc.

3.2.1 From point to parametric marked point process

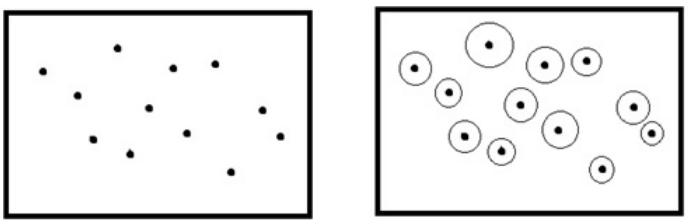

Figure 3-4: *Point process and marked point process.*

In Figure 3-4, we see a Point Process(PP) modeling spatial distribution of data — a configuration of points on $[0,X] \times [0,Y]$ and a Marked Point Process (MPP) modeling spatial distribution of data and geometry — a configuration of circles with centres on $[0,X] \times [0,Y]$ and radii from $M = [r_{min}, r_{max}]$ as marks. We consider a point process $\mathscr{X}$ existing in $K = [0,X_{max}] \times [0,Y_{max}] \times [0,Z_{max}]$, where K is a bounded, connected subset of $\mathbb{V}^3$, the image domain. Marked point process (MPP) is an augmented point process, where each point x_i is associated

with additional parameters (marks) m_i to define an object $\omega_i = (x_i, m_i)$. Here, $x_i \in K$ and $m_i \in M$ and the marked point process $\mathscr{Y}$ is defined on $K \times M$. A countable, unordered set of points in $\mathscr{Y}$ is called a *configuration*. The *configuration space* of the objects is given by:

$$\Omega = \cup_{n=0}^{\infty} \Omega_n, \tag{3.1}$$

where Ω_0 is the empty set, each $\Omega_n, n \in \mathbb{N}$ is a configuration containing n objects and $\gamma_n \in \Omega_n, \gamma_n = \{\omega_1, \ldots, \omega_n\}$. Note that n can be arbitrary, and in the following sections of the paper the elements of configuration $\gamma \in \Omega$ (with an arbitrary number of elements) will be denoted as $\{\omega_i\}$, where $i = 1 \ldots n$.

3.2.2 Gibb's distribution and energy of configuration

The Marked Point Processes are defined by their probability density w.r.t. the reference Poisson process. Given a real, bounded below function $U(\gamma)$ in Ω, the Gibbs distribution μ_β in terms of the density $p(\gamma) = \frac{d\mu_\beta}{d\lambda}(\gamma)$ w.r.t. Lebesgue-Poisson measure λ on Ω is defined as:

$$p(\gamma) = \frac{z^{|\gamma|}}{Z_\beta} \exp[-\beta U(\gamma)]. \tag{3.2}$$

Here, γ represents the configuration of objects, $z, \beta > 0$ and Z_β is a normalizing factor:

$$Z_\beta = \int_{\gamma \in \Omega} z^{|\gamma|} \exp[-\beta U(\gamma)] d\lambda(\gamma). \tag{3.3}$$

These models are defined on huge configuration spaces over unknown number of objects. The configuration space is then the union of the spaces with a fixed number of objects. Markov Chain Monte Carlo (MCMC) simulations are widely used as a means for estimating very high-dimensional integrals. The principle is to define a Markov Chain converging to a target distribution. By including a simulated annealing scheme, the chain converges to the Maximum A Posteriori, which is the configuration which maximizes the target distribution. To define the Markov chain, an iterative process is computed. At each step, a new configuration is proposed following the so-called proposal density. This new configuration is accepted with a probability depending on an acceptance ratio which involves the target and the proposal distributions.

In the Gibbs energy model, the optimum object configuration $\hat{\gamma}$ corresponds to the minimum global energy, where γ represents the configuration of objects:

$$\hat{\gamma} = \arg\max_{\gamma} p(\gamma) = \arg\min_{\gamma} U(\gamma). \tag{3.4}$$

The problem of object extraction in Bayesian inference is formulated as an inverse problem. It aims to find some model parameters γ from the observed data D. It is solved as an energy $U(\gamma)$ optimization problem in the space of model parameters. Bayesian inference framework typically involves a likelihood term or data energy response to fit the model to the data and a regularization prior to embed expected structural constraints. The parameters are finally estimated using a Maximum A Posteriori (MAP) estimate:

$$U(\gamma) = w_d U_d(\gamma) + U_p(\gamma), \tag{3.5}$$

where U_d represents the data energy, U_p is the object interaction prior energy w_d is the relative weight between the data and the prior energies. We seek to minimize the global energy $U(\gamma)$. To find the minimizer $\hat{\gamma}$ means to find the number n of objects in the required configuration and to find positions of all n objects in the configuration $\hat{\gamma}$.

To fully appreciate the power of the MPP framework, we should view it in comparison to the more popularly used Markov Random Fields (MRF) models. The MRF is a more general framework — they could be pixel-wise ones, or point configuration models, and can be applied to various image processing problems. The crucial idea behind the MRF modeling is that there exist a Markov random field such that the desired image will be a ground state of this field.

Markov point process models is a class of MRF models with a configuration space, where configurations are unordered sets of points/objects with a corresponding probability distribution on this configuration space. In our approach it is a Gibbs field. This class of models can give a more qualitative result for a certain image processing problems such as object detection, counting.

The key difference is that for objects model with MRF and graph optimization, the number of objects should be known in advance and is fixed for ever. Whereas in the case of MPP, the number of objects can vary at each iteration of the optimization done via RJMCMC (such as Metropolis-Hasting-Green dynamics) and one need not know the total number of objects in advance.

3.3 Energy model for 3D neuronal networks

Our aim is to extract the neuronal branches by generating a configuration of objects fitted to the points of maximum medialness measure on the image volume. For this purpose, we adopt spheres as objects $\omega_i = (x_i, r_i), x_i \in \mathbb{V}^3, r_i \in [r_{min}, r_{max}]$ and $\omega_i(x_i, r_i) = (y_i : |x_i - y_i| \leq r_i)$ where y_i are voxels in the image domain $\mathbb{V}^3$. The stochastic optimization and random sampling strategy of the object configuration space, which also defines our filter space, extracts an optimal configuration of objects whose radii correspond to the scales of the filters maximizing the responses at their center voxels in the image data. In the following section we describe each of the energy components in detail.

3.3.1 Data Energy

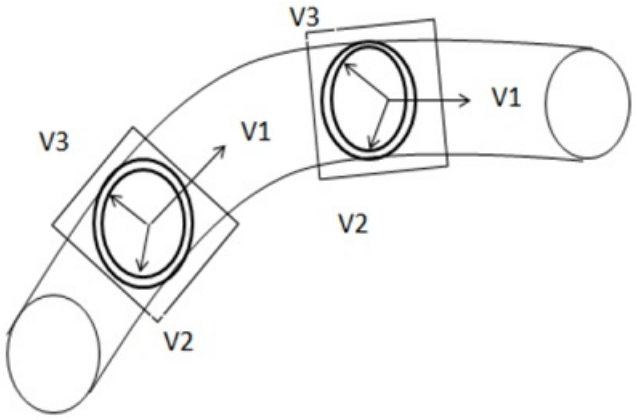

Figure 3-5: *Illustration of adopted neurite-ness function.*

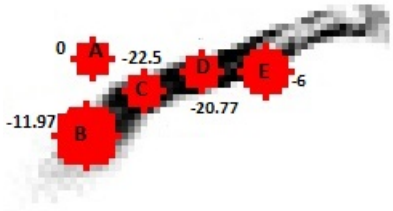

Figure 3-6: *The red circles are the cuts of our spherical objects on 1 slice of data.*

The total data energy is a sum of data energy responses of individual objects:

$$U_d(\gamma) = \sum_{\omega_i \varepsilon \gamma} U_d(\omega_i). \tag{3.6}$$

Our data energy response is based on the tubularity filter proposed in [98]. The Hessian is a second order partial derivative of image data containing local structural information. Its principal components determine the tangent direction and normal plane of the local neurite structures. The scale of the Hessian σ_H is uniformly sampled from the radius range $[r_{min}, r_{max}]$. The medialness measure $M(\omega_i)$ is obtained by taking an integral of the image gradient at scale σ_G along the circumference of the cut of the spherical object on the normal plane defined by $V1$ and $V2$:

$$M(\omega_i) = |\frac{\pi}{2} \int_{\theta=0}^{2\pi} \nabla I^{(\sigma_G)}(x_i + r_i V_\theta) d\theta|. \tag{3.7}$$

Here, $V_\theta = cos(\theta)V_1 + sin(\theta)V_2$ is a rotating phasor in the normal plane sampling gradient information at radial distance r from the center $x_i = [x, y, z]^T, x_i \in \mathbb{V}^3$ of the object. The medialness measure varies greatly for thin or weakly contrasted neurite branches, a common occurrence in case of microscopy images

due to injection of noise and non-homogeneous staining of the neurons. Thus, a user defined optimal global threshold to reject structured noise and background artifacts is difficult to obtain. So, to discriminate between "good" and "bad" objects an adaptive thresholding of the medialness response is performed based on the gradient response at the tube's center $M_c(\omega_i) = |\nabla I^{(\sigma_H)}(x_i)|$. The data energy term is then defined as follows:

$$U_d(\omega_i) = \begin{cases} -(M(\omega_i) - M_c(\omega_i)), \text{if} M(\omega_i) > M_c(\omega_i) \\ 0, \text{otherwise.} \end{cases} \tag{3.8}$$

Figure 3-5 shows the adopted neurite-ness function. The eigen analysis at the scale of object radii determines the orientation of branch and the perpendicular normal plane on which we average the edge response. In Figure 3-6, the red circles are the cuts of our spherical objects on 1 slice of data. High negative energies indicate "good" objects (e.g., objects B,C,D), i.e., objects situated on the branch centreline and the same size as the local branch width. "Bad" objects, for example, on the background (object A) or not centered correctly on the branch (object E) have low probabilities of survival in the configuration during the energy minimization scheme.

The prior $U_p(\gamma)$ in the energy function (Equation 3.5) consists of two terms $U_i(\gamma)$ and $U_c(\gamma)$.

3.3.2 Prior I

This term is a pair-wise interaction potential for objects in each other's zone of influence:

$$U_i(\gamma) = \sum_{\substack{\omega_i,\omega_j \in \gamma; \\ \omega_i \sim \omega_j}} U_i(\omega_i, \omega_j), \tag{3.9}$$

where the operation $\sim$ is defined as a neighborhood relation:

$$\omega_i \sim \omega_j = |\omega_i, \omega_j \in \gamma : |x_i - x_j| < tD|, \tag{3.10}$$

and D is distance between centers of objects ω_i and ω_j, and $t \in \mathbb{N}$. It avoids crowding together of spheres along the neuronal processes and favors continuity of network by merging of close lying disconnected fragments, a common occurrence in microscopy data due to inhomogeneity in branch intensity and poor contrast with background. Around every object exists an immediate zone of repulsion followed by a concentric zone of attraction. Two energy potentials are defined: U_+ is repulsive in nature to penalize objects lying too close to each other, and U_- is attractive in nature to favor objects in reasonable distances of each other.

$$U_i(\omega_i, \omega_j) = \begin{cases} U_+, \text{ if } d < d_r \\ U_-, \text{ if } d_r \leq d \leq d_a \\ 0, \text{ if } d > d_a. \end{cases} \tag{3.11}$$

Here, d is the Euclidean distance between the centers of the spheres; d_r and d_a ($d_r < d_a$) are respectively the repulsive and attractive distances, d_r, d_a are multiples of $r_i + r_j$. By varying d_r and d_a, density of spheres along the neuronal

branches can be controlled.

3.3.3 Prior II

We propose a second prior — $U_c(\gamma)$, which is a multi-object interaction potential, incorporating constraints on the connection among objects:

$$U_c(\gamma) = \sum_{\omega_i \in \gamma} U_c(\omega_i). \tag{3.12}$$

Depending on the number of objects $k(\omega_i) = |\omega_j \in \gamma : d_r < d(\omega_i, \omega_j) < d_a|$, in the neighborhood, the prior term can also be used to determine branching points and termination points along neuronal processes.

$$U_c(\omega_i) = \begin{cases} E_1, \text{if } k(\omega_i) = 0 \\ -E_1, \text{if } k(\omega_i) = 1 \\ -E_2, \text{if } k(\omega_i) = 2,3 \\ -E_2, \text{if } k(\omega_i) = 4 \\ E_1, \text{if } k(\omega_i) > 4. \end{cases} \tag{3.13}$$

This association of favorable energy potentials E_1 and E_2 with particular local sub-configurations encourage accurate detection of critical nodes. At the same time, it discourages isolated objects in the configuration, which are likely to correspond to cell nuclei or other such background structures.

Algorithm 1 Multiple Birth and Death

Initialization
Discrete time-step $\delta = \delta_0$; inverse temperature $\beta = \beta_0$; Poisson mean z_0; Parameters of energy function and the empty start configuration.
Now, alternate between birth and death step until stop condition is met:
Birth
(a) Generate a configuration of spheres $\gamma \in \Omega$, from the Lebesgue-Poisson distribution with intensity $z = \delta z_0$ for centers, with independent radii uniformly distributed on $[r_{min}, r_{max}]$. A hard core repulsion δ_ε is added with ε equal to one pixel.
(b) $\gamma' \cup \gamma''$: Add the new set of objects γ'' to the "surviving" ones $\gamma' \subset \gamma$ to get current configuration γ.
Death
(a) Sort the objects of the current configuration according to their data energy $U_d(\omega_i)$, for the purpose of accelerating computation;
(b) Each object ω_i in the configuration γ, is removed with probability $p(\omega_i, \gamma) = \frac{\delta \alpha_\beta(\omega_i, \gamma)}{1+\delta \alpha_\beta(\omega_i, \gamma)}$;
Termination
Terminate if all and only objects added in the birth step of current iteration are removed. Else, update γ, decrease $\delta, \frac{1}{\beta}$ according to a geometric annealing schedule and go to the birth step.

3.4 Optimization

The main idea of the proposed approach is to sample special configurations consisting of spherical objects and fit them to the microscopy data stacks to voxels of maximum neuriteness measures. These configurations are projected onto the image volume. The configurations are optimized by measuring the similarity between the projected model of the configuration and the neuronal data. A Gibbs energy is defined on the configuration space. The complexity of optimization of the global energy depends directly on the size of the sampling space of the objects, which we limit by the adoption of spherical objects, with a 1-

dimensional parameter space. The optimum global energy is defined over the space of union of all possible configurations, considering an unknown a-priori number of objects. To obtain the optimal configuration of the objects on the image data, we use MAP estimation (Equation 3.4). We sample from the probability distribution μ_β using a Markov chain of the discrete-time Multiple Birth and Death dynamics defined on Ω and apply a Simulated Annealing scheme. At every iteration, a transition is considered from current configuration γ to $\gamma^{'} \cup \gamma^{''}$ where $\gamma^{'} \subset \gamma$ and $\gamma^{''}$ is any new configuration. The corresponding transition probability is given by:

$$P(\gamma \to \gamma^{'} \cup \gamma^{''}) \sim (z\delta)^{|\gamma^{''}|} \prod_{\omega_i \in \gamma \setminus \gamma^{'}} \frac{\alpha_\beta(\omega_i, \gamma)\delta}{1 + \alpha_\beta(\omega_i, \gamma)\delta} \prod_{\omega_i \in \gamma^{'}} \frac{1}{1 + \alpha_\beta(\omega_i, \gamma)\delta}, \tag{3.14}$$

where $\alpha_\beta(\omega_i, \gamma) = \exp(-\beta(U(\gamma \setminus \omega_i) - U(\gamma)))$. The convergence properties of the Markov Chain to the global minimum under a decreasing scheme of parameters δ and $\frac{1}{\beta}$ are proved in [32]. The probability of death of an object depends on both the temperature and its relative energy in the sub-configuration; whereas, birth of object is independent of both energy and temperature and is spatially homogenous. In this way, the iterative process finds a configuration $\hat{\gamma}$ minimizing the global energy Eq. 3.5.

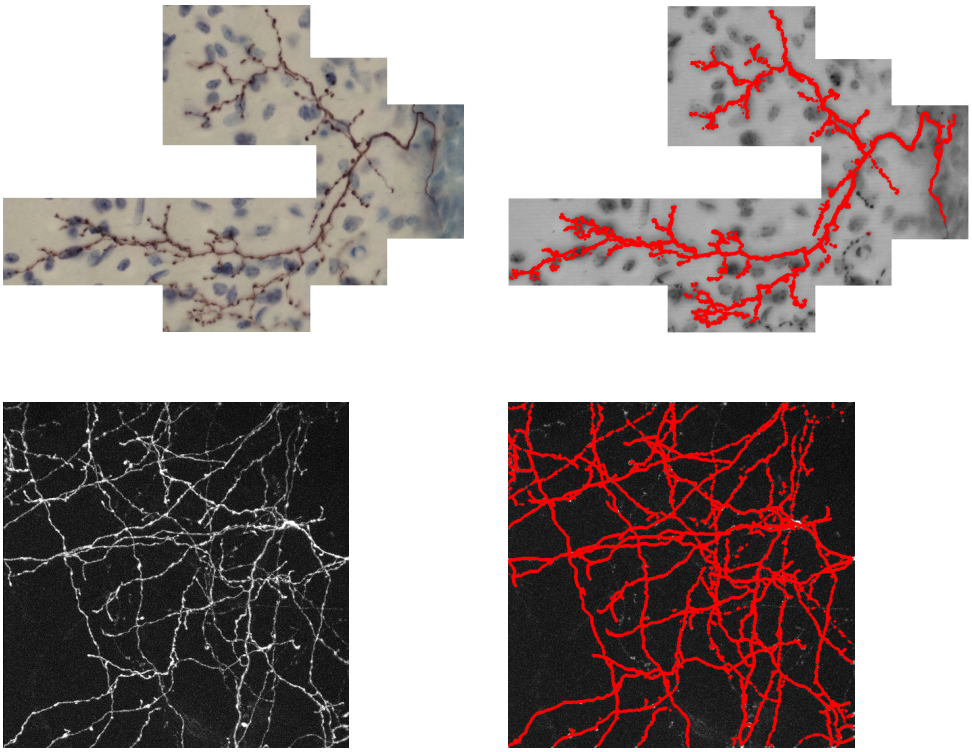

Figure 3-7: *Detected networks with our proposed MPP configurations on CCF and NL1.*

3.5 Results

3.5.1 Pre-processing

Our method is not sensitive to the initialization of the configuration and converges to the global minimum from any random initialization. But the structures of interest take up only a small fraction of the total volume of the data. In order to speed up convergence to the optimum configuration, the birth of the objects are restricted to a region of interest defined by the dilation of the maximum intensity projection of the original data stack. In case of Neocortical Layer 1

Axons obtained by 2-photon Laser Scanning microscopy and the Olfactory Projection Fibers data obtained by confocal microscopy, the neurite branches have good contrast with the background. But for the Cerebellar Climbing Fibers obtained by Transmitted Light Brightfield microscopy, a regular maximum intensity projection of the 3D stack presents not only the neurites of interest but also some structures having a contrast with the background. Moreover, as is typical of Brightfield images, for most of the volume the neurites have a fuzzy, out-of-focus appearance. Hence, we perform a color segmentation to weed out the background structures followed by a standard deviation projection to obtain a layered depth map to guide the birth of objects in the more relevant sections of the image data.

3.5.2 Evaluation

We test the performance of our proposed model on 3D light microscopy image stacks from the DIADEM Challenge database [21]. Refer Figure 3-7. The left top image shows the minimum intensity projection of Cerebellar Climbing Fibers (CCF) obtained by Transmitted Light Brightfield microscopy. The top right shows the neuronal network extraction with the proposed model visualised on a projection of the least noisiest channel of the CCF data. The bottom row left maximum intensity projection of Neocortical Layer 1 Axons (NL1) obtained by 2-photon Laser Scanning microscopy. The bottom right image shows the neuronal network extraction with the proposed model on the projection of the NL1 data. These results are obtained with a high density of objects, allowing

overlap to fully reconstruct the fuzzy and blurred segments of the neurites. Our unoptimized Matlab implementation takes 57 mins, 3 hrs 29 mins and 1 hr 33 mins to converge on NL1, OPF and CCF datasets respectively on Intel Core i7 processor, 3.4 GHz with 8GB RAM.

The *parameters of the priors* are set to: $U_+ = 10$, $U_- = -2$, $E_1 = 1.5$ and $E_2 = 2.0$. The *sampling parameters* are set experimentally as $\beta_0 = 1$ and δ_0 to approximately three to five times the number of objects expected in the final configuration. The objects are sampled uniformly from the radius ranges $[1,10], [1,3]$ and $[1,25]$ for OPF, NL1 and CCF data sets respectively. The deviation of the extracted points set (P) using our proposed model from gold standard manually delineated centerlines (G) is compared in Table. 3.1 in the following way :

$$max(P,G) = max(\min_{p\in P, g\in G}(f(p,g))), \tag{3.15}$$

$$avg(P,G) = avg(\min_{p\in P, g\in G}(f(p,g))), \tag{3.16}$$

$$err_r(P,G) = avg(|r_p - r_g|: \min_{p\in P, g\in G}(f(p,g))), \tag{3.17}$$

$$maxerr_r(P,G) = max(|r_p - r_g|: \min_{p\in P, g\in G}(f(p,g))), \tag{3.18}$$

where $f(p,g)$ represents Euclidean distance of the concerned points and r_p and r_g are radius at point p and g respectively. The units of reporting error are anisotropic image voxels. The errors are higher along the z-axis due to the differential resolution of original data. * indicates ground truth radius not available. Thus, our method produces an automatic and reliable extraction of neuronal morphology. It is robust to small branch discontinuities, intensity variations due to inhomogeneous labeling, noise and background interference. More than

Dataset	Resolution	Centreline deviation			Radius	
		$avg(P,G)$	$max(P,G)$	% under 2 voxel error	$err_r(P,G)$	$maxerr_r(P,G)$
OP1	512x512x60	0.9504	3.00	96.90%	1.07	3.64
OP4	512x512x67	1.02	3.72	92.88%	1.18	3.24
OP5	512x512x76	1.39	3.53	84.24%	0.99	1.98
OP6	512x512x101	1.34	3.62	88.28%	0.43	1.22
OP7	512x512x71	1.08	3.13	94.78%	0.61	1.72
OP8	512x512x85	1.41	3.28	95.52%	0.78	1.18
CCF1	6120x4343x34	2.67	6.5869	66.23%	1.7656	9
NC01	512x512x60	1.1398	2.0119	79.12%	*	*

Table 3.1: Evaluation of our proposed method against gold standard manual extraction.

accuracy of centreline detection, our emphasis is on obtaining a connected extraction of the neuronal branches. In the subsequent chapters of this thesis, we will demonstrate how this presents an accurate topological representation of the neuronal structures from the 3D data volume and aids in subsequent analysis.

We also perform comparison against state-of-the-art methods in Figure 3-8. We select representative methods from several categories of algorithms - the oriented optimal flux [63] an extension of hand crafted filters combining local Hessian matrix analysis and gradient information; a skeletonization based method [128]; and a learning based method that models centreline detection as a classification task [108]. We compute the deviation for the centreline points given by given by each of the methods against the gold standard manual reconstruction. Figure 3-8 shows the plot of the mean deviation and one standard deviation from the mean for all the methods. We see that the performance of MPP is superior compared to the other methods showing the least mean for euclidean deviation and also a small standard deviation overall.

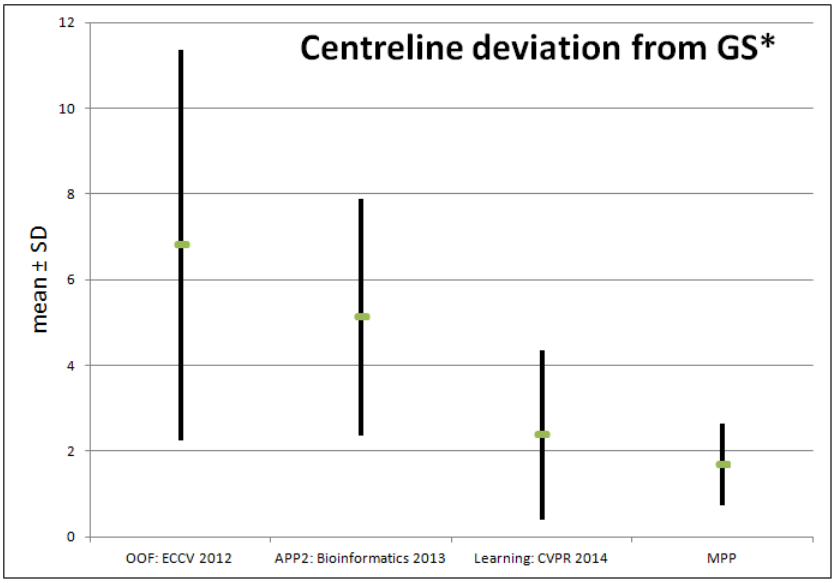

Figure 3-8: *Comparison with existing algorithms: euclidean deviation measured in pixels. *GS: Gold Standard.*

3.6 Discussion

To conclude, in this chapter we present a MPP model for unsupervised network extraction that is fully automatic and requires neither seed points nor manual intervention. The proposed method significantly improves network detection by reconstructing blurred and fuzzy segments of networks due to connectivity priors of the energy function. The stochastic optimization to the global minimum and the random nature of data exploration makes it preferable for large, high content microscopy data-sets. The obtained results demonstrate its reliability and robustness for fully automated analysis of neuronal morphology from 3D data stacks acquired by various imaging modalities.

Our work can also be viewed as a stochastic optimization of scale-orientation space for matched filters, developing a connected network of maximum vessel-

ness points on tubular structures. Such tubular/ vessel-like structures are abundantly encountered in medical images. Hence, our proposed model has potential for a wide range of application with adequate adaptation of data term modeling radiometric features and the desired priors. Our model is independent of data dimensionality and can be suitably adapted for 2D data. In fact, the biggest concern for MCMC methods applied directly to 3D data volume is the processing time. While MCMC algorithms are notorious for the time taken for convergence; we employ a MBAD sampling dynamics which greatly reduces computational complexity and speeds up convergence. There has been significant improvement in increasing stability and speed of convergence. Our experiments on profiling computation time showed that CPU time is mainly taken in extraction of radiometric features, particularly when it involves a stack of slices. Efficient handling of 3D data is an open and challenging problem. But with increasing availability of multi-core, multi-processor systems and advancement of GPU computing, efficient handling of 3D image data has various possible solutions. Some marked point process family of methods achieved huge speed up benefits with data driven parallelization and using GPU [10, 121].

We enumerate, below, the aims of the following chapters:

1. The model is parameter driven. Hence, studies of the sensitivity and robustness of our model w.r.t. the model parameters and automatic estimation of the critical parameters are important, as that would increase the general applicability of the family of Marked Point Process based methods.

2. Identification of critical nodes such as bifurcation and terminals of the

neurite tree. This will allow to calculate various properties of neurons such as branching order, average branch length, average branching angles, branch tapering rate etc which parameterize a neuron. These help in quantification of cell types in neuron shape space. In other words these it facilitates classification/enumeration of neuron cell type.

3. So far, we only extract the neuronal structures by a configuration of uniformly spaced MPP objects. It does not result in a structural representation of tubular objects. A digital reconstruction capturing the connectivity relation of the nodal hierarchy of the extracted network presents an analytical model abstracting out the key information from the vast (and sparse) 3D image volume. In the following chapters, we address the problem of neuronal reconstruction, where the extracted centreline, local width and orientation information along with detected critical nodes will aid in a connected, minimum spanning tree representation of the neuronal arbors.

Chapter 4

Modeling Single Neurons as Minimum Spanning Trees

Contents

Extraction and meaningful interpretation of neuronal morphology is a difficult task. These inherently 3D structures are difficult to capture faithfully as digital data. The resolution limit of microscopy technique and the slicing thickness of samples introduce a 2D projection effect occluding important nodal positions and connections, and misappropriating branch length. Imaging artefacts, such as structured noise, lighting gradation, cluttered backgrounds, and uneven staining of neuronal fibres give it a discontinuous, beaded appearance. These artefacts impose further challenges for automatic analysis.

The scope of this work is limited to extraction of single neurons and its branching patterns. The case of multiple intertwined neurons presenting ambiguous crossover and bifurcations are resolved currently by applying varied arbitrary heuristics or resorting to manual post-editing, even by the most sophisticated automated reconstruction algorithms [122]. We believe, this issue is better tackled at the image acquisition step, by differently labeling each neuron, as is successfully done by the Brainbow techniques [67].

We propose an efficient, stochastic framework for unsupervised neuronal network extraction in the previous chapter. It requires minimum parameterization and no user interaction or seed points. In this chapter, we introduce new priors designed to reflect typical arborization patterns in single neuron data. This enables accurate identification of branch bifurcation and terminals and gives us uniformly spaced intermediate nodes anchored to lengths of neuronal fibres.

4.1 Introduction

Parameter estimation in multi-parameter models is a recurring theme in biomedical image analysis. Bayesian inference methods are frequently employed in medical image computing for calculating posterior probability in the analysis of an inverse problem. Markov Chain Monte Carlo (MCMC) is a computational intensive technique often employed for Bayesian inference. They allow prior knowledge to guide the analysis of image data. For example, the expected size, distribution and density and organization of cells in an image can be modeled through various parameters as priors for more robust image analysis. Such priors improve the stability of the Markov Chain simulation reducing chances of consistent false-positives. Hence design of priors and the parameter initialization is of paramount importance in a Bayesian inference framework.

In this work, we examine the parameters of a stochastic marked point process framework for unsupervised, automatic reconstruction of single neurons. Firstly, we classify the model parameters and conduct a sensitivity and robustness analysis. This study identifies the critical parameters and their dependencies and relate their initialization to the application data. Thirdly, we propose new priors modeling arborization patterns encountered in neurons for efficient detection of bifurcation junctions, terminal nodes and intermediate points on neurite branches. These specialized priors also enforce constraints for preserving the connectedness of the neuronal tree components in spite of imperfect labeling causing intensity inhomogeneity and discontinuities in branches. This schema enables us to perform neurite tracing on 3D light microscopy images of Olfactory Projection Fibre axons from the DIADEM data set with good scores.

We complete the presentation of our model with an analysis of the errors and their sources in the neurite tracing pipeline.

4.2 Parameters of the model

Although there are significant benefits offered by this unsupervised and automatic framework including theoretical guarantees of global optimum, their usage is restricted by the difficulty in parameter initialization. In this chapter, we focus on the problem of automatic initialization of the parameters of a family of marked point processes. These object processes constitute a natural extension of Markov Random Fields (MRF), designed to better handle parametric objects. They have been conceptualized for efficient and competitive tackling of counting and object extraction tasks in high resolution data, typically in remote sensing and medical image analysis problems.

In the literature, parameters of MPP based methods are mostly initialized by various heuristic schemes, calibrated from domain knowledge or learnt empirically. In fact, many studies have been carried out to come up with automatic parameter estimation strategies. In [33, 24, 25, 20] the authors explore various methods such as stochastic expectation maximization, composite likelihood estimator, non-linear least square estimator respectively, for automatic estimation of parameters. In [24], a method for estimating the inverse temperature $\frac{1}{\beta}$ of the annealing scheme and the parameter w_d weighting the data and prior energy terms is proposed in the case of a simple marked point process using discs. It is a generic scheme that requires adaptations to specific applications and energy

models. However, the critical parameters still require initialization close to the optimum. Otherwise, the simulation has no means of converging near the global optimum. A general framework for a fully automatic approach for parameter estimation is, nevertheless, an open and challenging problem. In the following section, a critical study of our model shows its sensitivity and robustness w.r.t. the parameters.

In regard to our model and the adapted energy function, the parameters can be grouped into the following three categories.

4.2.1 Parameters of objects

The descriptive marks of the chosen objects are often application and data specific. Generally, the resolution of the image data and the available domain knowledge about expected size of the objects help in fixing the range from which these parameters can be sampled. Depending on available evidence of distribution of size of objects a uniform or gaussian sampling can be carried out from the ascertained range. For example, in case of Olfactory Projection fibres the branch widths are mostly uniform in data sets $6, 7$ and 8; whereas, the in data sets $1, 4$ and 5; exhibit a wide variance in branch width. Accordingly the radius range can be sampled with Gaussian model or uniform model respectively.

4.2.2 Parameters of energy model

The parameters of the energy functions, called "hyperparameters", in the literature, are calibrated according to the model and the application data. In our energy function, the data energy response involves adaptive thresholding for

discriminating "good" and "bad" objects. It frees the user from the burden of finding an optimal threshold. A good balance between the data term $U_d(\gamma)$ and the prior terms $U_p(\gamma)$, however, is of paramount importance in the energy function $U(\gamma) = w_d U_d(\gamma) + U_p(\gamma)$. In practice, carefully estimating the relative weight w_d between the data term and the priors ensures that we do not have to independently deal with the prior parameters. Moreover, it frees the user of the burden of independently learning the favoring and penalizing potentials of the priors. Learning w_d, however, is challenging, as it depends on many factors (imaging modality, quality of data, properties of the neuron etc.) Further, w_d should adapt to local sections of the images, rather than be a global parameter. Due to variations in density of labelled neurons, varying depth of the image stack, and noise in the XY plane, even learning w_d locally is difficult. This motivates us to improve our priors to obtain uniformly good results in all sections of the data.

The remaining energy priors involve favoring and penalizing potentials U_- and U_+, and potentials favoring particular sub configurations E_1, E_2, respectively. Balancing the energy function reduces to estimating of only one parameter w_d. w_d is proportional to difference of expected number of objects and as derived from radiometric properties and needs to be learned for every modality of image acquisition. It depends on modality of imaging, quality of the data, the nature (density, tortuosity) of the neurons etc. In our experiments it is observed w_d affects the position of the objects only in a small range if data energy and prior energy are relatively balanced, making it non-critical. Refer Figure 4-1, for how varying w_d values change optimal MPP configurations locally. The bi-

furcation node is marked green, terminals blue and intermediate nodes in red. However, when much greater priority is given to either, it affects the number of objects.

The attempts at empirical learning showed us that estimating w_d is a very difficult task. Firstly, it depends on many factors, such as imaging modality, quality of data, density of the labeled neuron etc. Secondly, w_d should best not be set as a global parameter and gives better result when it is adapted locally in the image. We observed, the optimal values of w_d gave good results in some sections of the data and failed in other sections having more densely labeled neurons. But due to numerous sources of variation such as density of labeled neurons, and variable noise levels at different depths of the image stack; it was difficult to find a schema for learning the optimal locally adaptive w_d. Hence, we took a more critical look at our priors and propose improvements in order to get uniformly good results in all sections of the images.

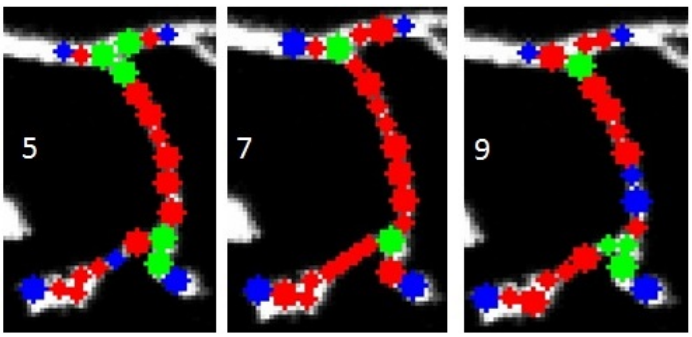

Figure 4-1: *Various MPP configurations with varying w_d values.*

4.2.3 Parameters of simulation

The most critical parameters of the model are the parameters controlling the simulation dynamics. The sensitivity of the model to these parameters are very noticeable. Unless the birth intensity is initialized optimally, there is little possibility of reaching close to the global optimum. It is generally set as an over estimation of the expected number of objects. Let $f(I)$ be the number of objects expected from the radiometric term. This can be approximated from the number of voxels (P) in the foreground intensity range by binary clustering algorithms. Using mean r from $[r_{min}, r_{max}]$ and assuming uniform distribution of objects — $f(I) = \frac{P}{\frac{4\pi r^3}{3}}$. Then, in each iteration a fraction $z = z_0\delta$ (generally, z_0 the Poisson mean is set $\frac{1}{3}$ to $\frac{1}{5}$) of the birth intensity is added to the evolving configuration.

Inverse temperature β and its rate of increase $\Delta\beta$ controls the cooling process. It is set heuristically in the literature of Simulated Annealing. Depending on the expected total number of objects, it is initialized low enough to give the process enough time for all objects to be detected. Thus, it is proportional to the difference $|\delta - f(I)|$. It is initialized according to the difference of expected number of objects and the estimation from radiometry.

The advantage of the adopted MBD dynamics is that the birth of objects is independent of temperature, allowing new objects to be added to the evolving configuration, even when the system is cool. Only in the death step, there is rejection based on temperature, discretization step and the energy. Thus, β is not critical and is heuristically initialized such that the system has enough time to cool down slowly, allowing sufficient iterations for the evolution of the configuration. The birth intensity δ_0 and its rate of discretization $\Delta\delta$ parameters

Object Parameters	$[r_{min}, r_{max}]^*$ OPF [1,10] CCF [1,25]	calibrated from domain knowledge and imaging resolution information
Energy Parameters	$U = 5; E_1 = 2$ $d_r = r_1 + r_2; d_r < d_a$	Empirically learnt; depends on image modality, quality etc.
Simulation Parameters	δ^*, $\Delta\delta = 0.999, \beta = 1,$ $\Delta\beta = 0.998$	δ and $\Delta\delta$ is critical for no. of objects in optimal configuration. The condition for convergence is $\Delta\beta < \Delta\delta < 1$

Table 4.1: Classification of model parameters. * indicates the data sensitive parameters.

mainly regulate the number of objects in the final configuration. The rate of cooling that determines the discretization step of the birth intensity has a strong influence on the quality of optimal configuration achieved. For convergence the desired condition is $\Delta\beta < \Delta\delta < 1$ [32].

4.3 Energy model with new priors

Our aim is to abstract out the neuronal morphology from the microscopy data into a mathematical model to facilitate further analysis. We sample special configurations of objects fitted to the points of maximum medialness measure on the image volume. In the following section we describe the role each of the energy components for neurite tracing in detail.

4.3.1 Fit to data

Our data energy response is based on the tubularity filter proposed in [98]. The medialness measure $M(\omega_i)$ is obtained by taking an integral of the image gradient at a scale σ_G proportional to the object radii along the circumference of the cut of the spherical object on the normal plane by a rotating phasor $V_\theta = cos(\theta)V_1 + sin(\theta)V_2$:

$$M(\omega_i) = |\frac{\pi}{2}\int_{\theta=0}^{2\pi} \nabla I^{(\sigma_G)}(x_i + r_i V_\theta) d\theta|. \tag{4.1}$$

An adaptive thresholding of the medialness response on the gradient response at the tube's center $M_c(\omega_i) = |\nabla I^{(\sigma_H)}(x_i)|$ enables to discriminate between "good" and "bad" objects. The data energy term is then defined as follows:

$$U_d(\omega_i) = \begin{cases} -(M(\omega_i) - M_c(\omega_i)), \text{if} M(\omega_i) > M_c(\omega_i) \\ 0, \text{otherwise.} \end{cases} \tag{4.2}$$

4.3.2 Connectedness

A pair-wise interaction potential for objects in each other's zone of influence imposes continuity constraints on the configuration of objects modeling neuronal fibres. It favors objects in poorly stained, fragmented sections. U_+ is a repulsive potential to penalize overlapping of objects, and U_- is an attractive potential to favor objects in touching distances of each other. Figure 4-2 demonstrates this effect. Every object is surrounded by a zone of repulsion where birth of other objects are penalized. This can prevent clustering and overlapping of objects.

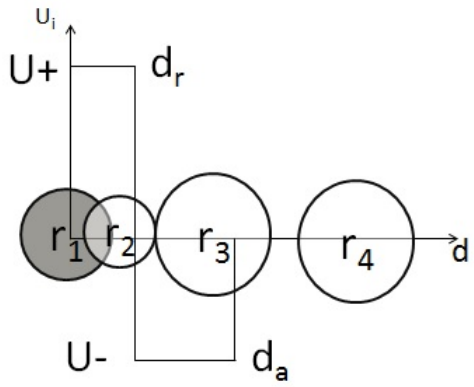

Figure 4-2: *Illustration of connection prior*

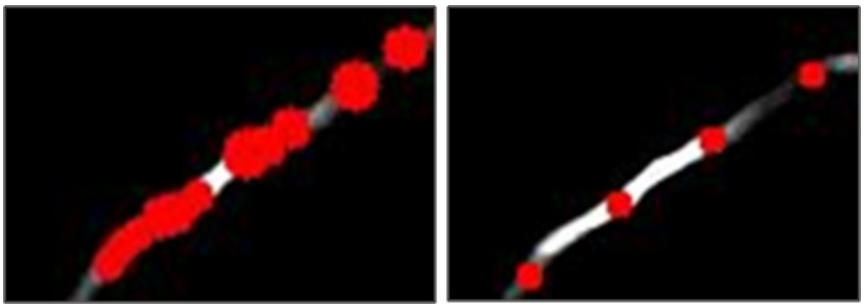

Figure 4-3: *Effect of connection prior on real data.*

Beyond the zone of repulsion is another concentric zone of attraction where birth of objects are favoured to preserve continuity of structures. In this illustration, w.r.t current object (shaded) with radius r_1; object r_2 is in the repulsion zone, object r_3 is in zone of attraction, where as object r_4 ia not influenced by object r_1.

$$U_i(\omega_i, \omega_j) = \begin{cases} U, \text{ if } d < d_r \\ -U, \text{ if } d_r \leq d \leq d_a \\ 0, \text{ if } d > d_a. \end{cases} \tag{4.3}$$

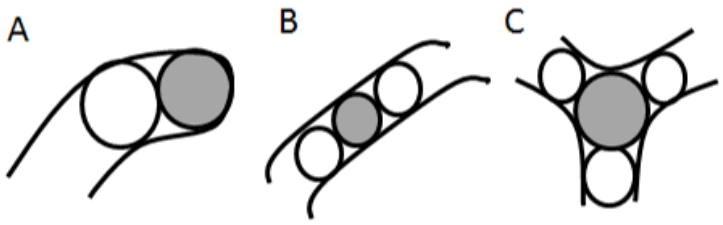

Figure 4-4: *Typical sub configurations encountered in axonal structures.*

Here, d is the Euclidean distance between the centers of the spheres; d_r and d_a ($d_r < d_a$) are respectively the repulsive and attractive distances, d_r, d_a are multiples of $r_i + r_j$. By varying d_r and d_a, density of spheres along the neuronal branches can be controlled. Refer Figure 4-3 to see the effect of connection prior on the MPP configurations. We see unevenly spaced configuration on the left image, considering radiometric properties only. On the right image, we see object at uniform distance considering interaction constraints with radiometric properties. Moreover, in weakly stained sections when the data term response is not favorable for an object, this term still ensures survival of the object in the configuration to ensure continuity of branches.

4.3.3 Spatial configurations

The second prior is a multi-object interaction potential, incorporating constraints on the local sub-configurations depending on — $k(\omega_i) = |\omega_j \in \gamma : d_r < d(\omega_i, \omega_j) <$

$d_a|$ — number of immediate neighbors of an object. Figure 4-4 highlights the sub configurations that are encountered in axonal structures. Each sub configuration is identified by its characteristic connection energy - evaluated w.r.t. the number of neighbors with direct data connection with the current object— shaded in the image— A: terminal, B: anchor points along the length of a branch, and C: bifurcation junction. Careful consideration of the prior proposed in Equation 3.13, and the single neuron structures in the Olfactory Projection Fibre data set, we redesigned the spatial configuration prior to favor bifurcations and terminals. Firstly, we realize, the condition of favoring $k(\omega_i) = 2$ is taken care of by the connectivity prior as discussed. Secondly, we favor both terminal and branching points to the same extent, i.e., with the same negative potential. In the axons, presenting a near perfect strictly one sided binary tree hierarchy, both these special configurations have equal opportunity for occurrence in the data. We propose the improved prior as follows:

$$U_c(\omega_i) = \begin{cases} \infty, \text{ if } k(\omega_i) = 0 \\ -E_1, \text{ if } k(\omega_i) = 1,3 \\ \infty, \text{ if } k(\omega_i) > 3. \end{cases} \tag{4.4}$$

The association of favorable negative energy potentials E_1 with particular local sub-configurations encourage survival of sub-configurations corresponding to critical nodes such as bifurcations and terminals. At the same time, it discourages isolated objects in the configuration, which are likely to correspond to cell nuclei or other such background structures. Our analysis of the gold standard reconstruction indicates there are no multi-furcations in the data considered.

So, in this way unusual local sub-configurations can be weeded out from the candidate global configurations. Using such local sub-configurations we can generate further descriptors for the extracted neurons like average branch curvature, branching order, length etc besides identifying bifurcations, terminals and points of high inflection along branches.

4.4 Sampling and estimation

The main idea of the proposed approach is to sample special configurations consisting of spherical objects and fit them to the microscopy data stacks to voxels of maximum neuriteness measures. These configurations are projected onto the image volume. The configurations are optimized by measuring the similarity between the projected model of the configuration and the neuronal data. A Gibbs energy is defined on the configuration space. The optimum global energy is defined over the space of union of all possible configurations, considering an unknown a-priori number of objects. Exhaustive search of the solution space is impractical. We choose an efficient Multiple Birth and Death (MBAD) dynamics [32] to find the Maximum A Posteriori (MAP) estimation (Eq.3.4), greatly reducing computational cost and speeding up convergence. We optimize the object configuration in an iterative scheme, where multiple random objects are proposed and removed independently and simultaneously in each iteration depending on the relative energy change due to their introduction. We sample from the probability distribution μ_β using a Markov chain of the discrete-time MBD dynamics defined on Ω and apply a Simulated Annealing scheme. At every iteration, a transition is considered from current configuration γ to $\gamma' \cup \gamma''$ where

$\gamma^{'} \subset \gamma$ and $\gamma^{''}$ is any new configuration. The corresponding transition probability is given by:

$$P(\gamma \rightarrow \gamma^{'} \cup \gamma^{''}) \sim (z\delta)^{|\gamma^{''}|} \prod_{\omega_i \in \gamma \setminus \gamma^{'}} \frac{\alpha_\beta(\omega_i, \gamma)\delta}{1 + \alpha_\beta(\omega_i, \gamma)\delta} \prod_{\omega_i \in \gamma^{'}} \frac{1}{1 + \alpha_\beta(\omega_i, \gamma)\delta}, \tag{4.5}$$

where $\alpha_\beta(\omega_i, \gamma) = \exp(-\beta(U(\gamma \setminus \omega_i) - U(\gamma)))$. The convergence properties of the Markov Chain to the global minimum under a decreasing scheme of parameters δ and $\frac{1}{\beta}$ are proved in [32]. The probability of death of an object depends on both the temperature and its relative energy in the sub-configuration; whereas, birth of object is independent of both energy and temperature and is spatially homogeneous. In this way, the iterative process finds a configuration $\hat{\gamma}$ minimizing the global energy Eq. 3.5.

4.5 Experiments

We evaluate our proposed model by application to axonal trees descriptions from the DIADEM Olfactory Projections Fibres data set acquired by 2-channel confocal microscopy [21] . While Markov Chain Monte Carlo methods are notorious for their slow convergence, the novel MBD sampling strategy enables our MATLAB implementation to converge under 5 mins on a machine with Intel Core i7 processor, 3.4 GHz with 8GB RAM. Note, we run our experiments with the data term pre-computed. It is observed with live computation of data term for the same initialization the time taken is roughly 45 mins -1 hr to converge for these data sets due to the way the 3D volume of images slices is handled in MATLAB. The simulation parameters are fixed - inverse temperature $\beta = 1$, time

Figure 4-5: *MPP configuration modeling OP1.*

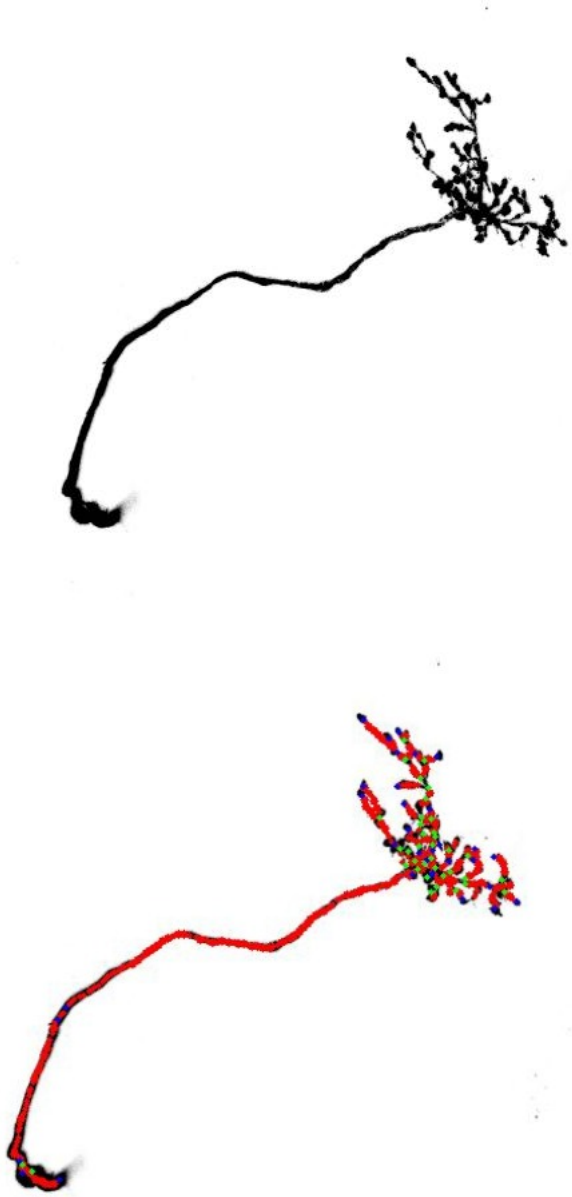

Figure 4-6: *MPP configuration modeling OP4.*

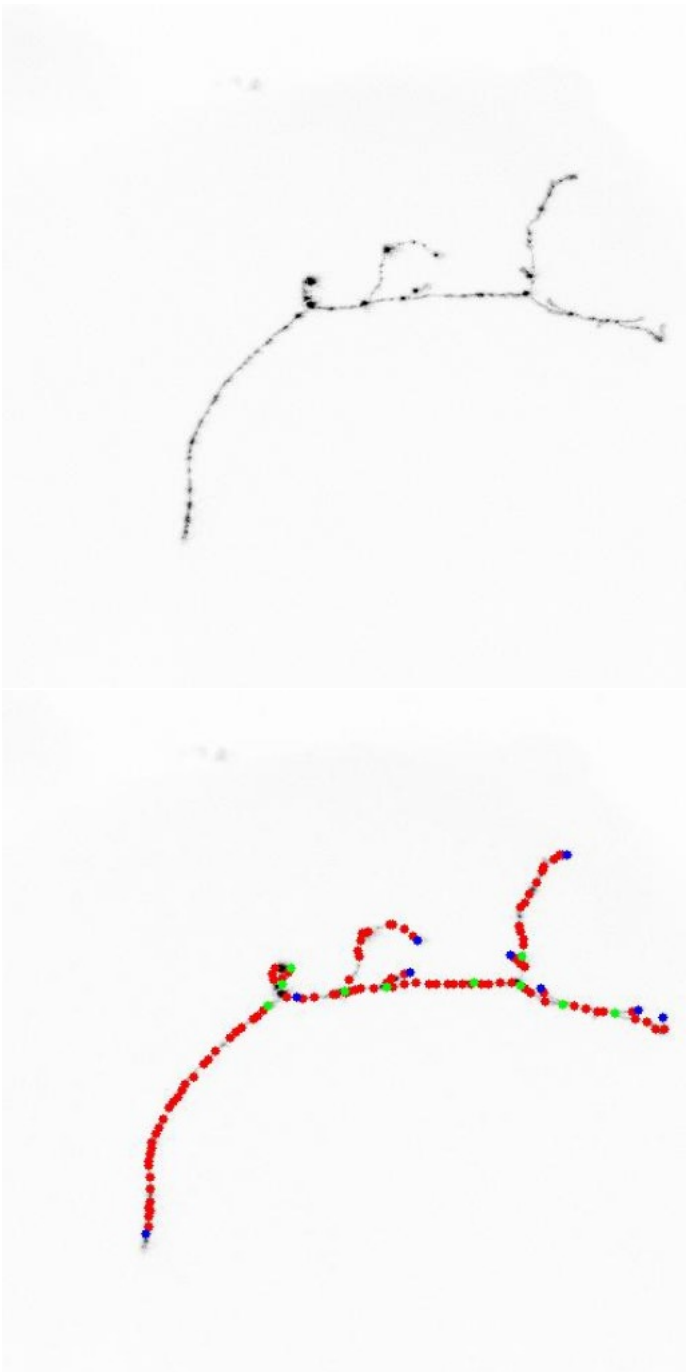

Figure 4-7: *MPP configuration modeling OP5.*

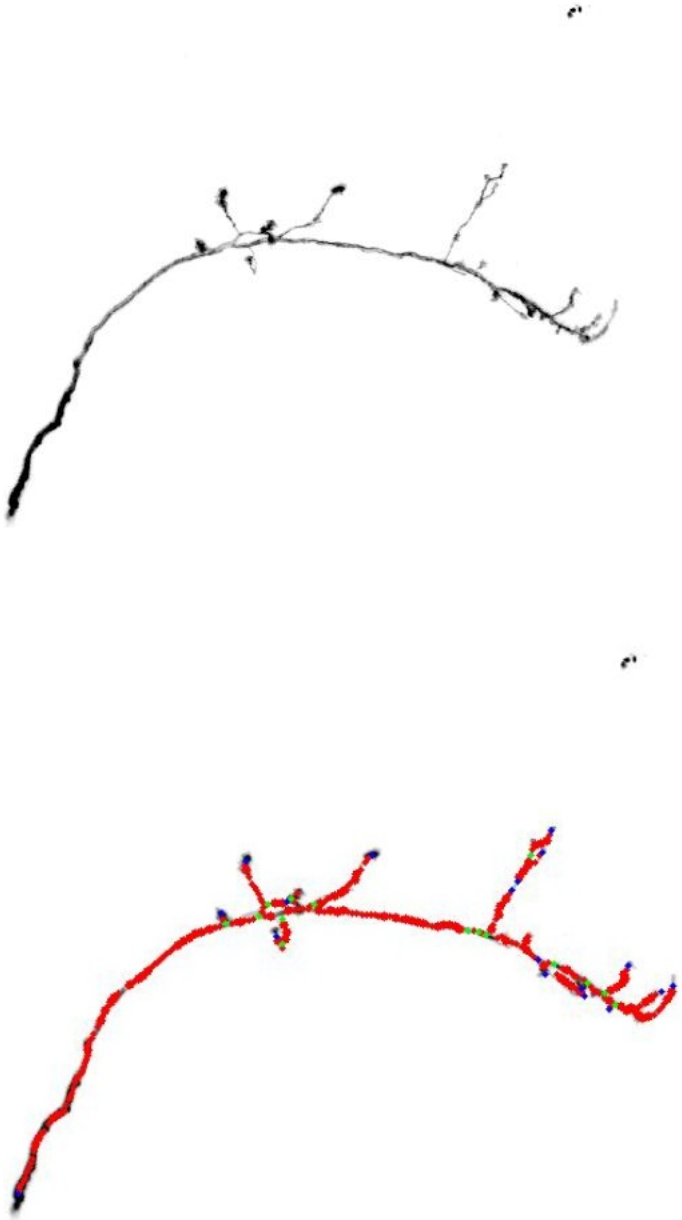

Figure 4-8: *MPP configuration modeling OP6.*

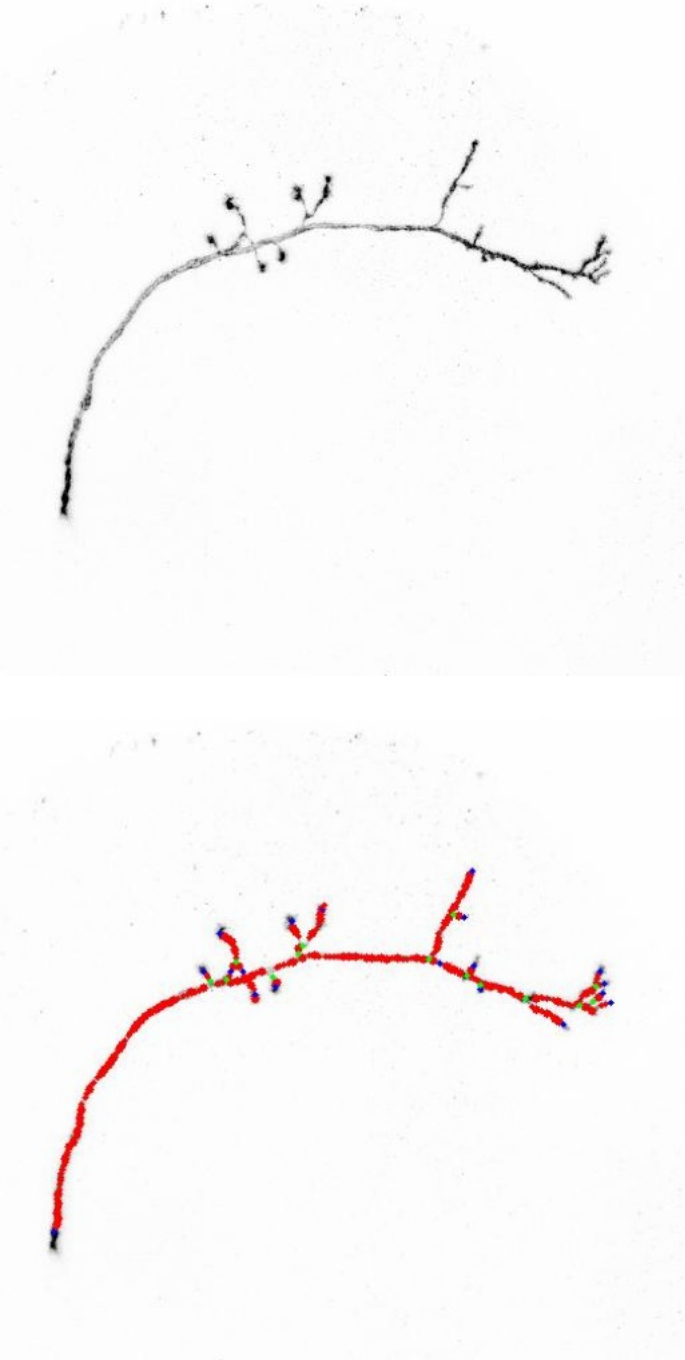

Figure 4-9: *MPP configuration modeling OP7.*

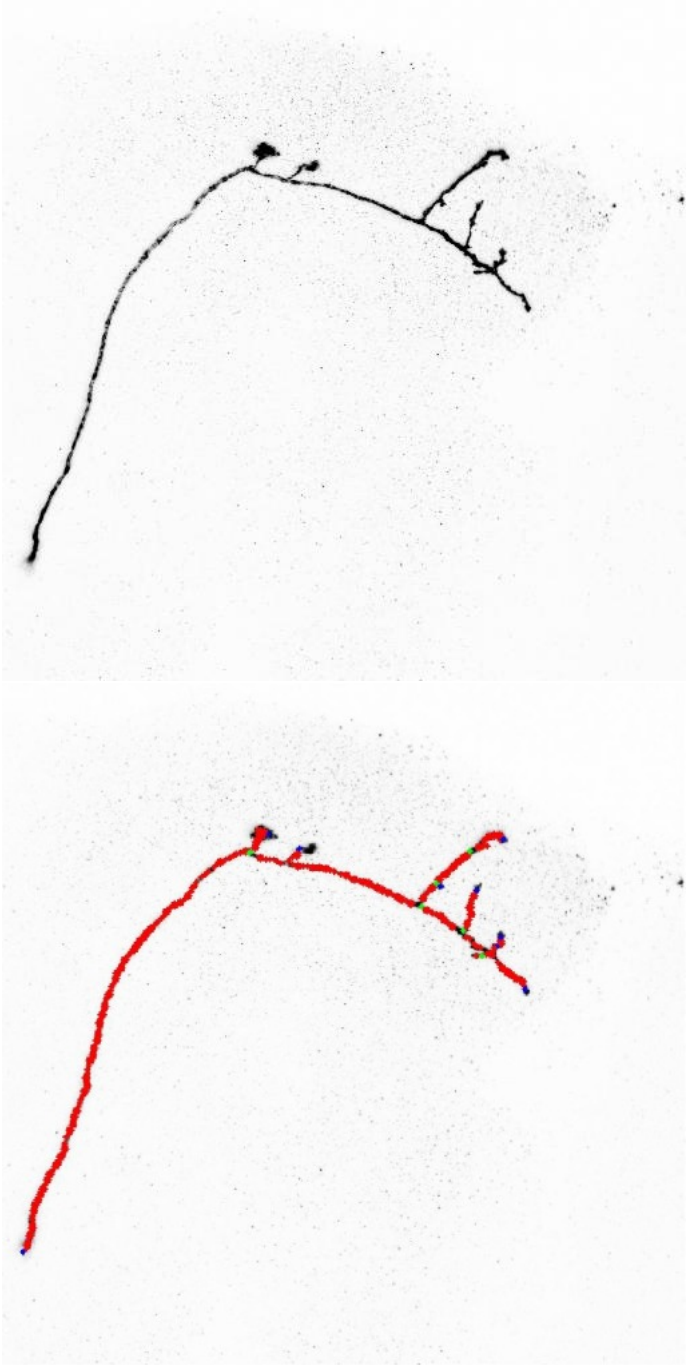

Figure 4-10: *MPP configuration modeling OP8.*

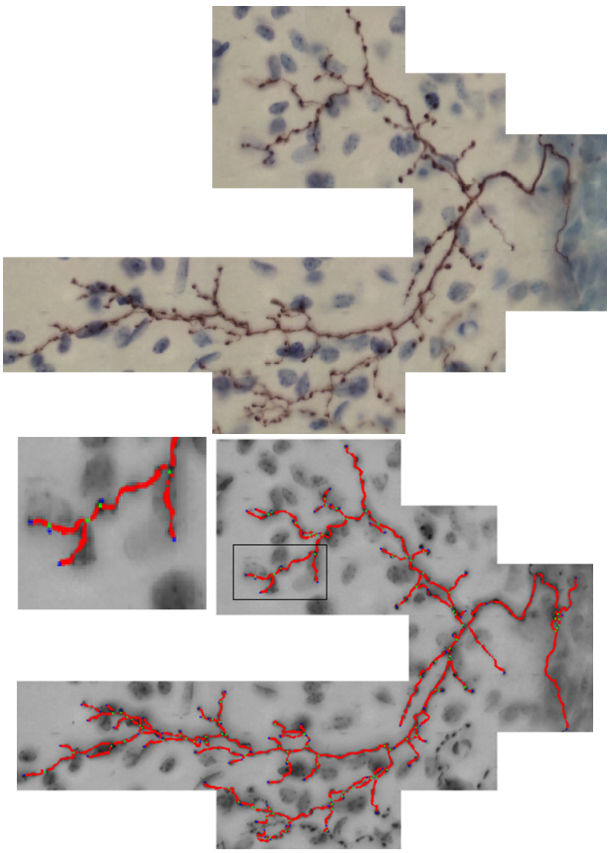

Figure 4-11: *MPP configuration modeling CCF1.*

discretization step size $\Delta\delta = 0.997$ and inverse temperature update $\Delta\beta = \frac{1}{0.999}$ is used for all our experiments. The δ_0 for each dataset and the final number of objects in the optimal configuration are listed in Table. 4.2. Refer Figures 4-5 to 4-11 for the modeling of single neurons morphology with optimal MPP configurations. For every data set the top panel shows the maximum intensity projection of Olfactory Projection Fibre axon, in inverted grayscale for ease of visualization and the bottom image shows the MPP configuration fitted to the neuronal data on projection of the stacks. The green nodes represent bifurcation, blue nodes terminals and the intermediate nodes on branches are red. Note that due to the projection effect some of the nodes appear mis-located. Generally, higher rates of mis-detection occurs in densely branches sections. Some close lying bifurcation nodes, detected as trifurcations by the model, were duly resolved as multiple bifurcations.

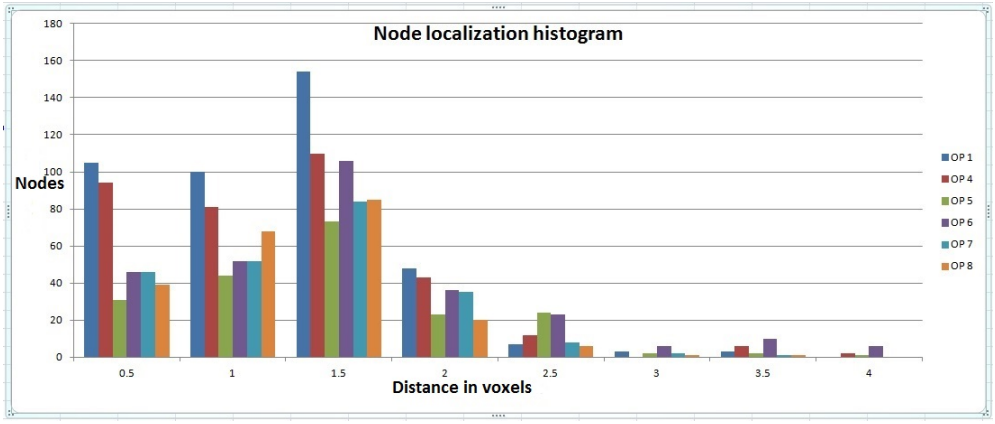

Figure 4-12: *Histogram shows Euclidean distance between points sets* $\{P\}$ *and* $\{G\}$.

We score the performance of our reconstruction method with the DIADEM metric [41] and the newly proposed NetMets metric [77, 78]. The DIADEM

metric gives a combined F-score for the positions and connections of the reconstructed neuron by comparing against a manual gold standard reconstruction. The DIADEM metric penalizes topological errors closer to the root more than errors further down the tree hierarchy. It ignores short branches of less than 6 pixel length in the scoring. Due to various inconsistencies, instead of using this metric, the community has proposed favoring visual inspection of results. But for the sake and ease of comparing our results against existing methods, we evaluate the performance of our algorithm with the DIADEM metric as well. Overall average score obtained by our method is 0.837 ± 0.043. The NetMets software, on the other hand, gives a more detailed analysis for the quantification and visualization of errors in two biological networks. False negative(FN) and false positive(FP) rates for geometry and connections constitute the metrics for comparing explicit representations of interconnected biological networks. Finally, we also compare the deviation of our extracted centreline against the gold standard. In Figure 4-12, the histogram shows Euclidean distance of the extracted points set $\{P\}$ using our proposed model from gold standard manually delineated centerlines $\{G\}$.

Our inspection of the accompanying gold standard reconstructions with the DIADEM data revealed some of the datasets such as OP5 and OP8, the gold

	OP1	OP4	OP5	OP6	OP7	OP8
δ_0	2150	1850	1000	1350	1100	1100
No. of objects in final configuration	435	358	204	283	226	223
DIADEM Score	0.829	0.789	0.797	0.830	0.921	0.854

Table 4.2: Summary of reconstruction

standard contains only a part of the entire structure. We observed better performance on data sets such as OP1 (1496 points) and OP4 (1383 points) in spite of them showing more complex structure due to denser reconstructed by the experts compared to other data sets OP5 (135 points) and OP8 (152 points). Thus for OP5 and OP8 data sets, we used the Simple Neurite Tracer [71] to complete reconstructions in a semi-automatic supervised manner. We used the image analysis tool Fiji [105] with built-in tools for analysis and hardware accelerated 3D visualization of the results. We used Neuromantic [89] for visualization of generated SWC files.

Generally, the more error prone regions of the data are the densely branched sections and the small branches making very acute angles with the main branch. The performance of our method is poorer in profusely branched sections towards the axon terminals (particularly OP4), evident from the low connectivity scores by the NetMets metric. Due to a lack of image data consideration in neighbor identification these regions prove to be tricky for our algorithm. The other error prone branches are ones oriented near perpendicular to the imaging plane (along our "Z" axis). Whenever branches oriented near perpendicular to the imaging

	gFN	gFP	cFN	cFP
OP1	0.028	0.041	0.304	0.313
OP4	0.026	0.052	0.671	0.716
OP5	0.025	0.038	0.176	0.6
OP6	0.052	0.052	0.384	0.416
OP7	0.020	0.037	0.258	0.148
OP8	0.138	0.142	0.328	0.454

Table 4.3: NetMets scores for MPP

plane are present, there is a stark fore-shortening effect of their length leading to misinterpretation. The primary source of such an error is the slicing thickness at the image acquisition stage. Such errors introduced during the image acquisition stage keeps accumulating and culminates in large topological distortion in the final stages. There is generally a lot of noise in the top slices, which is typical of confocal microscopy data. It is better eliminated again in preprocessing stages, ideally by imaging the volume from both end and compositing them together to get a relatively noise free data.

Our analysis reveals huge anomaly in the number of terminal nodes reported by various existing methods on the same data sets in the literature. In Figure 4-13, we can visualize the source of these variations. Some of branch terminals appear as blobs. Our MPP algorithm interprets it correctly by modeling it with a sphere of bigger dimension. But the Neurolucida semi-automated tool treats them as bifurcation point with very short branches, drastically increasing the number of terminals nodes. Similarly in sections of high curvature of the branch, it has also been misinterpreted as terminals. This highlights, once again, the subjective variability of expert manual or semi-automatic reconstruction and proves how our MPP model presents a more accurate semantic interpretation of neuronal morphology.

4.6 Discussion

To conclude, in this chapter, we present a marked point process model with specialized priors for sophisticated semantic description of neurite morphol-

	SNT (SA)[71]	Neurolucida (SA)[45]	3Dtip (A)[68]	Vaa3D (A)[128]	MPP (A)
OP1	41	49	48	43	43
OP4	43	61	46	46	39
OP5	9	9	17	6	9
OP6	18	18	23	12	16

Table 4.4: Terminals reported on same data by different methods. SA: Semi-automatic; A: Automatic.

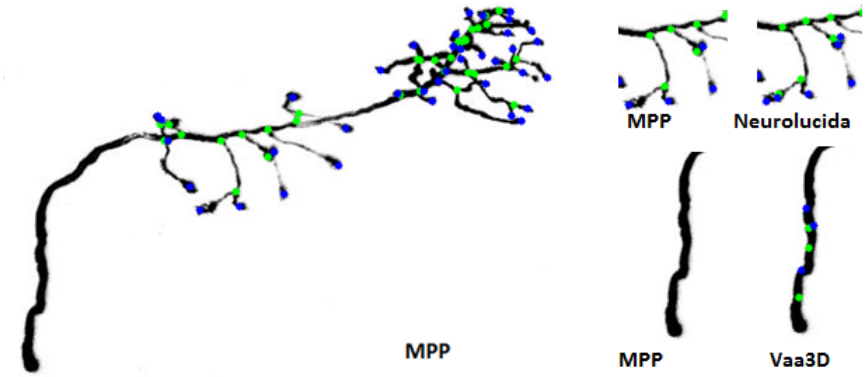

Figure 4-13: *Comparison with other methods. The position of detected terminals are marked in blue and the bifurcation in green.*

ogy. It gives accurate detection of bifurcation, terminals and intermediate nodes. This identification of critical nodes enables to derive several parametric descriptors for neuronal classes - such as average branch length, branch tapering rate, branching order; branching angles etc. Further the study of the model parameters reveals their data dependencies and helps to define a set of rules for automating the initialization of the parameters

Chapter 5

Reconstruction of Neuronal Tree Morphology

Contents

In this chapter, we focus on incorporation of an image potential in consideration of neighboring node relation. Indeed, due to lack of it our algorithm

as described in previous chapter performs poorly at the junctions or densely branched zones. We develop a framework to use image data in determination of connectivity of neuronal branches and remove the false positives from the MPP nodes. In our previous chapters the notion of connection of nodes were based on the neighbor properties of the defined priors. However, the neighborhood criteria is based solely on Euclidean distance between the centers of our MPP objects, with no incorporation of the image data.

Neuronal reconstruction refers to extracting a mathematical or analytical description of the neuronal morphology that can facilitate further analysis. Modeling the hierarchy of neuronal branches is a difficult task. Firstly, the resolution limit of microscopy technique and the slicing thickness of samples introduces a 2D projection effect resulting in occlusion of important nodal positions and connections. Uneven staining with biological markers gives beaded appearance to neurite branches. While branch cross-sections are commonly expected to exhibit Gaussian intensity profiles, often membranes take up strong contrast and the inverted Gaussian profile gets misinterpreted as parallel running branches. Imaging artifacts, such as structured noise, lighting gradation or cluttered backgrounds, impose further challenges for automatic analysis.

5.1 Introduction

We obtain an extraction of the neuron data by the fully automatic marked point process and stochastic optimization framework described in the previous chapters. We fit configurations of spherical objects to high neuriteness voxels in

the data volume. This representation identifies the terminal and bifurcation nodes, and anchor nodes along the branches. While it provides sort of a semi-segmentation of the neurite that allows the trained expert eye to extrapolate the continuity; it does not guarantee physical connectivity, particularly in weakly labeled sections of a neuron. We choose a subset of these points to re-initialize our front at optimal intervals during the fast marching. We sub-sample the object configuration to select a set of nodes $n_i = [x_i, y_i, z_i] \in N$ *iff*: n_i is a terminal node, bifurcation node or high curvature node along the length of a branch. Our consideration of an image potential in determination of nodal connections removes the false positives from our initial set of node while generating a connected minimal spanning tree representation. In this way, we propose a method for abstracting the neuronal morphology from the microscopy data and presenting a digital reconstruction of it in the standard SWC format, prevalent for storage, sharing and analysis in the neuroimaging community.

Related works

Tubular structure such as neurites, vasculature networks, bronchial airways are abundantly encountered in biomedical imaging. Inferring connectedness of vessels is a commonly studied problem in biomedical imaging. Some examples are angiographic studies of coronary arteries, vasculature networks in different organs, retinal images. Generally, the vascular network or neurons are injected/labelled with some biological dyes to show strong contrast with the background or neighboring organs and structures during imaging to aid in tracing. Traditionally, multi-scale Eigen-analysis [36], in combination with gradi-

ent information [56] or intensity ridge traversal [11] are used to detect seeds on tubule centerlines. These filters find voxels maximizing a vesselness measure by collecting responses over a range of filter scales. However, they have limited ability in describing the connectedness, tree hierarchy and branching pattern of complex neuronal arborization. Hence, shortest graph path based neurite tracing methods are employed for the purpose of generating their *Minimum Spanning Tree* (MST) models. They connect paths of maximum neuriteness voxels locally between sets of seed points to extract the global neurite structure [115, 27, 122, 97]. In the following section, we analyze the major classes of neuronal reconstruction algorithms.

A. Firstly, parametric deformable models such as the *Active Contours* methodology is very popular for connecting seed points locally on neurite branches [27],[122]. The snakes deform under the influence of internal data driven energy and external regularization forces to assume the arbor contour on energy minimization. The intrinsic shortcoming of snake based methods is their sensitivity to initialization and background noise, in addition to being computationally expensive. Active contours require very precise initialization to avoid being trapped by local energy minimum. Extensive preprocessing is required for selection of candidate voxels for the initialization of snakes and dynamic reparameterized is necessary to accurately recover the object centreline. The second limitation is its inability to deal with topological adaptation such as splitting or merging branch parts.

B. A second class of local explorative methods — the *Iterative Model Fitting* — fit a mathematical neurite-like kernel, between sets of detected seed points

[136]. These methods are computationally efficient since it performs a localized search by matching templates at different orientations at the end of already detected segments. But the high cross-sectional morphology variability does not allow for such shape averaging. The neuronal fibres are approximate tubules often of irregular cross-section depending on "XY" and "Z" data acquisition resolution. Moreover, such cylinder or tubule like templates perform poorly at junctions or bifurcations.

C. In contrast to the local explorative methods, the global methods are mainly based on *skeletonisation* or *medial axis* representation of a segmented neurite image [14, 88]. A good segmentation of the data is difficult to achieve due to artifacts introduced during imaging, structured noise and the non-uniform staining of neuronal fibres. Subsequent pruning of the skeletal tree is necessary to remove loops and spurs that add loops and false length to the neurites. Often, heuristic post processing, requiring manual intervention, are necessary to join disconnected components. Moreover, the memory requirements of global methods are, generally, exceptionally high making them unattractive choices for large data sets (and limiting them to 2D data only [14]). Automated neuronal reconstruction is still an open and challenging problem is evident from the many recent review literature on the topic - [79, 34, 107].

In this work, we propose a fully automatic framework, requiring no user interaction to generate a meaningful and precise description of the neuronal arbors. For this purpose, first, we adopt a gradient vector field based speed map, taking into account the anisotropy of the voxels in the image stack, to guide front propagation. Second, we choose the parameter-free fast marching methods to

extract the neuronal fibres as geodesic curves. We use a set of optimal control points to re-initialize the front at frequent intervals. Finally, to answer the key issues of analysis of neuronal fibres our method captures the inherent graph structure of the minimal paths and order them into a minimum spanning tree hierarchy. The underlying numerical principles make it fast, memory efficient and robust.

5.2 Proposed method

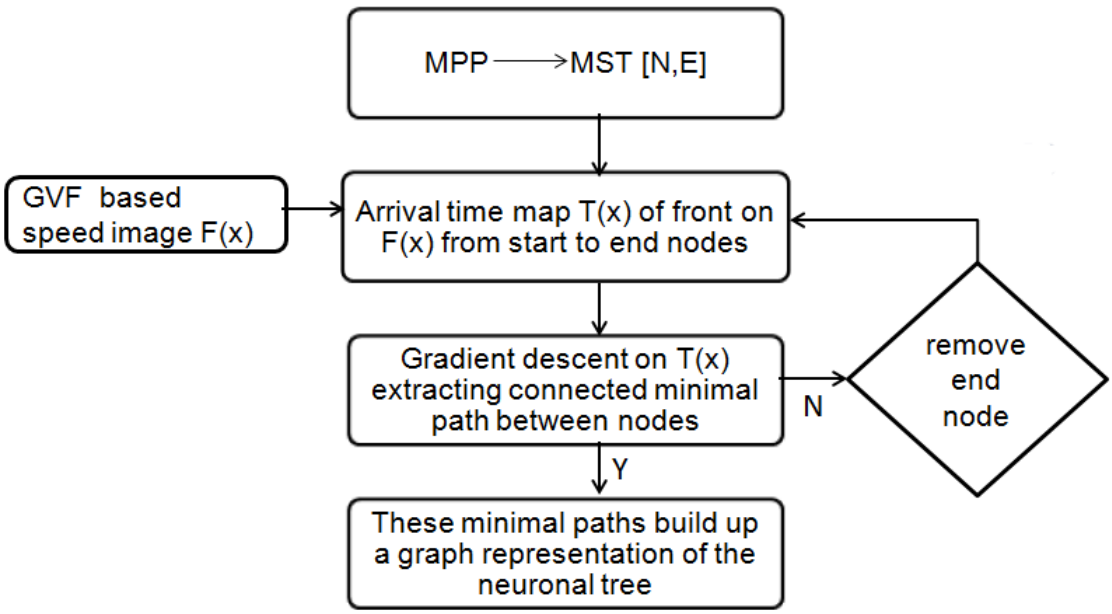

Figure 5-1: *The flow chart for the reconstruction pipeline.*

Our aim is to capture the positional and connectivity information of neuronal morphology into an analytic model. Refer Figure 5-2 and Figure 5-1 for an overview of the reconstruction pipeline. The automatically generated seed

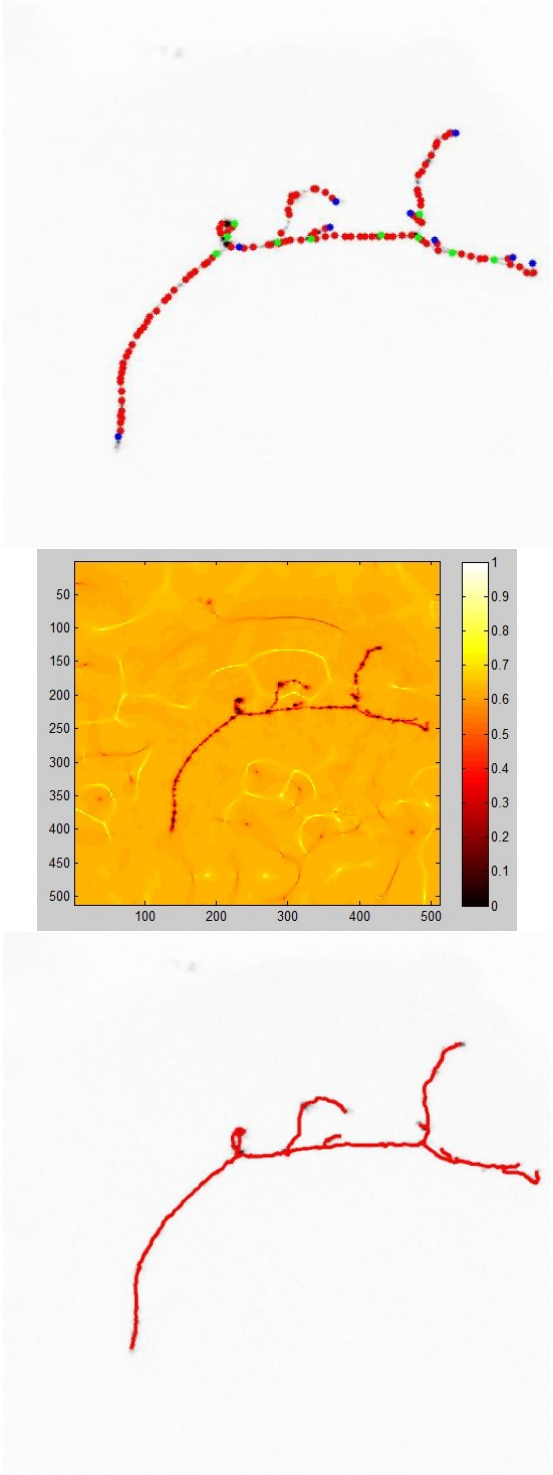

Figure 5-2: *The algorithmic steps in the reconstruction pipeline.*

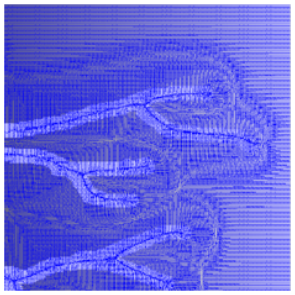

Figure 5-3: A. Gradient vector field

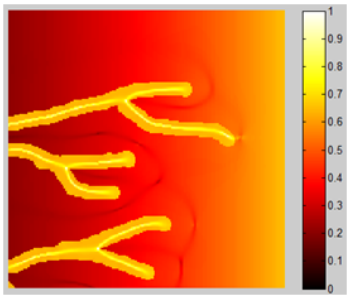

Figure 5-4: B. Speed image

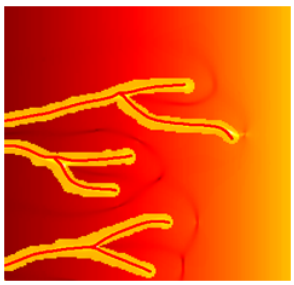

Figure 5-5: C. Centreline in red

points by Marked Point Process model with green nodes showing bifurcation, blue as terminals, red nodes as anchors and points of high curvature along the branches. These nodes are used to frequently re-initialize the marching front. The middle image shows the Gradient Vector Field (GVF) based speed image its color map. The bottom image shows the resulting tree on maximum intensity projection of Olfactory Projection Fibre data set 5. The neuron tree reconstruction by fast marching models the branches by the geodesic curves representing the medial axes of their topologies. Our algorithm goes through the following steps-

1. We begin with a set of automatically generated nodes as our control points to re-initialize the front for the reconstruction of neural tree. The selection of nodes includes terminal nodes (in blue), the bifurcation junctions (in green) and the anchor points (in red) along the branches that show maximum non-linearity w.r.t. its immediate neighbors, i.e., the high curvature voxels.

2. An adjacency matrix defines connections between nodes with edge weights as euclidean distances. We perform a topological sort of the selected subset of nodes into a tree-like hierarchy using Kruskal's algorithm [57]. We now aim to

perform a depth first traversal of the obtained tree, starting from the root, as provided with each data set, to generate the directed MST of the voxels representing the centreline of the neuronal structure.

3. We compute a Gradient Vector Field (GVF) of the original data volume to generate a speed map. This map facilitates the implementation of Front Propagation.

4. From a start node we allow the front to propagate until it reaches the end node. A gradient descent on the arrival time map of the front connecting the start and end nodes extracts the geodesic curve between them in the form of the medial axis of the branch shape. For the erroneous nodes in our node list, the due to the image potential based speed map, the minimal path fails to connect the 2 nodes. This enables us to remove the false positives nodes and obtain a reduced node set for our spanning tree.

5. We re-initialize our front and perform Step 4 iteratively until all nodes (control points) are visited. Thus, we obtain a tree-like description of the neuronal data by modeling the branches and segments by their centerlines in the form of a Djikstra's minimal graph path representation.

In this way, we generate a fully connected minimum spanning tree from of the noisy unstructured microscopy data containing the neurite. This digitized representation of both morphology and connectivity information of neuronal data can facilitate further analysis. In the following sections, we explain in further detail the individual steps involved.

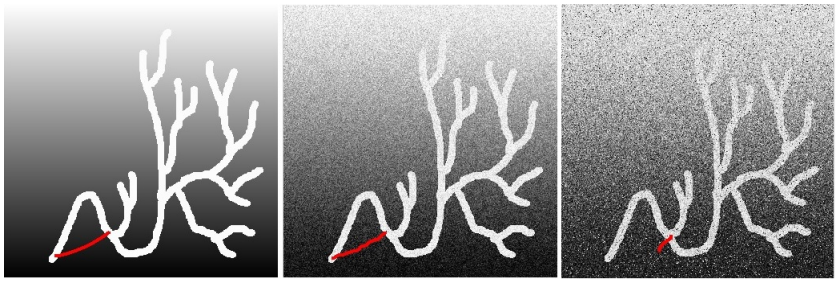

Figure 5-6: *Attempted minimal paths between root and first branch point in absence of intermediate control points.*

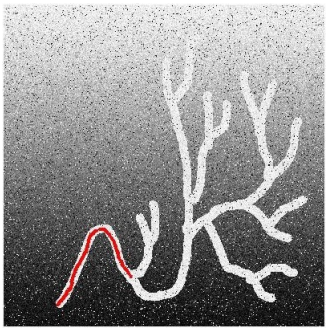

Figure 5-7: *Minimal path with intermediate control points to reinitialize the front.*

5.2.1 Control points

Refer Figures 5-6 and 5-7, for reconstruction attempts in absence and presence, respectively, of MPP nodes as control points. Figure 5-6 shows attempts at finding minimal paths between root and first branch point in absence of intermediate control points to reinitialize the front. The synthetic example is a challenging one due to the gradience in the background and the high curvature of the branches, besides the increasing levels of noise. Figure 5-7 shows minimal path between root and first branch point with intermediate control points to reinitialize the front. These control points optimally localize computation on

our structure of interest, preventing the minimal paths from leaking out of the structure due to background gradience or cutting corners at high curvature regions. It is observed, in presence of cellular structures or structured noise in the vicinity of the branches, or illumination gradation in the background, the front tends to spill out of our structure of interest into the background. Often, these artifacts become sources of errors by getting connected as part of network during digital reconstruction falsely increasing neural length. Conversely, minimal path representations cut corners at high curvature regions of branches shortening actual neuronal length. Hence, these control points re-initialize the propagating front at frequent intervals to optimally localize the computation and control the quality of the reconstruction. We sub-sample the MPP object configuration to select a set of nodes $n_i = [x_i, y_i, z_i] \in N$ *iff*: n_i is a terminal node, bifurcation node or high curvature node along the length of a branch.

In this work, firstly we propose a scheme to find a reduced set of nodes to define our tree by removing some false nodes from the detected neuron morphology. A spanning tree of a graph is a subgraph containing all the vertices and no cycles. Secondly, we utilise this framework to verify the edges between the neuronal nodes given by the MPP objects in the image data by modeling them as geodesic minimal paths. We iteratively build up a minimal spanning tree by adding the neuron branches as edges.

5.2.2 Speed map computation

The second step is computation of a speed map for the subsequent Front Propagation (FP) phase. Our speed map is calculated by diffusion of a Gradient Vector

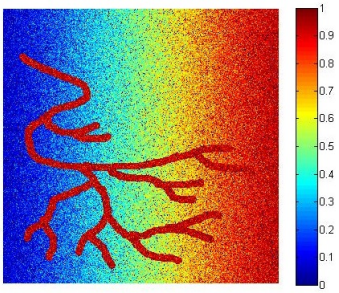

Figure 5-8: *The speed image of synthetic data (SYN01).*

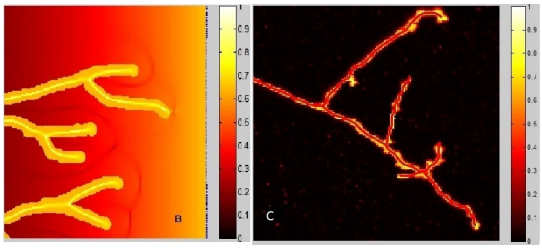

Figure 5-9: *Extracted centerlines overlayed in red on speed image.*

Field (GVF). It was proposed by Xu. *et al* in [130] to enable edge-preserving diffusion of gradient information. The GVF exhibits some characteristic properties that felicitates detection of topological centerlines or medial axes. It is noted that the magnitude of the gradient vector decreases inwards away from the boundary and vanishes at the center. For given image volume I, and an initial vector field $F = |\nabla I^{\sigma_G}|$, where σ_G is the scale of the gaussian, the GVF is defined as the vector field $V(\mathbf{x})$ that minimizes the energy:

$$E_{gvf}(\mathbf{x}) = \int\int\int_{\mathbb{V}^3} \mu|\nabla V(\mathbf{x})|^2 + |F(\mathbf{x})|^2|V(\mathbf{x}) - F(\mathbf{x})|^2. \qquad (5.1)$$

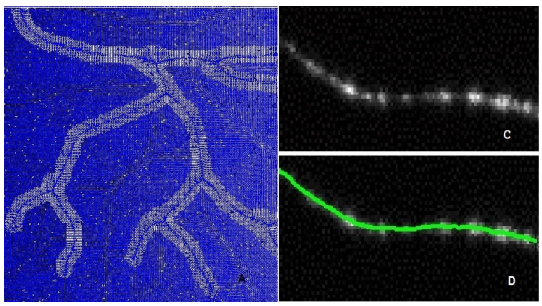

Figure 5-10: *Gradient vector field and connected minimal paths.*

Here, voxel vector $\mathbf{x} = (x, y, z) \in \mathbb{V}^3$, the image domain, and μ is a parameter for balancing between the two terms dependent on noise level in data. The intuition behind this variational formulation is to achieve a slow varying, smooth result in homogeneous, no-data regions; while, in the regions of interest, it maintains the strengths of the original edge map. In practice, it makes the GVF robust at determination of medial axis for even arbitrary shapes and weak structures.

In Figure 5-8, we see the speed image of the synthetic data and color map for its interpretation. Due to strong background gradation, we can see propagation speed is high at the right corner, which would cause the propagating front to spill out of the structure in absence of terminal nodes to stop them. Figure 5-9 shows the speed image of real data and color map for its interpretation. Propagation speed is highest along the centerlines of the branches. The extracted centerlines are overlayed in red on speed image. Figure 5-10 shows a visualization of the Gradient Vector Field showing convergence of vectors at centreline of neuronal branches. On the right side in Figure 5-10, we see in spite of beaded appearance of neuronal branches (top), a connected minimal path is approximated (in green,

bottom).

In our implementation we adopt the diffusion based GVF (dGVF) function in MATLAB. In case of our 3D image stack with differential in-plane and "Z" axis resolution, the isotropic GVF fails to produce a robust speed image. dGVF can handle the problem associated with poor convergence of gradient vector flow in 3D volumes, by adjusting the time-step based on voxel dimensions. dGVF generates differential diffusion speeds in tangential and normal directions according the local structures of the image, taking into account the anisotropy of the voxel dimension. This modification is a key factor in improving the speed image to locate the centerlines of the neuronal fibres.

In order to exploit both magnitude and directional information of the obtained GVF, we calculate the average outward flux for every voxel. The numerical computation is made robust by employing the divergence theorem [118]. The divergence at a point is defined as the net outward flux per unit volume, as the volume about the point shrinks to zero. Via the divergence theorem, we get:

$$D(\mathbf{x}) = \frac{1}{N_i} \int \int \int_{\mathbb{V}^3} V(x_i).\hat{n}_i dS_i, \tag{5.2}$$

where N_i is a 26-neighbor of $\mathbf{x}_i$ and $\hat{n}_i$ is the unit outward normal at $\mathbf{x}_i$ of the unit sphere S_i in 3D, centered at $\mathbf{x}_i$.

Fast Marching Methods are designed for problems in which the speed function never changes sign, so that the front is always moving either forward or backward. This allows to convert the problem to a stationary formulation, which combined with numerical tricks, gives it tremendous speed. Hence, we perform

a re-scaling of the divergence function as explained in [83] and normalize the speed image $F(\mathbf{x})$ to bring it in range $[0,1]$:

$$F(\mathbf{x}) = exp(\gamma[1 - D(\mathbf{x})].*I(\mathbf{x})) - 1, \tag{5.3}$$

where γ is a noise control parameter, set at 1.2 for our experiments. It is observed that further strengthening the speed image by multiplying with the original data $I(\mathbf{x})$ considerably speeds up the front.

5.2.3 Edges as geodesic minimal paths

Fast Marching Methods (FMM) were introduced to find numerical approximate solutions to the boundary value problems of the Eikonal equation [76]:

$$F(\mathbf{x})|\nabla T(\mathbf{x})| = 1. \tag{5.4}$$

Here $T(\mathbf{x})$ is an arrival time map that denotes the time taken by a front originating from $\mathbf{x}_s$ and propagating according to the speed map $F(\mathbf{x})$ to reach voxel $\mathbf{x}_f$. Next, a gradient descent using the 4th order Runge-Kutta time-step operator on the arrival time map $T(\mathbf{x})$ extracts the path corresponding to the shortest arrival time between the start node $n_s \leftarrow \mathbf{x}_s$ and end node $n_f \leftarrow \mathbf{x}_f$.

Beginning with the root node R and a list of unvisited nodes $n_1, n_2 \ldots \in N$, at every iteration, our algorithm extracts a part of the neuronal morphology by computing the geodesic curve of the branch topology. We allow the front to propagate guided by the speed image $F(\mathbf{x})$ until it reaches one of the nodes n_i from the node list N. From this node $n_f \leftarrow n_i$ to the point of initialization of

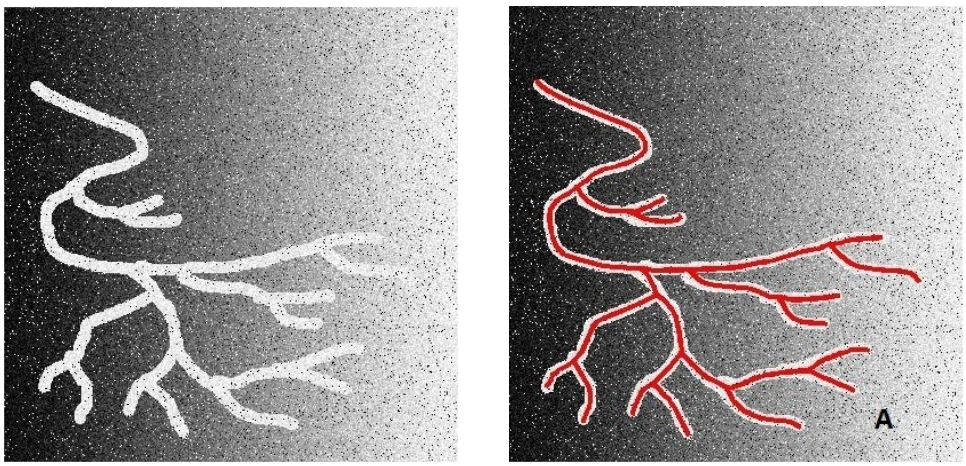

Figure 5-11: *Reconstruction of challenging synthetic data (SYN01).*

marching front n_s, a gradient descent is performed on the arrival time map to compute the geodesic path between the two. The resulting minimal path p is updated to the list of minimal paths $p_i \cup p$. Next, we update the just visited node as the start node $n_s \leftarrow n_i$, remove it from node list $N = N - n_i$ and re-initialize the front to extract the next part of the neuron tree. On reaching a terminal node, we trace back to the immediate past bifurcation and continue the iterative procedure. We terminate when node list N is empty. In this way, FMM captures accurate minimum spanning tree representation of neuronal morphology by iteratively adding minimal paths between nodes [28]. FFM offers several desirable features such as inherent connectivity and smoothness, which counteract noise and cross-section irregularities.

5.3 Experiments and results

We test the performance of our proposed model on synthetic data modeling actual challenges and 3D light microscopy image stacks from the DIADEM Challenge database [21]. The Synthetic data (SYN01) exhibits high curvature fibres presenting sharp corners and a strong gradience of the background, such as found in case of uneven illuminance during image acquisition. Refer Figure 5-11 for results. The sharp curvature of the branches and added noise make it a challenging task. It contains a single "axon-like" binary tree, corrupted with *Gaussian* and *salt and pepper noise*. The DIADEM Olfactory Projection Fibre data sets are axons acquired by 2-channel confocal microscopy.

	gFN	gFP	cFN	cFP
OP1	0.028	0.041	0.304	0.260
OP4	0.026	0.052	0.546	0.391
OP5	0.025	0.038	0.176	0.333
OP6	0.052	0.052	0.384	0.320
OP7	0.020	0.037	0.225	0.040
OP8	0.138	0.142	0.328	0.352
Overall	0.026±0.005	0.042±0.006	0.327±0.12	0.282±0.12

Table 5.1: NetMets scores for MPP+FFM

	OP1	OP4	OP5	OP6	OP7	OP8	overall
DIADEM Score	0.846	0.807	0.818	0.854	0.926	0.863	0.852±0.038

Table 5.2: DIADEM scores for MPP+FFM

Avg Manual Tracer	0.78±0.1[83]	-
Stepanyants *et. al*	0.80±0.1[27]	Semi-automatic
Roysam *et. al*	0.863[122]	Semi-automatic
Mukerjee *et. al*	0.82±0.07[83]	Automatic
Xiao *et. al*	0.77±0.17[128]	Automatic
MPP	**0.837±0.043**	Automatic
MPP+FFM	**0.852±0.038**	Automatic

Table 5.3: DIADEM scores comparison

5.3.1 Evaluation

Although the method of validation of traces itself a topic of much research with various metrics being employed [37, 42, 78], we choose to evaluate our automatic reconstruction using both DIADEM metric [42] and NetMets [78]. As explained previously, the DIADEM metric is particularly crafted for scoring Neuronal tree hierarchic reconstruction and is more relaxed in penalizing errors far from the root node. Whereas, NetMets is for more general graph comparison with more expressive scoring system.

In our experience with the various semi-automatic tools for neuronal morphometry analysis, the baseline inter-software variability limits the DIADEM metric score at 0.91. Indeed, this represents the inherent limitation of validation against gold standard manual reconstructions due to lack of a singular ground truth. Table. 5.3 presents the DIADEM metric scores of various reconstruction tools. The existing methods are mostly semi-automatic and incorporate user-interaction at some stage of reconstruction. The Open Snake method [122] and the method presented by Stepanyants *et. al* [27] were judged the two best methods in the DIADEM challenge. But there is significantly large variance with

the Open Snake method, 0.836 ± 0.35, due to incorporation of user interaction in the final stage for proof-editing and optimization of original automatic trace. Our MPP+FFM method performs better than existing fully automatic methods in the literature. We have presented a fully automatic framework for analytical modeling of 3D neuronal morphology. Our Marked Point Process neurite model and Fast Marching combination makes it fast, robust and accurate. Further to the DIADEM scores, using the NetMets scores of geometric (g) and connectivity (c) false positive rate (FPR) and false negative rate (FNR) *gFNR, gFPR, cFNR, cFPR* further helps us see how the incorporation of an image potential consideration in connectedness of nodes consideration removes some of the erroneous nodes of MPP neurite model and improves the overall reconstruction results.

Overall, our algorithm performs uniformly well over all the Olfactory Projection Fibre datasets modeling the exceptional challenging scenarios encountered during neuronal reconstruction. The most challenging data set for our algorithm is OP4, due to its dense and profuse branching at the terminal end and OP5, which besides the high SNR, presents significant branch cross-section distortion from the assumed circular shape. Refer to NetMets generated graphs (Figures 5-12 to 5-17) for visualization of missed nodes and errors of MPP and MPP+FFM reconstruction. The top image is the visualization of gold standard manual reconstruction. Red node indicates the missed branch. The middle visualization is the automatic reconstruction with our proposed marked point process. Red nodes indicate the erroneous region, sometimes highlighted with boxes. The bottom image shows reconstruction using fast marching and marked

point process, where we can see false positive nodes are removed. Finally, Figures 5-18 to 5-23 show the reconstruction by our proposed method (in red) and the manual gold standard reconstruction (in magenta) for reference.

5.4 Discussion

In this chapter, we propose a pipeline to integrate the detection, modeling and reconstruction tasks. Our method produces an automatic and reliable extraction of neuronal morphology. It is robust to small branch discontinuities, intensity variations due to inhomogeneous labeling, irregular cross-sections, noise and background gradience. In addition, it is good at faithfully following high curvature branches. Overall, it improves the accuracy of automated neuronal reconstruction and minimizes variability.

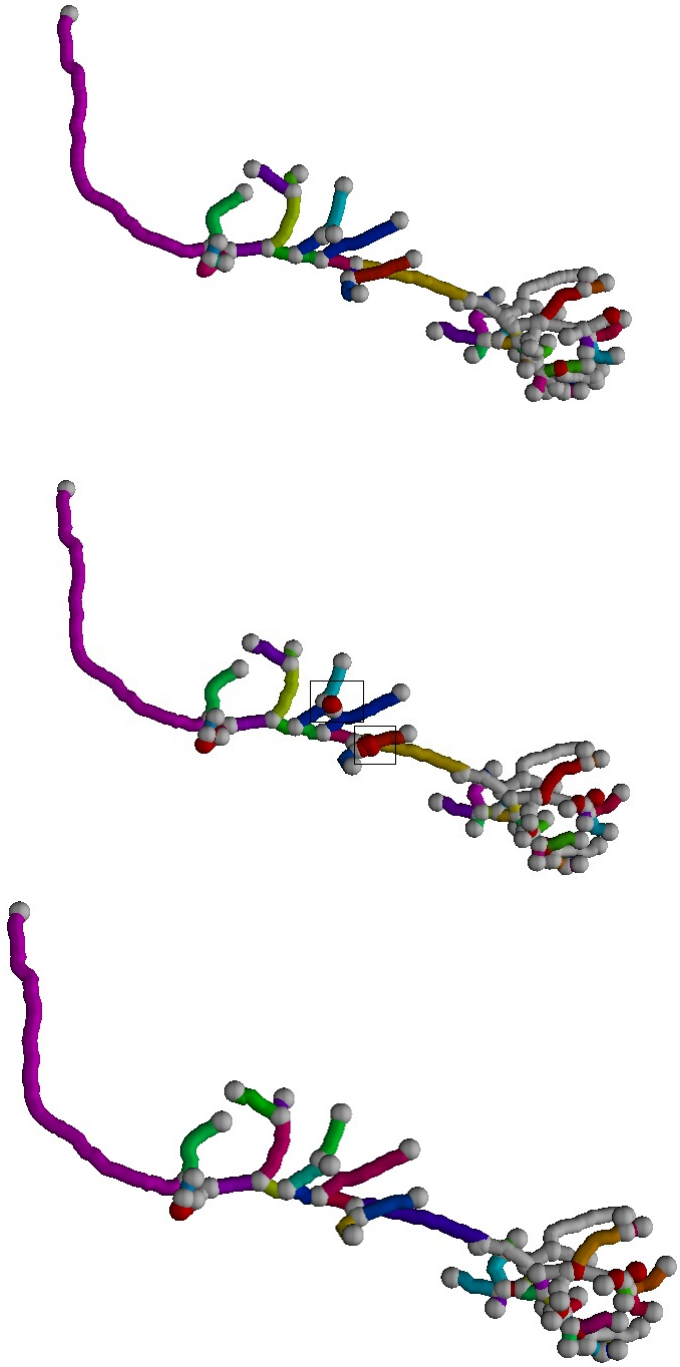

Figure 5-12: *NetMets visualization of our results with MPP and MPP+FFM against the manual gold standard reconstruction.*

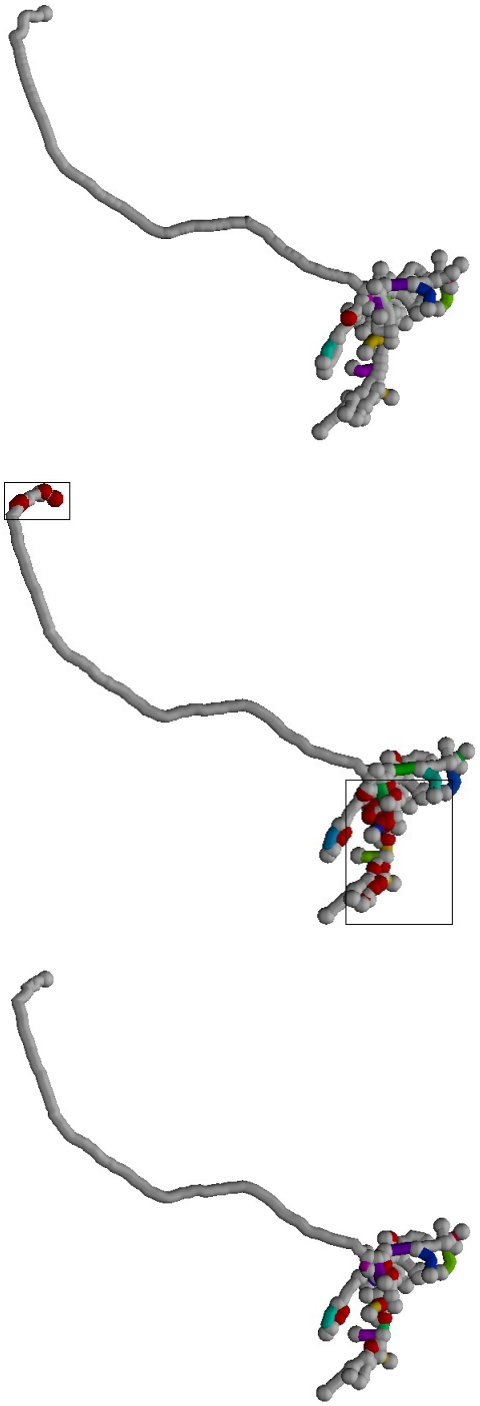

Figure 5-13: *OP4: NetMets visualization of our results with MPP and MPP+FFM against the manual gold standard reconstruction.*

Figure 5-14: *OP5: NetMets visualization of our results with MPP and MPP+FFM against the manual gold standard reconstruction.*

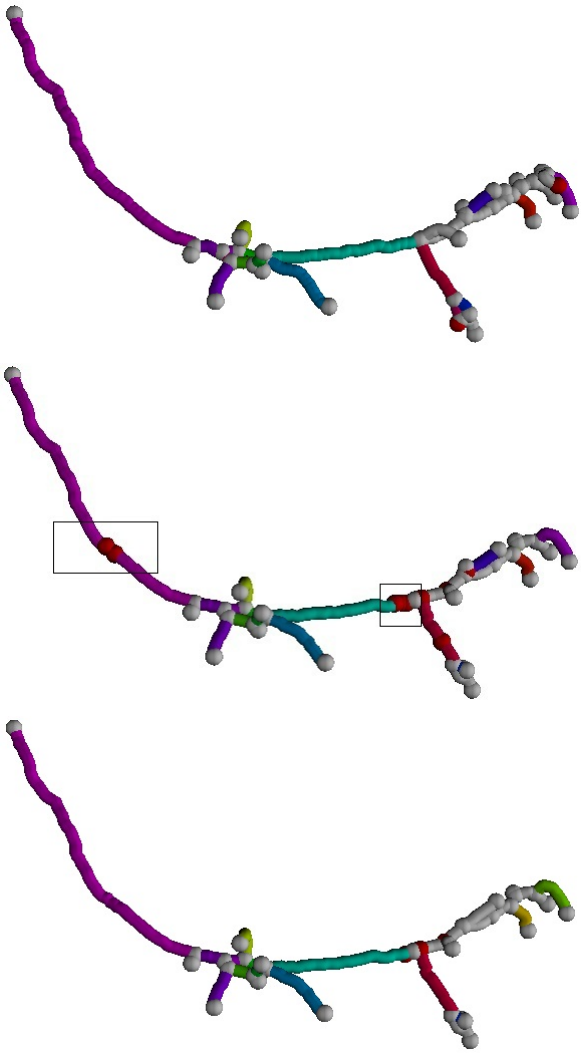

Figure 5-15: *OP6: NetMets visualization of our results with MPP and MPP+FFM against the manual gold standard reconstruction.*

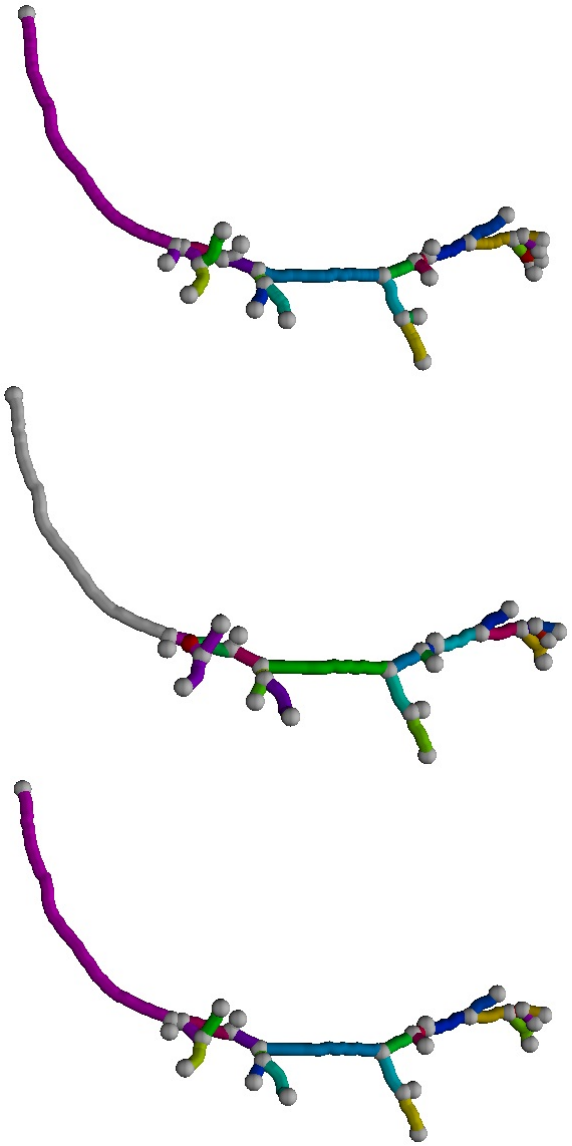

Figure 5-16: *OP7: NetMets visualization of our results with MPP and MPP+FFM against the manual gold standard reconstruction.*

Figure 5-17: *OP8: NetMets visualization of our results with MPP and MPP+FFM against the manual gold standard reconstruction.*

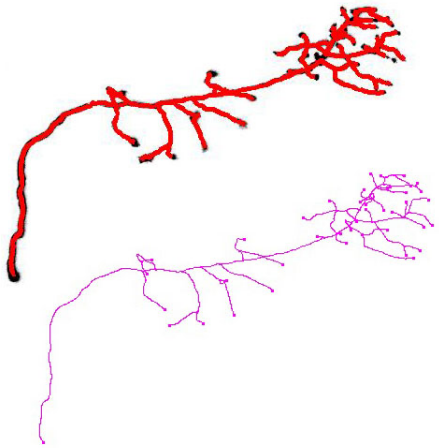

Figure 5-18: *OP1: The reconstruction by our proposed method (in red) and the manual Gold Standard reconstruction (in magenta) for reference.*

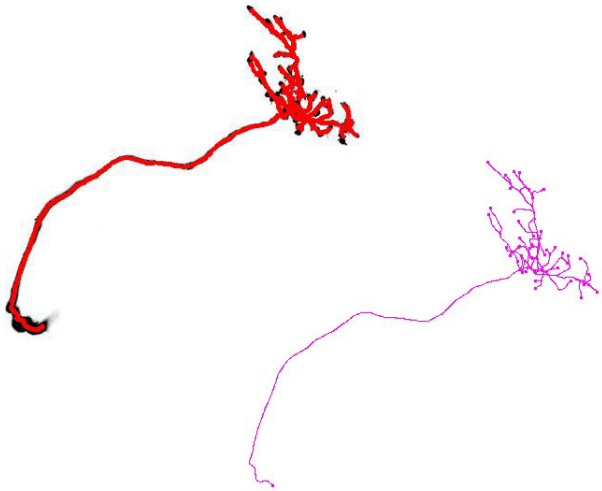

Figure 5-19: *OP4: The reconstruction by our proposed method (in red) and the manual gold standard reconstruction (in magenta) for reference.*

Figure 5-20: *OP5: The reconstruction by our proposed method (in red) and the manual Gold Standard reconstruction (in magenta) for reference.*

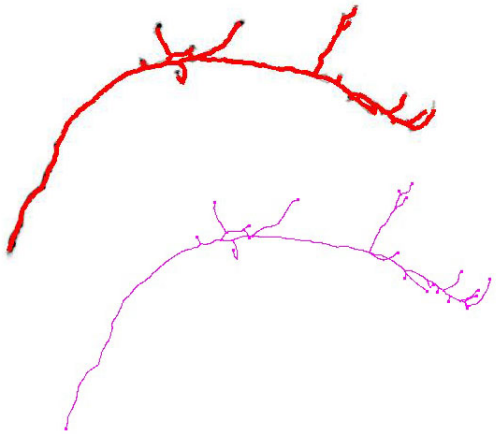

Figure 5-21: *OP6: The reconstruction by our proposed method (in red) and the manual Gold Standard reconstruction (in magenta) for reference.*

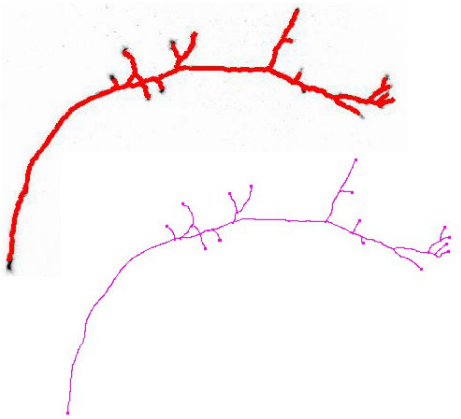

Figure 5-22: *OP7: The reconstruction by our proposed method (in red) and the manual Gold Standard reconstruction (in magenta) for reference.*

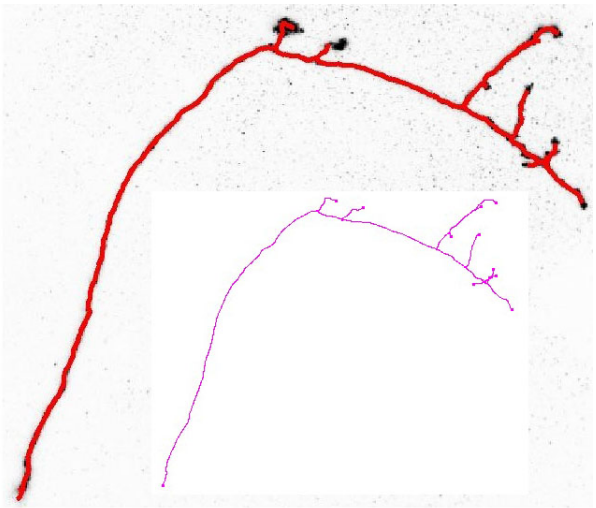

Figure 5-23: *OP8: The reconstruction by our proposed method (in red) and the manual Gold Standard reconstruction (in magenta) for reference.*

Chapter 6

Conclusion

Contents

The aims of this thesis are two-fold. Firstly, to exploit image processing and computer vision tools for automatic analysis of high content, high resolution 3D image stacks routinely generated by diverse microscopy methods. Secondly,

to quantify neuronal morphometry in standard *SWC* formats, favored by neurobiology community for concise description of neuro-image informatics. We broke the problem down into three methodological challenges — detection of neuron-like tubular structure networks, relating parameter initialization to application data; design of improved priors for description of tree-like single neuron topologies in biomedical structures and finally, digital reconstruction of neuronal morphology into connected minimum spanning tree representation. The following section concludes the thesis with a summary of our motivations, contributions and reiteration of the salient features of our works.

6.1 Summary

6.1.1 Detection of tubular structure networks

In Chapter 3, we present an object *detection* framework to extract connected networks of high medialness voxels representing the centerlines of tubular structure networks. Vessel or tubular structure detection in large biomedical images is a frequently encountered problem. Our proposed method combines the merits of both local (sub-configuration optimization through geometric shape and interaction priors) and global information (optimizing a global objective function). Our 3D marked point process model with varying object dimension simultaneously extracts position of centerline, local width and orientation. Besides, it enforces continuity in weakly labeled and noisy sections of the data by means of high level priors on object interactions. A segmentation of the structure can be further obtained by taking the envelope of these spheres as we move along

the branch centerlines.

6.1.2 Descriptive tree topologies for single neurons

In Chapter 4, we focus on *modeling* of single neuron morphology. We propose new priors emulating the arborization patterns exhibited in axonal and dendritic trees. We successfully classify critical nodes like bifurcations, terminals and anchoring nodes along neurite branches in images of single neuron data sets. To automate the process of parameter initialization, we classify the parameters of our model, relating parameter initialization in a meaningful way to the properties of application data. Based on our empirical learning we propose a set of rules for parameter estimation. Our investigations further identifies the critical parameters and leads to design of new priors that offer descriptive modeling of tree topologies. We can derive quantification of estimable parameters such as branching index, branching angles, internodal lengths, branch curvature etc.

6.1.3 Digital reconstruction of neuronal morphology

In Chapter 5, we propose an automatic pipeline for *reconstruction* of 3D neuron data. Numerical methods like fast forward marching provide fast and robust implementations that are scalable in complexity to 3D biomedical data. We abstract out important positional and connectivity information of neuronal topology from huge microscopy data volumes into graph theoretic SWC format that is readable by most neuronal analysis and visualization softwares. It offers concise analytical model for ease of storage, exchange, and archiving of data. The advantages offered by fast forward marching is the inherent connectedness of

minimal paths modeling the medial axis of neurite branches, which are further organized into a minimal spanning tree hierarchy. Our incorporation of a gradient vector field lifts any shape assumption on neurite branches and ensures accurate centreline detection in arbitrarily shaped topologies. The fast marching technique enables incorporation of an image potential in evaluation of connectedness of Euclidean neighbor nodes that help to rectify mis-location of critical nodes.

This concludes our work on designing an integrated detection, modeling, and reconstruction pipeline for neuronal trees from high content, high resolution image data. Our evaluation with multiple metrics show that the proposed algorithm out-performs the existing state-of-the-art reconstruction techniques and minimizes the inherent subjective variability of semi-manual methods, incorporating user-interaction at any stage.

6.2 Perspectives on future research directions

In the following section we discuss the open problems and new research directions on which our proposed framework has direct implications.

6.2.1 Enumerating neuron cell types

Study of shape-orientation space of neurons convey information about their molecular and functional identities. Systemic enumeration of neuronal cell types is important in comprehending the brain's abilities. Even today, the neuroanatomists have limited knowledge about diversity of neuron cell types. Sci-

entists catalogue/classify neuron populations according to their specific differentiated functions. The intricate structure-function co-relation of neurons, the structural and functional building blocks of the nervous system, has been conclusively proven. This implies that morphology analysis of neurons can predict hitherto unknown cell functions/categories [135]. It is a 2-step process — neuron tracing followed by its localization in the neuron shape manifold [110]. To analyze the parameter space (density, branch directionality, information that can be derived from our proposed model) of neuronal morphology to identify the discriminating factors for inter and intra class differences in the neuron cell types is still an open problem. This work would require close collaboration with cellular neuro-anatomists. Computational approaches to quantify neuronal morphogenesis in longitudinal studies are expected to establish patterns of neurodegeneration for disease diagnosis and prediction. Automated image analysis and quantitative neuro-informatics will assess the complex and dynamic nature of neuronal morphogenesis over time in response to various electro-chemical stimuli. Finally, this will identify the neuronal parameters for discrimination of healthy inter-neuron morphology variability and pathologic conditions.

6.2.2 Neuronal morphogenesis for connectomics

For connectomic studies, neuron to neuron interaction is very important. Multi-neuron scenarios present challenging, ambiguous cases of overlap of fibres from different sources (potential synapse sites) and branching of neuronal fibres. Recently, various heuristics have been proposed in the literature to deal with such ambiguities [37], but their success is limited to only sparsely labeled neurons.

The Neuromuscular Projection Fibers, for example, represent very peculiar challenges of parallel running, overlapping axons [73]. The Brainbow technique labels neuronal fibres from different source cells with differently expressed markers by genetic manipulation [67]. This enables in visually distinguishing the intertwining fibres. Computational techniques like *Gaussian Mixture models* or *k-means* clustering is used to separate out the neuronal cells in multi-neuron interaction interpretation before applying single neuron tracing techniques.

Adaptation of our proposed automatic neuronal morphometry analysis framework to such high content, high resolution data can capture the key information for intertwined neural networks. This would require proposal of effective energy functions and marked objects to combine the color, structure and gradient information for neurite detection in presence of undesired channel cross-talk and insufficient resolution. Moreover, it is challenging to deal with shape variability presented by soma and neurites as encountered in whole neuron scenarios. One limitation of our algorithm is its poor results on densely branching regions, a general problem when using highly blurred images where processes that are very close or seem to touch each other. The combination of genetic labeling with super-resolution imaging technology has proven to produce image data with better reliability for accurate quantification of neuronal arbors position, even in densely labeled data [94, 62, 75].

6.2.3 Massively parallelized processing for high-throughput analysis

For large scale, high through-put analysis of neuronal morphology it is inevitable to have optimally parallelized implementation of our proposed automated reconstruction algorithm. The most attractive feature of our proposed MPP model is its inherent, multi-level parallelization scope and thus, its ability to scale. MCMC simulations are notorious for their slow convergence. Various studies have focused on exploiting its "embarrassingly" parallel property to speed up computation. Our current implementation uses a multiple birth and death dynamics that speeds up convergence. Further it reduces computational load by avoiding RJMCMC type perturbation moves on the objects. Our MATLAB implementation runs on a stand-alone desktop. However, the practicality of such algorithm in high throughput microscopy applications demands parallelized implementation. In [10, 121], are two examples of MPP family of algorithms whose massively parallel processing have enabled significant reductions in runtime, from few hours to few seconds.

There has been considerable efforts to speed up MCMC algorithms by both implementation tricks and statistical techniques. Beyond guarantee of convergence, the efficiency of these algorithms needs to be considered. A low acceptance ratio for transition between states leads to a slower convergence speed and wasteful CPU computation time. To fully exploit the advantage of marked point processes on image processing tasks, further work on optimization techniques is necessary. On the other hand, in [22], are presented implementation techniques of MCMC algorithms to optimally take advantage of multi-core and

multi-processor architectures in reducing the runtime of MCMC applications. Our profiling of the execution showed that the maximum computation time is

Function	% of total execution time
Birth	85%
Eigen Analysis	76%
Death	7%

Table 6.1: Table shows time spent in each section of MPP algorithm.

incurred in the calculation of the data energy term 6.1. It indicates that the maximum time is spent in Eigen analysis and computation of data energy response. Our data energy response is independent of other objects influence and hence can be easily computed in parallel, perhaps using Eigen analysis in GPUs to speed up the process. The second order terms where neighboring objects influence each others' overall energy places constraints on the parallel simulation of spatial processes. Problem arises when computation on one spatial position of data is dependent on concurrent computation in another position. For example, if objects were killed in parallel, we have to synchronize the order of killing objects so as not to penalize an object for an overlapping neighbor that has already been killed. This dependency requires segregating zones of influence in the data volume, a task handled through a chessboard scheme of non-interacting block level parallelization in [120]. Such constraints makes parallel computation of stochastic lattice models a non trivial task. In [64], the author demonstrates how each processor performs computations on a single sub-lattice and maintains communication between processes responsible for adjacent sub-lattices in an efficient way without creating long stalls in computation. Hence, we propose

that 2 potential avenues to investigate for high-throughput analysis of neuronal morphology analysis -

1. GPU processing of neuriteness measure to speed up the data energy response computation.

2. Optimal parallelization of MPP framework for taking advantage of multi-core systems and inherent parallelism of Markov Chains.

Bibliography

[1] The allen brain atlas project. `http://www.brain-map.org/`.

[2] The blue brain project. `http://bluebrain.epfl.ch/`.

[3] Eyewire: A game to map the brain. `http://blog.eyewire.org/about/`.

[4] K. Al-Kofahi, A. Can, S. Lasek, D. Szarowski, N. Dowell-Mesfin, W. Shain, J. Turner, and B. Roysam. Median-based robust algorithms for tracing neurons from noisy confocal microscope images. *IEEE Transactions on Information Technology in Biomedicine*, 7(4):302–317, 2003.

[5] K. Al-Kofahi, S. Lasek, D. Szarowski, C. Pace, G. Nagy, J. Turner, and B. Roysam. Rapid automated three-dimensional tracing of neurons from confocal image stacks. *IEEE Transactions on Information Technology in Biomedicine*, 6(2):171–187, 2002.

[6] O. Al-Kofahi, A. Can, S. Lasek, D. Szarowski, J. Turner, and B. Roysam. Algorithms for accurate 3d registration of neuronal images acquired by confocal scanning laser microscopy. *Journal of Microscopy*, 211(1):8–18, 2003.

[7] Y. Al-Kofahi, N. Dowell-Mesfin, C. Pace, W. Shain, J. Turner, and B. Roysam. Improved detection of branching points in algorithms for automated neuron tracing from 3d confocal images. *Cytometry Part A*, 73(1):36–43, 2008.

[8] G. Ascoli, J. Krichmar, S. Nasuto, and S. Senft. Generation, description and storage of dendritic morphology data. *Philosophical Transactions of the Royal Society of London. Series B: Biological Sciences*, 356(1412):1131–1145, 2001.

[9] G. A. Ascoli. Neuroinformatics grand challenges. *Neuroinformatics*, 6(1):1–3, 2008.

[10] C. Avenel, P. Fortin, and D. Béréziat. Parallel birth and death process for cell nuclei extraction in histopathology images. *Proceedings of International Conference on Parallel Processing, (ICPP)*, pages 429–438, October 2013.

[11] S. R. Aylward and E. Bullitt. Initialization, noise, singularities and scale in height ridge traversal for tubular object centerline extraction. *IEEE Transactions on Medical Imaging*, 21(2):61–75, 2002.

[12] A. Baddeley and M. Van Lieshout. Stochastic geometry models in high-level vision. *Journal of Applied Statistics*, 20(5-6):231–256, 1993.

[13] E. Bas and D. Erdogmus. Principal curves as skeletons of tubular objects - locally characterizing the structures of axons. *Neuroinformatics*, 9(2-3):181–191, 2011.

[14] S. Basu, A. Aksel, B. Condron, and S. T. Acton. Tree2tree: neuron segmentation for generation of neuronal morphology. In *Proceedings of IEEE International Symposium on Biomedical Imaging,(ISBI)*, pages 548–551, 2010.

[15] S. Basu, B. Condron, and S. T. Acton. Path2path: Hierarchical path-based analysis for neuron matching. In *Proceedings of IEEE International Symposium on Biomedical Imaging, (ISBI)*, pages 996–999, 2011.

[16] S. Basu, B. Condron, A. Aksel, and S. T. Acton. Segmentation and tracing of single neurons from 3d confocal microscope images. *IEEE J. Biomedical and Health Informatics*, 17(2):319–335, 2013.

[17] S. Basu, M. S. Kulikova, E. Zhizhina, W. T. Ooi, and D. Racoceanu. A stochastic model for automatic extraction of 3d neuronal morphology. *Proceedings of International Conference on Medical Image Computing and Computer Assisted Intervention (1), (MICCAI)*, pages 396–403, 2013.

[18] S. Basu, W. T. Ooi, and D. Racoceanu. Improved marked point process priors for single neurite tracing. *Proceedings of International Workshop on Pattern Recognition in Neuroimaging, (PRNI)*, pages 1–4, 2014.

[19] S. Basu and D. Racoceanu. Reconstructing neuronal morphology from microscopy stacks using fast marching. *Proceedings of IEEE International Conference on Image Processing, (ICIP)*, pages 3597 – 3601, October 2014.

[20] S. Ben Hadj, F. Chatelain, X. Descombes, and J. Zerubia. Parameter estimation for a marked point process within a framework of multidimensional shape extraction from remote sensing images. *Proceedings of ISPRS Technical Commission III Symposium on Photogrammetry Computer Vision and Image Analysis, (PCV)*, page 1, Sept. 2010.

[21] K. Brown, G. Barrionuevo, A. Canty, V. De Paola, J. Hirsch, G. Jefferis, J. Lu, M. Snippe, I. Sugihara, and G. Ascoli. The diadem data sets: Representative light microscopy images of neuronal morphology to advance automation of digital reconstructions. *Neuroinformatics*, pages 1–15, 2011.

[22] J. M. R. Byrd, S. A. Jarvis, and A. H. Bhalerao. On the parallelisation of mcmc-based image processing. *Workshop Proceedings of IEEE International Symposium on Parallel and Distributed Processing, (IPDPS)*, pages 1–8, 2010.

[23] P. Cariou, X. Descombes, and E. Zhizhina. A point process for fully automatic road network detection in satellite and aerial images. *Problems of Information Transmission*, 10(3):247–256, 2010.

[24] F. Chatelain, X. Descombes, and J. Zerubia. Parameter estimation for marked point processes. application to object extraction from remote sensing images. *Proceedings of International Conference on Energy Minimization Methods in Computer Vision and Pattern Recognition, (EMMCVPR)*, pages 221–234, 2009.

[25] F. Chatelain, S. Lambert-Lacroix, and J.-Y. Tourneret. Pairwise likelihood estimation for multivariate mixed poisson models generated by gamma intensities. *Statistics and Computing*, 19(3):283–301, 2009.

[26] A. Choromanska, S.-F. Chang, and R. Yuste. Automatic reconstruction of neural morphologies with multi-scale tracking. *Frontiers in Neural Circuits*, 6:25, 2012.

[27] P. Chothani, V. Mehta, and A. Stepanyants. Automated tracing of neurites from light microscopy stacks of images. *Neuroinformatics*, 9(2-3):263–278, 2011.

[28] L. D. Cohen and R. Kimmel. Fast marching the global minimum of active contours. *Proceedings of IEEE International Conference on Image Processing (1),(ICIP)*, pages 473–476, 1996.

[29] W. Czarnecki. Multilayer neural networks with receptive fields as a model for the neuron reconstruction problem. *Proceedings of International Conference on Artificial Intelligence and Soft Computing (2), (ICAISC)*, pages 242–250, 2012.

[30] D. J. Daley and D. Vere-Jones. *An introduction to the theory of point processes*, volume 2. 1988.

[31] E. O. Denloye-Ito and S. T. Acton. Phase congruency eigendecomposition for multi-scale neuronal enhancement. *Proceedings of Asilomar Conference on Signals, Systems and Computers*, pages 638–642, 2012.

[32] X. Descombes, R. Minlos, and E. Zhizhina. Object extraction using a stochastic birth-and-death dynamics in continuum. *Journal of Mathematical Imaging and Vision*, 33(3):347–359, 2009.

[33] X. Descombes, M. van Lieshout, R. Stoica, and J. Zerubia. Parameter estimation by a markov chain monte carlo technique for the candy model. *Proceedings of IEEE Workshop on Statistical Signal Processing, Singapour*, 2001.

[34] D. E. Donohue and G. A. Ascoli. Automated reconstruction of neuronal morphology: An overview. *Brain Research Reviews*, 67:94 – 102, 2011.

[35] J. Evers, S. Schmitt, M. Sibila, and C. Duch. Progress in functional neuroanatomy: precise automatic geometric reconstruction of neuronal morphology from confocal image stacks. *Journal of Neurophysiology*, 93(4):2331–2342, 2005.

[36] A. F. Frangi, W. J. Niessen, K. L. Vincken, and M. A. Viergever. Muliscale vessel enhancement filtering. *Proceedings of International Conference on Medical Image Computing and Computer Assisted Intervention (1), (MICCAI)*, pages 130–137, 1998.

[37] R. Gala, J. Chapeton, J. Jitesh, C. Bhavsar, and A. Stepanyants. Active learning of neuron morphology for accurate automated tracing of neurites. *Frontiers in Neuroanatomy*, 8, 2014.

[38] A. Gamal Eldin, X. Descombes, and J. Zerubia. Multiple birth and cut algorithm for point process optimization. *Proceedings of Signal-Image Technology and Internet-Based Systems, (SITIS)*, Dec. 2010.

[39] A. Gamal-Eldin, X. Descombes, and J. Zerubia. A novel algorithm for occlusions and perspective effects using a 3d object process. *Proceedings of IEEE International Conference on Acoustics, Speech, and Signal Processing, (ICASSP)*, pages 1569–1572, 2011.

[40] W. Ge and R. T. Collins. Marked point processes for crowd counting. *Proceedings of IEEE Conference on Computer Vision and Pattern Recognition, (CVPR)*, pages 2913–2920, 2009.

[41] T. A. Gillette, K. M. Brown, and G. A. Ascoli. The diadem metric: Comparing multiple reconstructions of the same neuron. *Neuroinformatics*, 9(2-3):233–245, 2011.

[42] T. A. Gillette, K. M. Brown, K. Svoboda, Y. Liu, and G. A. Ascoli. Diademchallenge.org: A compendium of resources fostering the continuous development of automated neuronal reconstruction. *Neuroinformatics*, 9(2-3):303–304, 2011.

[43] T. A. Gillette and J. J. Grefenstette. On comparing neuronal morphologies with the constrained tree-edit-distance. *Neuroinformatics*, 7(3):191–194, 2009.

[44] G. González, F. Fleuret, and P. Fua. Learning rotational features for filament detection. *Proceedings of IEEE Conference on Computer Vision and Pattern Recognition, (CVPR)*, pages 1582–1589, 2009.

[45] M. Halavi, K. A. Hamilton, R. Parekh, and G. A. Ascoli. Digital reconstructions of neuronal morphology: three decades of research trends. *Frontiers in neuroscience*, 6, 2012.

[46] B. He, T. Coleman, G. M. Genin, G. Glover, X. Hu, N. Johnson, T. Liu, S. Makeig, P. Sajda, and K. Ye. Grand challenges in mapping the human brain: Nsf workshop report. *IEEE transactions on biomedical engineering*, 60(11):2983–2992, 2013.

[47] H. Y. He and H. T. Cline. Diadem x: Automated 4 dimensional analysis of morphological data. *Neuroinformatics*, 9(2-3):107–112, 2011.

[48] W. He, T. Hamilton, A. Cohen, T. Holmes, C. Pace, D. Szarowski, J. Turner, B. Roysam, et al. Automated three-dimensional tracing of neurons in confocal and brightfield images. *Microscopy and Microanalysis*, 9(4):296–310, 2003.

[49] M. Helmstaedter, K. Briggman, and W. Denk. 3d structural imaging of the brain with photons and electrons. *Current Opinion in Neurobiology*, 18(6):633–641, 2008.

[50] H. Heumann and G. Wittum. The tree-edit-distance: a measure for quantifying neuronal morphology. *Neuroinformatics*, 7:191–194, 2009.

[51] H. Irshad, A. Gouaillard, L. Roux, and D. Racoceanu. Spectral band selection for mitosis detection in histopathology. *Proceedings of IEEE International Symposium on Biomedical Imaging (ISBI)*, pages 1279–1282, 2014.

[52] H. Irshad, A. Veillard, L. Roux, and D. Racoceanu. Methods for nuclei detection, segmentation and classification in digital histopathology: A review - current status and future potential. *IEEE Reviews in Biomedical Engineering*, 7:97–114, April 2014.

[53] C. Kirbas and F. Quek. A review of vessel extraction techniques and algorithms. *ACM Computing Surveys*, 36(2):81–121, June 2004.

[54] V. Kolmogorov and R. Zabih. What energy functions can be minimized via graph cuts. *IEEE Transactions on Pattern Analysis and Machine Intelligence*, 26:65–81, 2004.

[55] I. Konstantinidis, A. Santamaría-Pang, and I. Kakadiaris. Frames-based denoising in 3d confocal microscopy imaging. *Proceedings of IEEE International Conference of the Engineering in Medicine and Biology Society, (EMBS)*, pages 290–293, 2005.

[56] K. Krissian, G. Malandain, N. Ayache, R. Vaillant, and Y. Trousset. Model-based multiscale detection of 3d vessels. *Proceedings of IEEE Conference on Computer Vision and Pattern Recognition, (CVPR)*, pages 722–727, 1998.

[57] J. Kruskal. On the shortest spanning subtree of a graph and the traveling salesman problem. *Proceedings of the American Mathematical Society*, pages 48–50, 1956.

[58] M. Kulikova, I. Jermyn, X. Descombes, E. Zhizhina, and J. Zerubia. A marked point process model including strong prior shape information applied to multiple object extraction from images. *International Journal of Computer Vision and Image Processing, (IJCVIP)*, 1(2):1–12, 2011.

[59] C. Lacoste, X. Descombes, and J. Zerubia. Point processes for unsupervised line network extraction in remote sensing. *IEEE Transactions on Pattern Analysis and Machine Intelligence*, 27(10):1568–1579, 2005.

[60] C. Lacoste, X. Descombes, and J. Zerubia. Unsupervised line network extraction in remote sensing using a polyline process. *Pattern Recognition*, 43(4):1631–1641, 2010.

[61] C. Lacoste, G. Finet, and I. E. Magnin. Coronary tree extraction from x-ray angiograms using marked point processes. *Proceedings of IEEE International Symposium on Biomedical Imaging, (ISBI)*, pages 157–160, 2006.

[62] M. Lakadamyali, H. Babcock, M. Bates, X. Zhuang, and J. Lichtman. 3d multicolor super-resolution imaging offers improved accuracy in neuron tracing. *PloS ONE*, 7(1):e30826, 2012.

[63] M. W. Law, K. Tay, A. Leung, G. J. Garvin, and S. Li. Dilated divergence based scale-space representation for curve analysis. pages 557–571, 2012.

[64] J. Lee, R. Kulperger, and H. Yu. Parallel computation of stochastic lattice models. *Thesis*, 2011.

[65] P.-C. Lee, Y.-T. Ching, H. M. Chang, and A.-S. Chiang. A semi-automatic method for neuron centerline extraction in confocal microscopic image stack. *Proceedings of IEEE International Symposium on Biomedical Imaging, (ISBI)*, pages 959–962, 2008.

[66] P.-C. Lee, C.-C. Chuang, A.-S. Chiang, and Y.-T. Ching. High-throughput computer method for 3d neuronal structure reconstruction from the image stack of

the *drosophila* brain and its applications. *PLoS Computational Biology*, 8(9), 2012.

[67] J. W. Lichtman, J. Livet, and J. R. Sanes. A technicolour approach to the connectome. *Nature Reviews Neuroscience*, 9(6):417–422, 2008.

[68] M. Liu, H. Peng, A. K. R. Chowdhury, and E. W. Myers. 3d neuron tip detection in volumetric microscopy images. *Proceedings of IEEE International Conference on Bioinformatics and Biomedicine, (BIBM)*, pages 366–371, 2011.

[69] Y. Liu. The diadem and beyond. *Neuroinformatics*, 9(2-3):99–102, 2011.

[70] N. Loménie and D. Racoceanu. Point set morphological filtering and semantic spatial configuration modeling: Application to microscopic image and biostructure analysis. *Pattern Recognition*, 45(8):2894–2911, 2012.

[71] M. H. Longair, D. A. Baker, and J. D. Armstrong. Simple neurite tracer: open source software for reconstruction, visualization and analysis of neuronal processes. *Bioinformatics*, 27(17):2453–2454, 2011.

[72] J. Lu, J. C. Fiala, and J. W. Lichtman. Semi-automated reconstruction of neural processes from large numbers of fluorescence images. *PLoS ONE*, 4(5):e5655, 05 2009.

[73] J. Lu, J. C. Tapia, O. L. White, and J. W. Lichtman. The interscutularis muscle connectome. *PLoS Biology*, 7(2):e1000032, 2009.

[74] J. Macke, N. Maack, R. Gupta, W. Denk, B. Schölkopf, and A. Borst. Contour-propagation algorithms for semi-automated reconstruction of neural processes. *Journal of Neuroscience Methods*, 167(2):349–357, 2008.

[75] M. Maglione and S. J. Sigrist. Seeing the forest tree by tree: super-resolution light microscopy meets the neurosciences. *Nature Neuroscience*, 16(7):790–797, 2013.

[76] R. Malladi and J. A. Sethian. Level set and fast marching methods in image processing and computer vision. *Proceedings of IEEE International Conference on Image Processing (1),(ICIP)*, pages 489–492, 1996.

[77] D. Mayerich, C. Björnsson, J. Taylor, and B. Roysam. Metrics for comparing explicit representations of interconnected biological networks. *Proceedings of Symposium on Biological Data Visualization, (BioVis)*, pages 79–86, 2011.

[78] D. Mayerich, C. Bjornsson, J. Taylor, and B. Roysam. Netmets: software for quantifying and visualizing errors in biological network segmentation. *BMC Bioinformatics*, 13(Suppl 8):S7, 2012.

[79] E. Meijering. Neuron tracing in perspective. *Cytometry Part A*, 77(7):693–704, 2010.

[80] E. Meijering, M. Jacob, J. C. F. Sarria, P. Steiner, H. Hirling, and M. Unser. Design and validation of a tool for neurite tracing and analysis in fluorescence microscopy images. *Cytometry Part A,*, 58(2):167–176, 2004.

[81] A. Mottini, X. Descombes, and F. Besse. Axon extraction from fluorescent confocal microscopy images. *Proceedings of IEEE International Symposium on Biomedical Imaging, (ISBI)*, pages 764–767, 2012.

[82] A. Mottini, X. Descombes, and F. Besse. Axonal tree classification using an elastic shape analysis based distance. *Proceedings of IEEE International Symposium on Biomedical Imaging (ISBI)*, pages 850–853, 2014.

[83] A. Mukherjee and A. Stepanyants. Automated reconstruction of neural trees using front re-initialization. In *Proceedings of SPIE Medical Imaging*, pages 83141I–83141I. International Society for Optics and Photonics, 2012.

[84] S. Mukherjee and S. T. Acton. Vector field convolution medialness applied to neuron tracing. *Proceedings of IEEE International Conference on Image Processing, (ICIP)*, pages 665–669, 2013.

[85] S. Mukherjee, S. Basu, B. Condron, and S. T. Acton. A geometric-statistical approach toward neuron matching. *Proceedings of IEEE International Symposium on Biomedical Imaging, (ISBI)*, pages 772–775, 2012.

[86] S. Mukherjee, S. Basu, B. Condron, and S. T. Acton. Tree2tree2: Neuron tracing in 3d. In *Proceedings of IEEE International Symposium on Biomedical Imaging, (ISBI)*, pages 448–451, 2013.

[87] S. Mukherjee, B. Condron, and S. T. Acton. Chasing the neurome: Segmentation and comparison of neurons. *Proceedings of Signal Processing Conference, (EUSIPCO)*, pages 1–4, 2013.

[88] S. Mukherjee, B. Condron, and S. T. Acton. Neuron segmentation with level sets. In *Proceedings of Asilomar Conference on Signals, Systems and Computers*, pages 1078–1082. IEEE, 2013.

[89] D. R. Myatt, T. Hadlington, G. A. Ascoli, and S. J. Nasuto. Neuromantic–from semi-manual to semi-automatic reconstruction of neuron morphology. *Frontiers in Neuroinformatics*, 6, 2012.

[90] A. Narayanaswamy, S. Dwarakapuram, C. Bjornsson, B. Cutler, W. Shain, and B. Roysam. Robust adaptive 3-d segmentation of vessel laminae from fluores-

cence confocal microscope images & parallel gpu implementation. *Microscopy and Microanalysis*, 14(S2):726–727, 2008.

[91] A. Narayanaswamy, Y. Wang, and B. Roysam. 3-d image pre-processing algorithms for improved automated tracing of neuronal arbors. *Neuroinformatics*, 9(2-3):219–231, 2011.

[92] M. Narro, F. Yang, R. Kraft, C. Wenk, A. Efrat, and L. Restifo. Neuronmetrics: software for semi-automated processing of cultured neuron images. *Brain Research*, 1138:57–75, 2007.

[93] M. Oberlaender, R. Bruno, B. Sakmann, and P. Broser. Transmitted light brightfield mosaic microscopy for three-dimensional tracing of single neuron morphology. *Journal of Biomedical Optics*, 12:064029, 2007.

[94] Y. A. Pan, J. Livet, J. R. Sanes, J. W. Lichtman, and A. F. Schier. Multicolor brainbow imaging in zebrafish. *Cold Spring Harbor Protocols*, 2011:pdb–prot5546, 2011.

[95] H. Peng. Bioimage informatics: a new area of engineering biology. *Bioinformatics*, 24(17):1827–1836, 2008.

[96] H. Peng, F. Long, and G. Myers. Automatic 3d neuron tracing using all-path pruning. *Bioinformatics [ISMB/ECCB]*, 27(13):239–247, 2011.

[97] H. Peng, Z. Ruan, D. Atasoy, and S. Sternson. Automatic reconstruction of 3d neuron structures using a graph-augmented deformable model. *Bioinformatics*, 26(12):i38–i46, 2010.

[98] T. Pock, C. Janko, R. Beichel, and H. Bischof. Multiscale medialness for robust segmentation of 3d tubular structures. *Proceedings of the Computer Vision Winter Workshop*, pages 93–102, 2005.

[99] M. Pool, J. Thiemann, A. Bar-Or, and A. E. Fournier. Neuritetracer: a novel imagej plugin for automated quantification of neurite outgrowth. *Journal of Neuroscience Methods*, 168(1):134–139, Feb. 2008.

[100] R. Rigamonti and V. Lepetit. Accurate and efficient linear structure segmentation by leveraging ad hoc features with learned filters. *Proceedings of International Conference on Medical Image Computing and Computer Assisted Intervention (1), (MICCAI)*, pages 189–197, 2012.

[101] A. Rodriguez, D. Ehlenberger, D. Dickstein, P. Hof, and S. Wearne. Automated three-dimensional detection and shape classification of dendritic spines from fluorescence microscopy images. *PLoS ONE*, 3(4):e1997, 2008.

[102] L. Roux, D. Racoceanu, N. Loménie, M. Kulikova, H. Irshad, J. Klossa, F. Capron, C. Genestie, G. Le Naour, and M. N. Gurcan. Mitosis detection in breast cancer histological images an icpr 2012 contest. *Journal of Pathology Informatics*, 4, 2013.

[103] N. A. Sarder P. Deconvolution methods for 3-d flourescense microscopy images. *IEEE Signal Processsing Magazine*, 23:32–45, 2006.

[104] R. Sarkar, S. Mukherjee, and S. T. Acton. Shape descriptors based on compressed sensing with application to neuron matching. *Proceedings of Asilomar Conference on Signals, Systems and Computers*, pages 970–974, 2013.

[105] J. Schindelin, I. Arganda-Carreras, E. Frise, V. Kaynig, M. Longair, T. Pietzsch, S. Preibisch, C. Rueden, S. Saalfeld, B. Schmid, et al. Fiji: an open-source platform for biological-image analysis. *Nature Methods*, 9(7):676–682, 2012.

[106] S. Schmitt, J. Evers, C. Duch, M. Scholz, and K. Obermayer. New methods for the computer-assisted 3-d reconstruction of neurons from confocal image stacks. *NeuroImage*, 23(4):1283–1298, 2004.

[107] S. L. Senft. A brief history of neuronal reconstruction. *Neuroinformatics*, 9(2):119–128, 2011.

[108] A. Sironi, V. Lepetit, and P. Fua. Multiscale centerline detection by learning a scale-space distance transform. In *Computer Vision and Pattern Recognition (CVPR), Proceedings of IEEE Conference on*, pages 2697–2704. IEEE, 2014.

[109] R. Srinivasan, X. Zhou, E. Miller, J. Lu, J. Litchman, and S. Wong. Automated axon tracking of 3d confocal laser scanning microscopy images using guided probabilistic region merging. *Neuroinformatics*, 5(3):189–203, 2007.

[110] U. Sümbül, A. Zlateski, A. Vishwanathan, R. H. Masland, and S. Seung. Automated computation of arbor densities: a step toward identifying neuronal cell types. *Frontiers in Neuroanatomy*, 8:139, 2014.

[111] K. Sun, N. Sang, and T. Zhang. Marked point process for vascular tree extraction on angiogram. *Proceedings of International Conference on Energy Minimization Methods in Computer Vision and Pattern Recognition, (EMMCVPR)*, pages 467–478, 2007.

[112] K. Svoboda. The past, present, and future of single neuron reconstruction. *Neuroinformatics*, 9(2-3):97–98, 2011.

[113] G. Tsechpenakis, P. Mukherjee, M. D. Kim, and A. Chiba. Three-dimensional motor neuron morphology estimation in the drosophila ventral nerve cord. *IEEE Transactions on Biomedical Engineering*, 59(5):1253–1263, 2012.

[114] E. Türetken, C. Blum, G. González, and P. Fua. Reconstructing geometrically consistent tree structures from noisy images. *Proceedings of International Conference on Medical Image Computing and Computer Assisted Intervention (1), (MICCAI)*, pages 291–299, 2010.

[115] E. Türetken, G. González, C. Blum, and P. Fua. Automated reconstruction of dendritic and axonal trees by global pptimization with geometric priors. *Neuroinformatics*, 9(2-3):279–302, 2011.

[116] P. Vallotton, R. Lagerstrom, C. Sun, M. Buckley, D. Wang, M. De Silva, S. Tan, and J. Gunnersen. Automated analysis of neurite branching in cultured cortical neurons using hca-vision. *Cytometry Part A*, 71(10):889–895, 2007.

[117] M. Van Lieshout. *Markov point processes and their applications*. Imperial College Press, 2000.

[118] A. Vasilevskiy and K. Siddiqi. Flux maximizing geometric flows. *IEEE Transactions on Pattern Analysis and Machine Intelligence*, 24(12):1565–1578, 2002.

[119] Z. Vasilkoski and A. Stepanyants. Detection of the optimal neuron traces in confocal microscopy images. *Journal of Neuroscience Methods*, 178(1):197–204, 2009.

[120] Y. Verdié and F. Lafarge. Efficient monte carlo sampler for detecting parametric objects in large scenes. *Proceedings of European Conference on Computer Vision (3), (ECCV)*, pages 539–552, 2012.

[121] Y. Verdie and F. Lafarge. Detecting parametric objects in large scenes by monte carlo sampling. *International Journal of Computer Vision*, 106(1):57–75, 2014.

[122] Y. Wang, A. Narayanaswamy, C.-L. Tsai, and B. Roysam. A broadly applicable 3-d neuron tracing method based on open-curve snake. *Neuroinformatics*, 9(2-3):193–217, 2011.

[123] S. Wearne, A. Rodriguez, D. Ehlenberger, A. Rocher, S. Henderson, and P. Hof. New techniques for imaging, digitization and analysis of three-dimensional neural morphology on multiple scales. *Neuroscience*, 136(3):661–680, 2005.

[124] C. Weaver, P. Hof, S. Wearne, and W. Lindquist. Automated algorithms for multiscale morphometry of neuronal dendrites. *Neural Computation*, 16(7):1353–1383, 2004.

[125] J. G. White, E. Southgate, J. N. Thomson, and S. Brenner. The structure of the nervous system of the nematode caenorhabditis elegans. *Philosophical Transactions of the Royal Society of London. Series B, Biological Sciences*, 314(1165):1–340, 1986.

[126] M. H. F. Wilkinson and M. A. Westenberg. Shape preserving filament enhancement filtering. *Proceedings of International Conference on Medical Image Computing and Computer Assisted Intervention, (MICCAI)*, pages 770–777, 2001.

[127] H. Xiao and H. Peng. App2: automatic tracing of 3d neuron morphology based on hierarchical pruning of a gray-weighted image distance-tree. *Bioinformatics*, 29(11):1448–1454, 2013.

[128] H. Xiao and H. Peng. App2: automatic tracing of 3d neuron morphology based on hierarchical pruning of a gray-weighted image distance-tree. *Bioinformatics*, 29(11):1448–1454, 2013.

[129] G. Xiong, X. Zhou, A. Degterev, L. Ji, and S. Wong. Automated neurite labeling and analysis in fluorescence microscopy images. *Cytometry Part A*, 69(6):494–505, 2006.

[130] C. Xu and J. L. Prince. Snakes, shapes, and gradient vector flow. *IEEE Transactions on Image Processing*, 7(3):359–369, 1998.

[131] J. Yang, P. T. Gonzalez-Bellido, and H. Peng. A distance-field based automatic neuron tracing method. *BMC Bioinformatics*, 14:93, 2013.

[132] W. Yu, H. K. Lee, S. Hariharan, W. Bu, and S. Ahmed. Level set segmentation of cellular images based on topological dependence. *Proceedings of Advances in Visual Computing*, pages 540–551, 2008.

[133] W. Yu, H. K. Lee, S. Hariharan, W. Bu, and S. Ahmed. Evolving generalized voronoi diagrams for accurate cellular image segmentation. *Cytometry Part A*, 77(4):379–386, 2010.

[134] Y. Zhang, X. Zhou, A. Degterev, M. Lipinski, D. Adjeroh, J. Yuan, and S. Wong. Automated neurite extraction using dynamic programming for high-throughput screening of neuron-based assays. *NeuroImage*, 35(4):1502–1515, 2007.

[135] T. Zhao and S. M. Plaza. Automatic neuron type identification by neurite localization in the drosophila medulla. *arXiv preprint*, 2014.

[136] T. Zhao, J. Xie, F. Amat, N. Clack, P. Ahammad, H. Peng, F. Long, and E. Myers. Automated reconstruction of neuronal morphology based on local geometrical and global structural models. *Neuroinformatics*, 9(2-3):247–261, 2011.